Habilitation thesis

submitted to the

Eötvös Loránd University
Faculty of Science
Institute of Physics

by

Dr. Péter Dusán Ispánovity
Eötvös Loránd University
Faculty of Science
Department of Materials Physics

Budapest, September 2021

Nomenclature

Notations

G	Elastic constant: $\mu/[2\pi(1-\nu)]$
L	System size
M	Dislocation mobility
N	Total number of dislocations in 2D DDD simulations
P	Plastic potential
v^{d}	Drift velocity
v^{m}	Mean velocity
ρ	Total (or statistically stored) dislocation density
κ	Geometrically necessary dislocation density
α_{ij}	Components of the Nye dislocation density tensor
σ	Stress
ε	Strain
$\varepsilon_{\mathrm{pl}}$	Plastic strain
τ	Shear stress
τ_{ind}	Shear stress of an individual straight edge dislocation
τ_{ext}	Externally applied shear stress
τ^{mf}	Mean field stress
τ^{b}	Back-stress
τ^{d}	Diffusion stress
τ^{y}	Yield stress
γ	Shear strain
μ	Shear modulus
ν	Poisson number

Abbreviations

2D	Two-dimensional
3D	Three-dimensional
AE	Acoustic emission
CA	Cellular automaton

CDD	Continuum dislocation dynamics
CTD	Continuous time dynamics
DDD	Discrete dislocation dynamics
EBSD	Electron backscatter diffraction
ED	Extremal dynamics
FCC	Face-centered-cubic
FEM	Finite element method
FIB	Focused ion beam
GND	Geometrically necessary dislocation
HR-EBSD	High-resolution electron backscatter diffraction
IPF	Inverse pole figure
MFD	mean-field depinning
ML	Machine learning
PBC	Periodic boundary condition
PLC	Portevin–Le Chatelier
RD	Random dynamics
SCPM	Stochastic continuum plasticity model
SEM	Scanning electron microscope
SSD	Statistically stored dislocation
STEM	Scanning transmission electron microscopy
XRD	x-ray diffraction

Contents

1 Curriculum Vitæ

Personal details

NAME	Péter Dusán Ispánovity
DATE AND PLACE OF BIRTH	24 October 1980, Budapest
ADDRESS	Eötvös Loránd University, Department of Materials Physics, H-1117 Budapest, Pázmány Péter sétány 1/a, Hungary
PHONE	+36 1 3722812
EMAIL	ispanovity.peter@ttk.elte.hu
WEB	ispanovity.web.elte.hu

Employment

JUL. 2011 – PRESENT	ASSISTANT PROFESSOR, Eötvös Loránd University, Budapest, Hungary
AUG. 2009 – JUL. 2011	POSTDOCTORAL FELLOW Paul Scherrer Institut, Villigen, Switzerland
MAR. 2008 – JUN. 2009	TEACHING ASSISTANT Eötvös Loránd University, Budapest, Hungary

Education

SEP. 2005 – AUG. 2009	PHD IN PHYSICS (MATERIALS SCIENCE PROGRAMME) Eötvös Loránd University, Budapest, Hungary Supervisor: Prof. István Groma Grade of Diploma: *summa cum laude*

Sep. 2001 – Jan. 2009	MSc in Computer Science Eötvös Loránd University, Budapest, Hungary Supervisor: Prof. Gisbert Stoyan Grade of Diploma: *with distinction*
Sep. 2001 – Jan. 2009	MSc in Physics Eötvös Loránd University, Budapest, Hungary Supervisor: Prof. István Groma Grade of Diploma: *with distinction*

Projects lead as a principal investigator

2021 – 2025	Experimental and theoretical investigation of micron-scale stochastic deformation phenomena; NKFIH-FK-138975 OTKA young researchers' excellence programme (FK_21)
2017 – 2019	Theoretical and experimental investigations of dislocation avalanches; NKFIH-KH-125380 Funding for research groups with internationally outstanding high impact results (KH_18)
2012 – 2016	Stochastic and statistical properties of dislocation plasticty; CIG-321842 (StochPlast) EU FP7 Marie Curie Career Integration Grant (CIG)
2012 – 2016	Stochastic properties of micron-scale plasticity; OTKA-PD-105256 Postdoctoral excellence programme

Awards and fellowships

2015 – 2019	János Bolyai Postdoctoral Fellowship
2018 – 2019	Bolyai+ Fellowship of the New National Excellence Programme

2017 – 2018	Fellowship of the New National Excellence Programme
2016	Excellent Lecturer of the Faculty, Eötvös Loránd University, Faculty of Science
2016	Excellence Award of the Rector, Eötvös Loránd University

Invited talks at international conferences

Jan. 2011	Slow relaxation processes and scaling in dislocation systems International Workshop on Fluctuations in Materials Science, Courmayeur, Italy
Aug. 2012	Statistical properties of plasticity: from 2D models to micropillars Dislocations 2012 – 4th international conference on fundamental properties of dislocations, Budapest, Hungary
Aug. 2012	Statistical properties of plasticity: from 2D models to micropillars MMM 2012 - 6th International Conference on Multiscale Materials Modeling, Singapore
Jan. 2014	Statistical properties of strain bursts in plastic deformation International Workshop on Avalanches and Intermittency in out-of-equilibrium systems, Courmayeur, Italy
Feb. 2014	Scale-free dynamics during plastic deformation The Schöntal Symposium: Dislocation-based Plasticity, Schöntal, Germany
Sep. 2014	Scale-free dynamics in dislocation systems International Conference on Smart Functional Materials for Shaping our Future, Debrecen, Hungary

Oct. 2015	Effects of Elastic Anharmonicity and Dislocation Climb on Patterning SIPS 2015 - Sustainable Industrial Processing Summit & Exhibition, Antalya, Turkey
Apr. 2018	Multiscale modelling of dislocation patterning MRS Spring Meeting, Phoenix AZ, USA
Apr. 2018	Extended criticality and anomalous system size scaling in crystal plasticity Nordita workshop on Crackling Noise in Materials, Stockholm, Sweden
Oct. 2018	Effect of solute atoms on the on the critical behaviour of discrete dislocations MMM 2018 – 9th International Conference on Multiscale Materials Modeling, Osaka, Japan
Feb. 2019	Acoustic emission of crystalline micropillars Workshop on Avalanche Dynamics and Precursors of Catastrophic Events, Les Houches, France
May 2019	Numerical and experimental investigations of dislocation avalanches Seminar talk at the Department of Applied Physics, Aalto University, Helsinki, Finland
May 2021	Multiscale modelling of dislocation patterning SIAM Conference on Mathematical Aspects of Materials Science, Virtual

Organisation of conferences, workshops and symposia

2012	Member of the Local Organizing Committee for the ‘Dislocations 2012 - 4th international conference on fundamental properties of dislocations’, Budapest, Hungary
2017	Co-organiser of the CECAM-workshop entitled ‘Challenges in crystal plasticity: from discrete dislocations to continuum models’, Lugano, Switzerland

2018	Co-organiser of ‘Symposium L (Structure, Statistics and Mechanics in Crystal Dislocation Plasticity)’ at the ‘MMM (Multiscale Materials Modeling) 2018’ conference, Osaka, Japan
2019	Co-organiser of ‘Symposium S09 (Contemporary Experiments and New Devices in Secondary Physics Classrooms)’ at the ‘GIREP 2019’ conference, Budapest, Hungary
2020	Organiser of the topical day ‘Discrete-continuum transition of dislocation behavior’ at the ‘4th Schöntal Symposium’, Schöntal, Germany

Public activities

SINCE 2013	Member of the Council of the Faculty of Science of the Eötvös Loránd University
SINCE 2013	Member of the Council of the Institute of Physics of the Eötvös Loránd University (with right of consultation)
SINCE 2018	Member of the Committee for the Ericsson Prize
SINCE 2018	Member of the Committee for the ‘Rátz Tanár Úr’ Prize

2 Recent scientific work

2.1 Introduction

Already more than eight decades have passed since it became known that a certain line-like crystal defect is responsible for the plastic deformation of crystalline materials, the so-called dislocation (Fig. 2.1) [1–3]. The mechanism, first recognized simultaneously by Orován, Taylor and Polányi, proved successful in explaining numerous fundamental issues related to plasticity, yet, a vast amount of questions, most notably those related to the collective dynamics of dislocations, are still to be answered. One of the most known such problems is the pattern formation of dislocations. As well-known, upon deformation dislocations arrange into structures with properties depending on the type and extent of deformation. Although these patterns play a fundamental role in the mechanical properties, an in-depth physics-based theory of pattern formation is still elusive. The main reasons for the lack of such a theory are as follows:

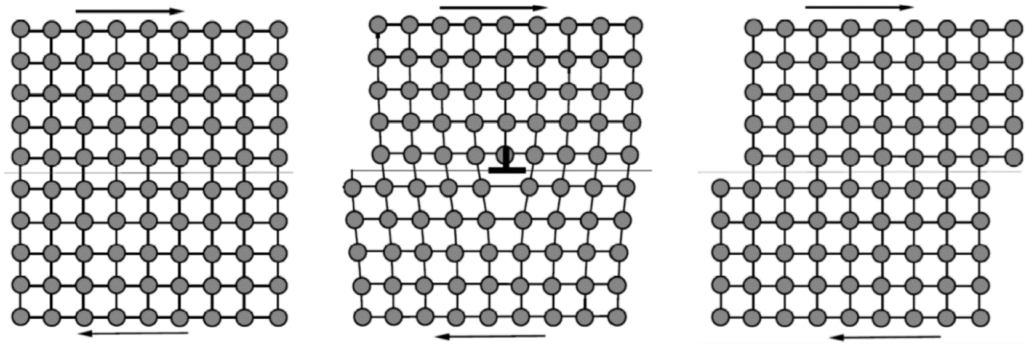

Figure 2.1: Schematics of an edge dislocation moving due to externally applied shear stress.

- Dislocation lines induce long range ($1/r$-type) stress fields in the material, so, the interaction of distant dislocation pairs cannot be neglected. Consequently, most of the classical thermodynamical concepts, since they assume short-range interparticle interactions, cannot be applied.
- The motion of dislocations is non-conservative due to the strong phonon drag. The role of thermal noise at low temperatures (that is, below approx. one third of the melting temperature) is negligible.

- Strong geometrical constrains apply for the motion of dislocation lines, since at low temperatures they can only glide in a certain plane (called glide plane). As a result, the system cannot reach its ground state, rather, it gets trapped in a meta-stable configuration. This means, that dislocation systems at low temperatures are far from equilibrium.

However, in the engineering practice it is essential to employ models that predict plastic deformation to certain precision. To fulfil this demand, several phenomenological models have been proposed that do not address the difficulties mentioned above thoroughly and usually provide constitutive relations between the stress, strain, strain rate and dislocation densities [4–8]. These models give satisfactory results under various specific conditions and sufficiently large sample sizes. In materials science currently the most widespread such model is the 'Crystal Plasticity Finite Element' method [9–11] which couples phenomenological plasticity models with an anisotropic elastic description. The model obtained proved capable of, e.g., modelling texture evolution in copper [12] or plasticity of nickel-based superalloys [13].

In summary, the phenomenological theories in many cases seem to be capable of describing the processes involving relevant dislocation motion. However, some of the breakthrough deformation experiments conducted around the millennium changed this view fundamentally. On the one hand, it turned out that if a characteristic scale of either the deformation volume or the sample itself (e.g., size of an indentor tip, size of the specimen, grain size or size of dispersoids) decreases to 1 μm or below, the mechanical properties start to differ considerably from the predictions of classical models [14, 15]. This phenomenon in materials science is referred to as *size effect*. On the other hand, it also became clear that size effects are accompanied by stochastic fluctuations. The first indication for this was delivered by *acoustic emission* (AE) measurements performed on ice single crystals, where it was found that the size distribution of the individual events of the burst-like AE signal follows a scale-free distribution [16, 17]. This suggested that plastic deformation is not a smooth process as phenomenological viscoplastic theories may suggest, rather deformation is, in fact, the accumulation of numerous independent scale-free distributed local plastic events. Subsequently, the spatial distribution of these events was also mapped and it was found that they originate from a fractal-like subvlume of the sample with dimension $\sim$2.5 [18].

The next milestone following the AE results described above were the deformation experiments performed on micron-scale cylindrical samples, called *micropillars*. With the development of scanning electron microscopy (SEM) technology it became possible to fabricate microscopic samples with nm precision with a focused ion beam (FIB), and their subsequent compression while obtaining the stress-strain relationship to high precision. The latter can be performed using a nanoindenter equipped with a flat punch diamond tip. The experiments were initially performed on Ni single crystal samples by Dimiduk and co-workers [19, 20]. Figure 2.2 presents SEM images obtained after the deformation for various micropillar sizes. It is evident

that with decreasing diameter deformation becomes more and more inhomogeneous as it gets localized in distinct slip bands. These bands, in fact, form due to the local plastic events which are also responsible for the emission of acoustic signals discussed in the previous paragraph.

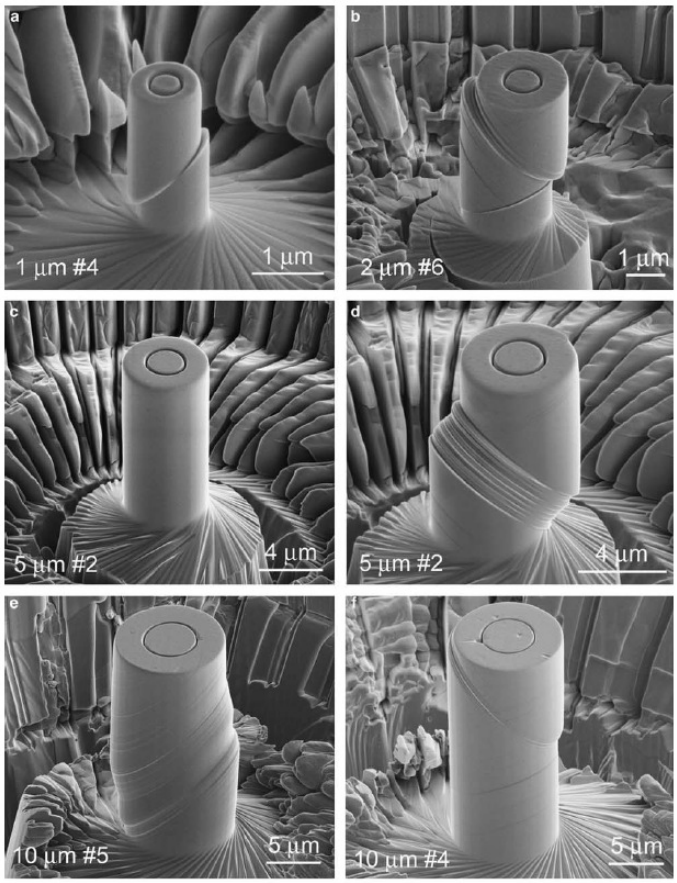

Figure 2.2: SEM images of deformed Ni single crystalline micropillars of various diameters. It is seen that for small samples deformation is localized in distinct slip bands and with increasing diameter deformation gets more homogeneous [20]. [Note that the sample in panel (c) is the undeformed initial state of the one seen in panel (d).]

The measured stress-strain curves of the micropillars are plotted in Fig. 2.3(a). In addition to the strong size effect (smaller samples are harder) it is visible, that for small sizes step-like features appear. These steps also correspond to the plastic events, that is, to the sudden appearance of individual slip bands. These events are, thus, also called *strain bursts* or *dislocation avalanches*. The stochasticity here means that micropillars prepared from the same sample with the same geometry exhibit different stress-strain responses: both the width of these steps as well as the strengths corresponding to their onset can be considered random variables. This remarkable observation is shown explicitly in Fig. 2.3(b). Note, that the scatter in the 'yield stress' is around 50% for pillars with a relatively large diameter of $\sim$10 μm. For smaller samples the effect is even stronger.

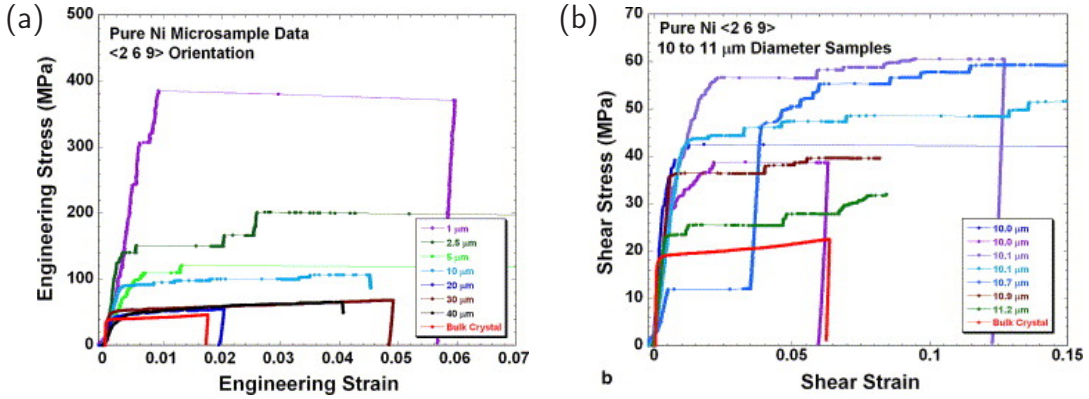

Figure 2.3: Stress-strain curves obtained during the compression of micropillars depicted in Fig. 2.2. The red curve corresponds to a bulk sample and the various colours denote micropillars with different diameters. (a): Curves corresponding to various diameters show a strong size effect. (b): Curves of micropillars with nearly equal diameters show the stochasticity of the response [20].

The statistical analysis of this random process mostly focused on the size distribution of the strain bursts. It turned out that, similarly to the distribution of AE events, they can be also characterized with a scale-free distribution [21, 22]. The practical relevance of this finding is that these random bursts prevent the predictable deformation of micron-scale objects. And from the theoretical point of view one can conclude that crystal plasticity is closely related to many other physical systems being far from equilibrium such as tectonic motion of the Earth's crust [23], migration of domain walls in ferromagnets due to external magnetic field [24] or the propagation of either liquid fronts in porous materials [25] or crack fronts in heterogeneous materials [26].

These stochastic features of plastic deformation immediately raised a focused interest of the community due to the fact that understanding micron-scale deformation had become a key issue with the rapid development of nanotechnology. The fact that phenomenological plasticity theories were not capable of describing these phenomena related to the fundamental properties of dislocations served as a driving force for the developments of statistical physics descriptions of dislocations. This was also assisted by the rapid increase in computational power that now lets us to simulate the dynamics of a large number of interacting dislocations. Yet, dislocation based modelling of a samples larger than few μm is still elusive due to the huge dislocation content and long-range interactions. So, the aim of the community is to develop physics-based mesoscopic models that may serve as a link between the properties of individual dislocations and experimentally observed macroscopic properties.

This scientific summary describes the recent research activities of the Author in this field. During this period, special emphasis was placed on the following aspects:

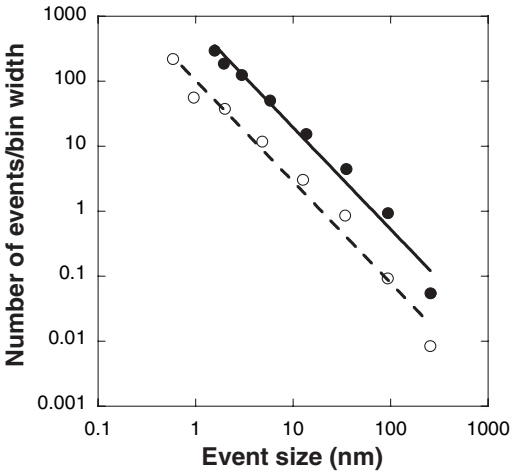

Figure 2.4: The size distribution of the strain bursts measured during the compression of the micropillars seen in Fig. 2.2. The open symbols represent data collected during the compression of a single micropillar with diameter of $\sim$20 μm, whereas full symbols stand for data summed over several such samples [21].

- The theoretical models of dislocation systems should contain as few free parameters as possible, yet, they should preserve the fundamental physical properties of dislocations described above.
- When possible, predictions of the mesoscopic models should be compared with lower scale discrete dislocation models.
- When possible, predictions should be also validated by experiments.
- To help validating theoretical results new experimental methodologies should be developed for the characterization of the dislocation microstructure and its dynamics on the micrometer scale.

The thesis is organised according to the methods used. The first section will focus on results obtained by the numerical analysis of discrete dislocation dynamics and a stochastic plasticity model. These, on the one hand, aim at the statistical description of the stochastic properties and, on the other hand, identify the anomalous scaling properties that stem from the universal scale-free nature of dislocation dynamics.

Results related to the continuum description of dislocation dynamics are presented in Sec. 2.3. This model considers the evolution of plastic deformation in terms of smooth dislocation density fields. After summarizing the reformulation of the theory into a variational framework results related to dislocation pattern formation will be presented. Finally, generalization of the theory for curved dislocations will be outlined that is a key step towards modeling realistic dislocation arrangements.

The last section focuses on experimental results. Firstly, statistical properties of micropillar compression will be presented and compared to predictions of numerical modelling. Secondly, the method of high-resolution electron backscatter diffraction (HR-EBSD) will be introduced which is capable of determining the dislocation structure close to the material surface. As shown, the applications of the method range from measuring the internal stress distribution to understanding dislocation interaction mechanisms during small-scale plastic deformation. Finally, results and prospects of the application of AE in micromechanics are discussed.

2.2 Stochastic properties of dislocation systems

2.2.1 Introduction

In order to understand the stochastic features of plasticity it is necessary to investigate this behaviour using physical models. The main reason for this is that during experiments the information one can gather is rather limited (mostly global properties, like stress or strain, or information from the sample surface) and one cannot access microscopic information like the precise position and speed of individual dislocations. In addition, for small samples (with volume of few μm^3) measurement errors may also play an important role. Possible sources of error include: (i) During FIB milling Ga^3+ ions get deposited at the surface making them harder to penetrate by dislocations, (ii) The elastic stiffness of the testing device has a strong influence on the avalanche dynamics and (iii) The geometry of the pillar is usually not regular but exhibits tapering [27].

Molecular dynamics simulations may seem adequate to study the collective behaviour of dislocations, where dislocation appear as line-like defects in the simulated crystal structure. Indeed, they have been used extensively to understand the specific features of nanoscale plasticity summarized above. However, limitations in computational power only constrains their use for a volume smaller than a few μm^3 and duration shorter than a few ns or for shock loading [28–31]. One, thus, cannot model the evolution of the system on atomic level but needs to use tools on higher scales. Since the elastic properties of dislocations in most materials depend only indirectly on the inter-atomic potentials one can substitute the crystal lattice between dislocations with an elastic continuum. Models obtained with this approach, thus, formulate equations of motion for individual dislocation lines and are called *discrete dislocation dynamics* (DDD) [32].

The model to be investigated is one of the simplest DDD systems that still incorporates the most important physical properties of dislocations summarized in the Introduction. The system consists of straight edge dislocations parallel with the z axis, and their slip plane is parallel with the xz plane (single slip). Since the system is translationally invariant along the z axis it can be considered two-dimensional (2D) and it is sufficient to track the motion of dislocations in the

xy plane. In this set-up the Burgers vector points in the x direction, so, reads as $\boldsymbol{b} = s(b,0)$, where $s \in \{+1,-1\}$ is the *sign* of the dislocation, that can be understood as some kind of charge. Figure 2.5(a) shows an example of such a 2D dislocation configuration. The colour of dislocations represents their sign and the background colour refers to the local shear stress within the embedding elastic medium.

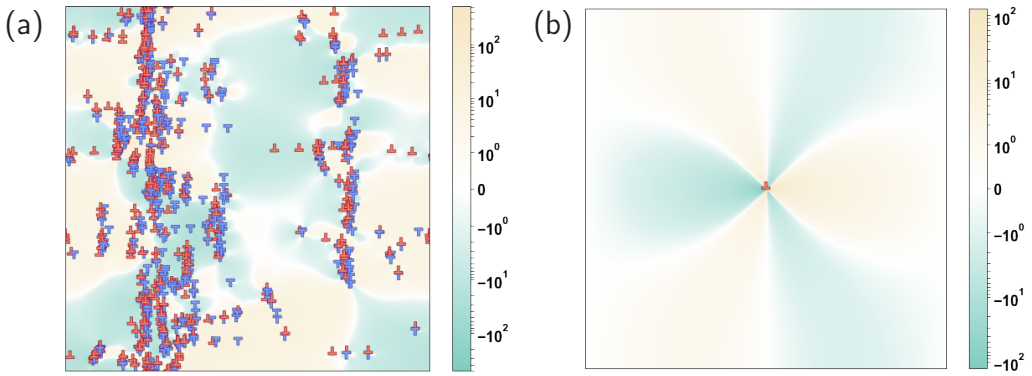

Figure 2.5: (a): 2D system of edge dislocations. (b): Shear stress field of individual dislocations with periodic boundary conditions.

Because of the strong dissipation due to phonon drag the motion of dislocations is assumed to be overdamped, that is, the force acting on a dislocation segment of unit length is proportional with its velocity. If the system consists of N dislocations and $\boldsymbol{r}_i = (x_i, y_i)$ denotes the position of the ith dislocation then the equation of motion reads as

$$\dot{x}_i = M s_i b \left[\sum_{j=1;\ j\neq i}^{N} s_j \tau_{\text{ind}}(\boldsymbol{r}_i - \boldsymbol{r}_j) + \tau_{\text{ext}} \right]; \qquad \dot{y}_i = 0. \quad (i = 1,\ldots,N) \tag{2.1}$$

Here M is the dislocation mobility, τ_{ext} is the externally applied shear stress and τ_{ind} is the shear stress field generated by individual dislocations. For the latter the solution corresponding to isotropic continua is used [33]:

$$\tau_{\text{ind}}(\boldsymbol{r}) = \frac{\mu b}{2\pi(1-\nu)} \frac{\cos(\varphi)\cos(2\varphi)}{r} = Gb \frac{\cos(\varphi)\cos(2\varphi)}{r} = Gb \frac{x(x^2-y^2)}{(x^2+y^2)^2}, \tag{2.2}$$

where μ and ν denotes the shear modulus and the Poisson number, respectively, and notation G was introduced for a combination of these elastic constants. Dislocations are arranged in a square-shaped simulation area and periodic boundary conditions (PBC) are applied. The emerging image dislocations alter the stress field of Eq. (2.2), which can be obtained using a Fourier method [see Fig. 2.5(b)] [34]. Further details about the implementation can be found in [A].

One of the main advantages of the model system introduced is that it preserves the $1/r$-type long-range dislocation interactions. This means that apart from the average dislocation spacing (being equal to $\rho^{-0.5}$, where ρ is the total dislocation density) no additional length scales appear in the model. One may, thus, introduce dimensionless variables that represent this scaling property by measuring length, stress, strain and time in units summarized in Table 2.1.

Quantity	length	stress	strain	time
Unit	$\rho^{-0.5}$	$Gb\rho^{0.5}$	$b\rho^{0.5}$	$\left(Gb^2M\rho\right)^{-1}$

Table 2.1: Units of the dimensionless quantities used in the simulations.

It is important to note that the studied system is a strong simplification of realistic dislocation networks found in crystals as it cannot account for dislocation multiplication, forest dislocations, the role of curvature, cross-slip, and dislocation reactions (such as the formation of Lomer-Cottrell locks).[1] Yet, it was successfully applied to describe Andrade-creep [17, 38], size distribution of dislocation avalanches [39–41], subgrain formation at elevated temperatures [42, 43], distribution of internal stresses [44, 45] and several statistical properties of the microplastic regime [46].

2.2.2 Plastic yielding in the sub-micron regime [A, D, F]

The fluctuations observed in the micron and submicron regimes make the stress-strain response random in several aspects. The step-like curves become a sequence of close to horizontal strain bursts connected by close to vertical stress increments (see Fig. 2.3). Both the bursts and the stress increments can be considered random variables that can be characterized with power-law [21, 22] and Weibull distributions [47], respectively. As a result, the stress corresponding to a given strain differs from sample to sample. The same is true for the yield stress, which for bulk materials is identified with the stress measured at 0.2% plastic strain. For micropillars this quantity is also stochastic and loses its universal nature being characteristic to the specific material only. In the literature, therefore, several new definitions of the yield stress were proposed at this scale, such as the stress at a given strain being larger than 0.2% [20], the stress at the onset of the first large strain burst [48] and the concept of 'Laue yield stress' was also introduced which is related to lattice rotations measured during *in situ* Laue-diffraction experiments [49]. The variety of the proposed methods raises the question what kind of physical process yielding corresponds to and whether a general definition of the yield stress exists that is not dependent on arbitrary parameters and the properties of the experimental device.

[1] It is noted that various extensions of this 2D model were proposed to account for these phenomena [35–37], but as these introduce various phenomenological length scales and we here focus on the role of the long-range interactions, we rather remain at the simplest version described above.

The fundamental hypothesis of the work described in the following was that at the micron level the yield stress can only be defined in a probabilistic sense for a set of samples with identical macroscopic parameters (size, crystal orientation, dislocation density, etc.) [A]. We, thus, performed 2D DDD simulations on a large ensemble. In every case, the system consisted of 64 positive and 64 negative sign dislocations initially arranged randomly in the simulation cell with uniform distribution. Firstly, the system was let to relax into a meta-stable state at zero stress, then the stress was increased with a constant small rate and the plastic strain γ was computed from the dislocation displacements as $\gamma = \sum_i s_i \Delta x_i$. Thin lines of Fig. 2.6(a) correspond to a few representative stress-strain curves obtained and indeed show the stochastic nature of the response. However, with averaging these curves (in this case, over 5000 realizations) the fluctuations disappear and one arrives at a smooth curve (thick red curve) typical for a bulk sample.

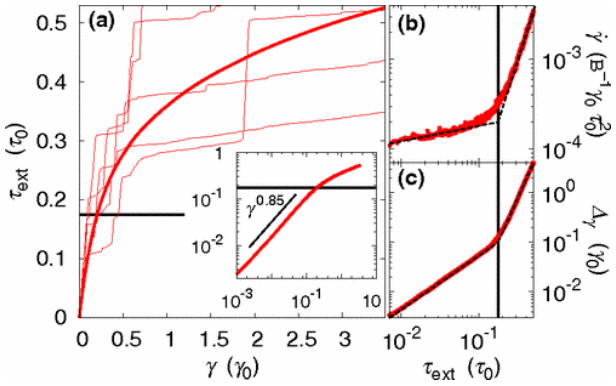

Figure 2.6: 2D DDD simulations with 128 dislocations. (a): Few representative stress-strain curves obtained from individual realizations (thin) and the average over an ensemble of 5000 realizations (thick). Inset: The average curve on a double logarithmic plot. The thick horizontal black line denotes the average yield stress. (b): Plastic deformation rate as a function of the applied stress. (c): Standard deviation of the plastic strain as a function of the applied stress [A].

Based on the average stress-strain curve one may split the plastic response into two regimes. For small stresses plastic strain increases as a power-law with an exponent $\sim$0.85, this can be identified with the microplastic regime. At larger loads, the curve deviates from the power-law and larger strains are measured. Based on this observation an average yield stress of $\tau_c \approx 0.17$ can be introduced that separates the two domains.

Figures 2.6(b) and 2.6(c) plot the average plastic deformation rate and the standard deviation of the plastic strain values of different realizations, respectively, as a function of the applied load. It is evident that the characteristic stress τ_c marks a sharp transition for these quantities, too.

The analysis of the velocity distribution of individual dislocations yields additional information about the dynamics of the system. Figure 2.7(a) shows the $P(v)$ distribution for various

external stress levels. In every case the distributions exhibit an inverse cubic decay, that is, for large velocities v

$$P(v) = Av^{-\lambda}, \tag{2.3}$$

where $\lambda \approx 3$ and the pre-factor A depends on τ_{ext}.[2] Figure 2.7(b) plots this $A(\tau_{\text{ext}})$ function and it is clear that, again, a well-defined shoulder is seen at τ_c.

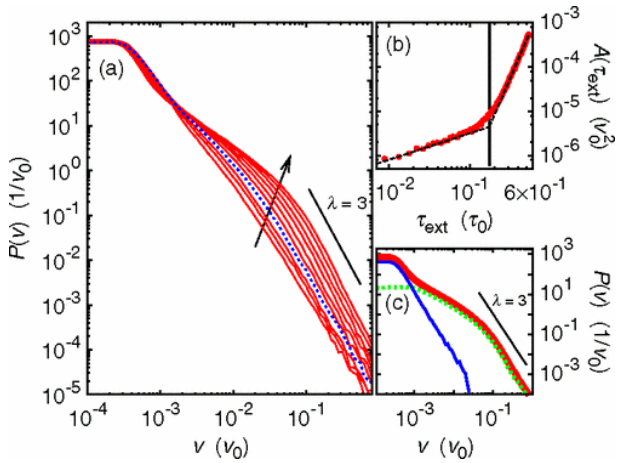

Figure 2.7: Velocity distribution of dislocations in 2D DDD simulations. (a): Distribution of velocities $P(v)$ for various external stresses τ_{ext}. The arrow indicates the increase of τ_{ext} and the blue dashed line is the distribution corresponding to $\tau_{\text{ext}} = \tau_c$. (b): The pre-factor of the inverse cubic tail A as a function of the external load. (c): Above τ_c distribution $P(v)$ can be decomposed into the contribution of the avalanches (dashed green) and systems in a quiescent state (continuous blue) [A].

In individual realizations the deformation process is a sequence of two alternating states: there are irreversible deformation avalanches (strain bursts) with quasi-reversible quiescent states in-between (for a detailed analysis the reader the referred to [F]). In Fig. 2.7(c) the velocity distribution was determined independently for systems in either avalanche or quiescent state. It is seen that the appearance of the shoulder in $P(v)$ [Fig. 2.7(a)] and, therefore, to the yielding phenomenon is due to the rapidly increasing number of dislocation avalanches above τ_c [A].

In summary, the threshold stress τ_c was found to separate two regimes with different dynamic behaviour, thus it can be identified with an average yield stress. This result is not specific to 2D systems as similar behaviour was found in more complex 3D DDD simulations and micropillar experiments as well (see also Sec. 2.4.2) [D].

[2] The theoretical background of the origin of the exponent is described in [A].

2.2.3 Scale-free dynamics in discrete dislocation systems [C, E, S]

As it was mentioned in the previous section 2D DDD simulations usually start with a random initial configuration that is first relaxed at zero stress. In this section, first, we investigate this relaxation process in more detail. As a tool we employ the velocity distribution of dislocations $P(v)$ introduced above. Obviously, dislocations move quickly during the initial, close-to-random state and slow down gradually until they stop when the system reaches equilibrium, so, the velocity distribution also depends on time t. Interestingly, according to Fig. 2.8(a) the $P(v,t)$ distributions can be collapsed on a master curve using the scaling relation

$$P(v,t) = t^{\alpha} f(t^{\alpha} v). \tag{2.4}$$

The exponent α was found to be $\alpha = 0.85 \pm 0.02$ and the scaling function f can be well approximated by the form $f(x) \approx A/(Bx^3+1)$ (note, that the inverse cubic tail is again recovered).

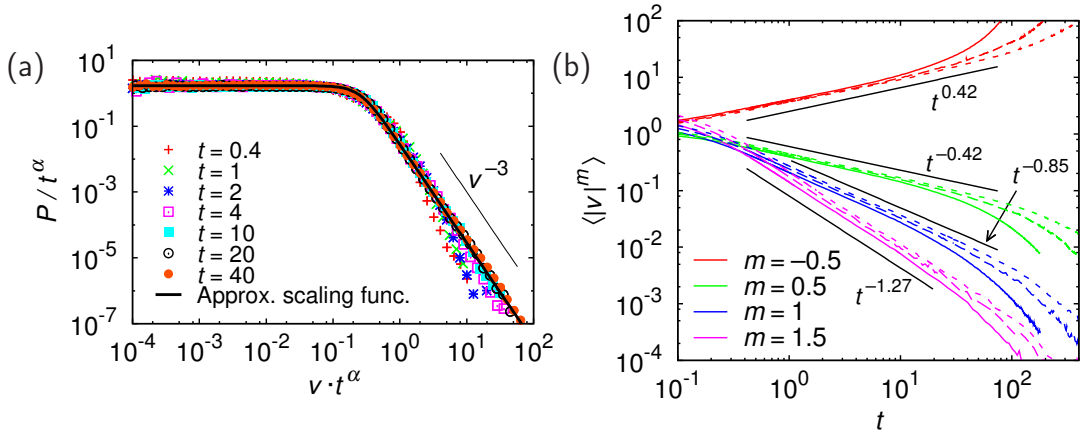

Figure 2.8: Dynamics during relaxation from a random configuration. (a): The scaled velocity distributions of dislocations $P(v,t)$ given by Eq. (2.4) with $\alpha = 0.85$ at system size $N = 2048$, and the approximated fitted scaling function (see text). (b): The moments $\langle |v(t)|^m \rangle$ for different exponents m (identified by colours) and dislocation numbers N. The solid, dashed, and dotted lines correspond to $N = 128$, 512, and 2048, respectively [C].

In order to investigate this scaling behavior in more detail, the mth moment $\langle |v(t)|^m \rangle$ of the absolute velocity was also determined for different m values. According to Eq. (2.4)

$$\langle |v(t)|^m \rangle = \int |v|^m P(v,t) \mathrm{d}v = C_m t^{-m\alpha}, \tag{2.5}$$

where C_m is a constant. (Because of the asymptotic properties of the scaling function f, the integral is finite only for $-1 < m < 2$.) Figure 2.8(b) shows the measured $\langle |v(t)|^m \rangle$ curves for different m values and system sizes. The fitted exponents are in agreement with Eq. (2.5). (With

the same simulation setup the scaling regime and the value of α has been already reported in [50].)

As seen in Fig. 2.8(b) the scaling region is bounded from both sides. It starts at a fixed $t_0 \approx 0.4$ and lasts till a cut-off time t_1 increasing with linear system size $L = \sqrt{N}$ as obtained from fitting an exponential cutoff. This is in accordance to what is usually found in systems with long-range interactions. To analyse this behaviour in more detail, additional simulation scenarios were studied, namely, perturbation by an externally added dislocation and creep response to applied stress. Both of these yielded equivalent velocity scaling, albeit with different exponents [C].

In summary, power-law relaxation of dislocation systems was observed in different scenarios. This effect may be attributed to the quenched random positions of the slip axes, the complex nature of the interactions and their long-rangeness. Remarkably, the scaling of the time-dependent velocity distribution goes with different exponents depending on the physical setup. Scaling is cut off due to the finite size, so the system does not possess any inherent time scale. The dislocation system is, therefore, found to behave like a critical one in all cases considered, strongly resembling glassy systems [C].

As it was explained in the Introduction in detail, the strain fluctuations observed in micron-scale plasticity are in many aspects analogous to other physical systems exhibiting criticality. In particular, several researchers have advanced the idea that the dislocations in a crystal deforming under stress might be envisaged as a driven non-equilibrium system, where power-law distributed avalanches arise from dynamic critical behavior associated with a non-equilibrium phase transition at a critical value $\tau_{\text{ext}} = \tau_{\text{c}}$ of the externally applied stress, analogous to the depinning transition of elastic interfaces in random media [51]. This idea applies in a straightforward manner to single dislocations interacting with immobile impurities which provide a textbook example of one-dimensional elastic manifolds undergoing a depinning transition [52, 53, S]. In generalization of this observation, several authors have argued that the mean-field limit of the depinning transition (mean-field depinning, MFD) might correctly describe the dynamics of stress-driven many-dislocation systems even when other defects are absent [41, 46, 54–57].

To unambiguously determine the nature of criticality associated with the strain bursts and the yielding transition we analysed 2D DDD simulations with continuous time dynamics (CTD) described above as well as two other cellular automaton (CA) based DDD models one with extremal dynamics (ED) and another with random dynamics (RD) (for details see [E]). In each case a quasistatic stress-controlled loading protocol was implemented. For each model, we consider the avalanche size distribution $P(s)$ at different levels of the external stress below the yield stress (s being the total plastic slip defined as $s = \sum_i s_i \Delta x_i$, where Δx_i is the dislacement of the ith dislocation during the avalanche). For $s > 1$ (i.e., slip events larger than that corresponding

Model	τ	β	σ_0
CTD	0.97 ± 0.03	0.36 ± 0.04	0.07 ± 0.01
CA with ED	1.00 ± 0.03	0.36 ± 0.02	0.116 ± 0.004
CA with RD	1.02 ± 0.01	0.44 ± 0.01	0.122 ± 0.002

Table 2.2: Parameters of Eqs. (2.6) and (2.7) obtained by fitting to the numerically obtained avalanche distributions [E].

to a single dislocation moving one average dislocation spacing), these can be well characterized by a power law with a cut-off,

$$P(s) \propto s^{-\tau} f(s/s_0). \tag{2.6}$$

To estimate τ and s_0, a fitting procedure was utilized that fits Eq. (2.6) simultaneously using a maximum likelihood estimation to the avalanche distributions obtained at different stress levels and system sizes. The cutoff was found to follow

$$s_0(\sigma_{\text{ext}}, N) \propto N^{\beta} \exp(\sigma_{\text{ext}}/\sigma_0). \tag{2.7}$$

Table 2.2 presents the parameters obtained by fitting Eqs. (2.6) and (2.7) to the avalanche size distributions. Figs. 2.9(a-c) show the $P(s)$ distributions for the three models plotted as functions of s/s_0. The validity of Eq. (2.7) is demonstrated by the collapse of all distributions in the cutoff region. Since Eq. (2.6) holds only for $s > 1$, the curves follow the master curve only as long as $s/s_0 > 1/s_0$, thus over longer range as the applied stress and/or the system size increase. Below this regime the behavior is governed by the single-dislocation dynamics and therefore differs between the three models.

The observations summarized by Eqs. (2.6), (2.7) and Table 2.2 exhibit several interesting features:

(i) The power law exponent τ has the value $\tau \approx 1.0$, clearly different from the MFD value $\tau = 1.5$. According to Fig. 2.9(d), the integrated distribution (where avalanches with all stress values are considered together) exhibits a larger exponent $\tau_{\text{int}} \approx 1.3$, in line with a subsequent reanalysis of experimental micropillar compression data [58]. Moreover, the inset of Fig. 2.9(d) shows that in the CTD model, the avalanche size scales with the duration as $s \propto T^{\gamma}$, with $\gamma \approx 1.32$ clearly different from the MFD value of 2.

(ii) According to Eq. (2.7), the cutoff s_0 increases with system size even at very small applied stress like $s_0 \propto N^{\beta}$ with $\beta \approx 0.4$.

(iii) The cutoff s_0 does not diverge at a certain external stress, rather it exhibits an exponential stress dependence.

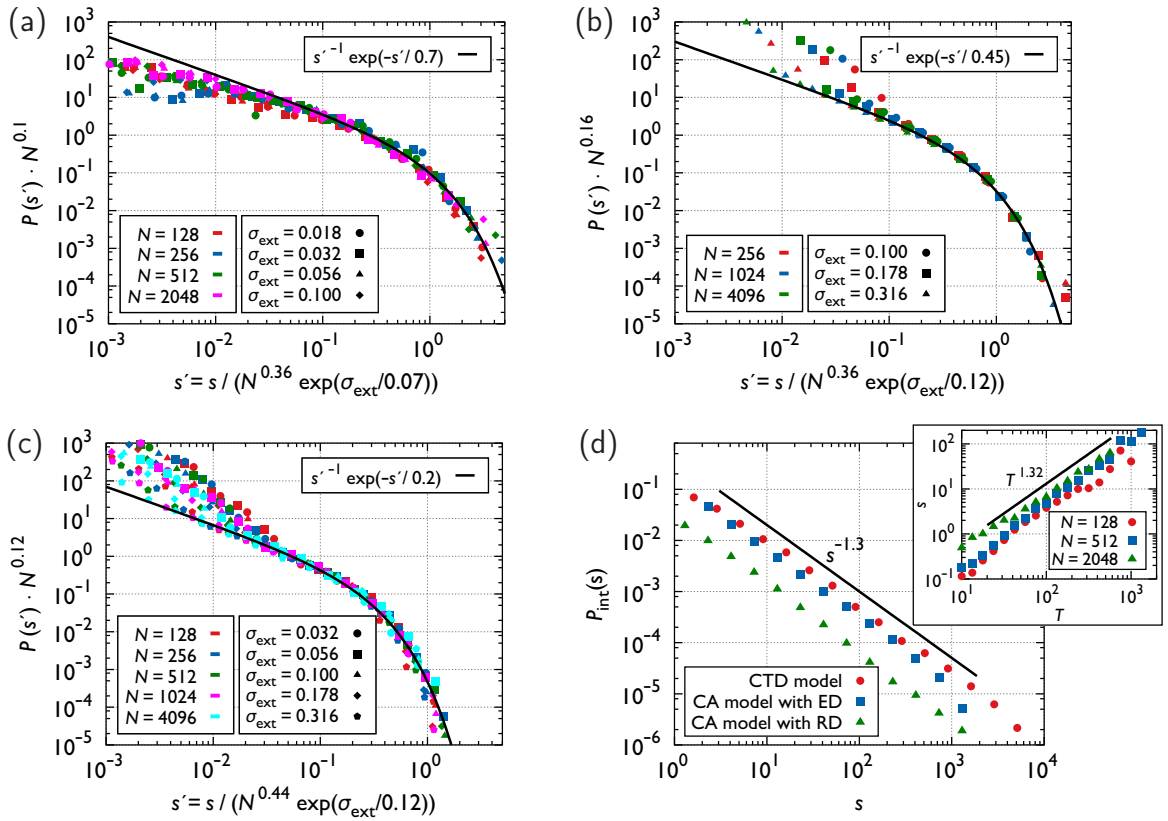

Figure 2.9: (color online) (a-c): Stress-resolved distributions of avalanche sizes for the various DDD models at different applied stresses and system sizes. The distributions are plotted as functions of $s' := s/s_0$, with s_0 obeying Eq. (2.7). (a): CTD model, (b): CA model with ED, (c): CA model with RD. (d): Aggregate avalanche size distributions P_{int} integrated over σ_{ext} for system sizes $N = 512$ (CDT model) and $N = 4096$ (CA models). Inset: Scaling of the avalanche size s with the duration T in the CTD model, for three different system sizes N [E].

The fundamental difference between the present and depinning behaviour is highlighted in Fig. 2.10, where the average avalanche size is compared for the CA DDD model with ED and a simple depinning model. In the latter an elastic line with $1/r$-type self-interaction is driven through a random pinning field.

To conclude, it was established that the statistics of slip avalanches in simple 2D DDD models is inconsistent with a depinning transition. Fundamental differences between the behavior of dislocation systems and the interface pinning/depinning scenario are manifested by the behavior of the cut-off of the avalanche size distribution which, rather than diverging at some critical stress τ_c, scales exponentially with stress but diverges with system size at every stress. In addition, the avalanche exponent $\tau \approx 1.0$ is inconsistent with MFD. These scale-free properties add to the slow relaxation described in the previous section and mean that single slip dislocation systems are, in fact, always in a critical state regardless of the applied stress. It is noted, that short-range interactions, such as point-defects, junctions, grain boundaries etc., are absent in this model and they may change the critical behaviour of the system, see, e.g, [59–61].

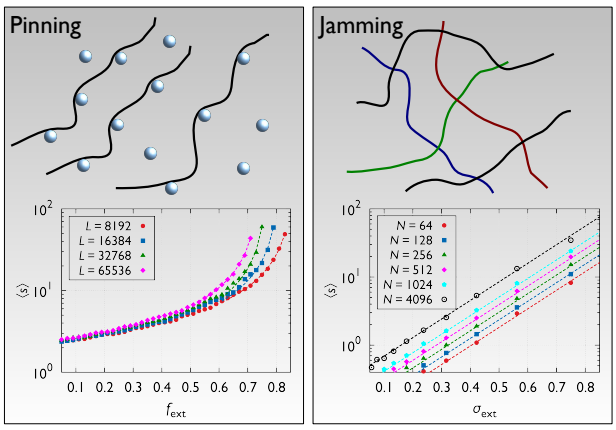

Figure 2.10: Differences between pinning and the present jamming scenario. Pinning is induced by quenched disorder which stops the motion of driven elastic manifolds for applied forces f_{ext} below a critical value f_c (top left). With f_{ext} approaching f_c from below, the manifold moves ahead in avalanches with an average avalanche size $\langle s \rangle$ which in MFD diverges as $\langle s \rangle \propto (f_c(L) - f_{\text{ext}})^{-1}$ ($1d$ elastic manifold with elastic interactions decaying as $1/r$, bottom left). f_c depends on the system size L due to finite size scaling, $f_c(L) = f_c(\infty) + aL^{-1}$. In a dislocation system without quenched disorder, dislocation motion may stop due to formation of jammed configurations (top right). The behavior of $\langle s \rangle$ we observe in this case is fundamentally different from the depinning scenario, with $\langle s \rangle = A(N)e^{\sigma_{\text{ext}}/\sigma_0}$, where $A(N)$ grows with the number of dislocations N (bottom right) [E].

2.2.4 Statistics of internal disorder [I, J]

In Sec. 2.2.2 the average stress-strain curve of 2D dislocation systems was analyzed. Here the distribution behind the average is investigated and its dependence on the system size. Figure 2.11 plots the cumulative distribution Φ_γ of applied stress values τ at a given value of plastic strain γ for different realizations of the dislocation system. The three panels correspond to different strain values. One can observe that (i) the average of the distributions increase with the strain (as was seen earlier on the average stress-strain curves in Sec. 2.2.2), (ii) fluctuations of the applied stresses decrease with increasing system size at all three studied strain values and (iii) the curves corresponding to different system sizes intersect each other in a single point, hereafter denoted by $\langle \tau \rangle(\gamma)$. The last observation suggests that in the thermodynamic limit (i.e., $L \to \infty$) the curves tend to a stepfunction at $\langle \tau \rangle(\gamma)$. In addition, it also hints at a scaling property of the curves. Indeed, according to the inset plots of Fig. 2.11 functions Φ_γ obey the following scaling law:

$$\Phi_\gamma(\tau) = \frac{1}{2}\left[1 + \text{erf}\left(\frac{\tau - \langle \tau \rangle(\gamma)}{cL^{-\theta}}\right)\right], \tag{2.8}$$

where fitting yields for the exponent $\theta = 0.8 \pm 0.05$. Finally it is noted that the usage of the erf function implies that the stress values follow a normal distribution.

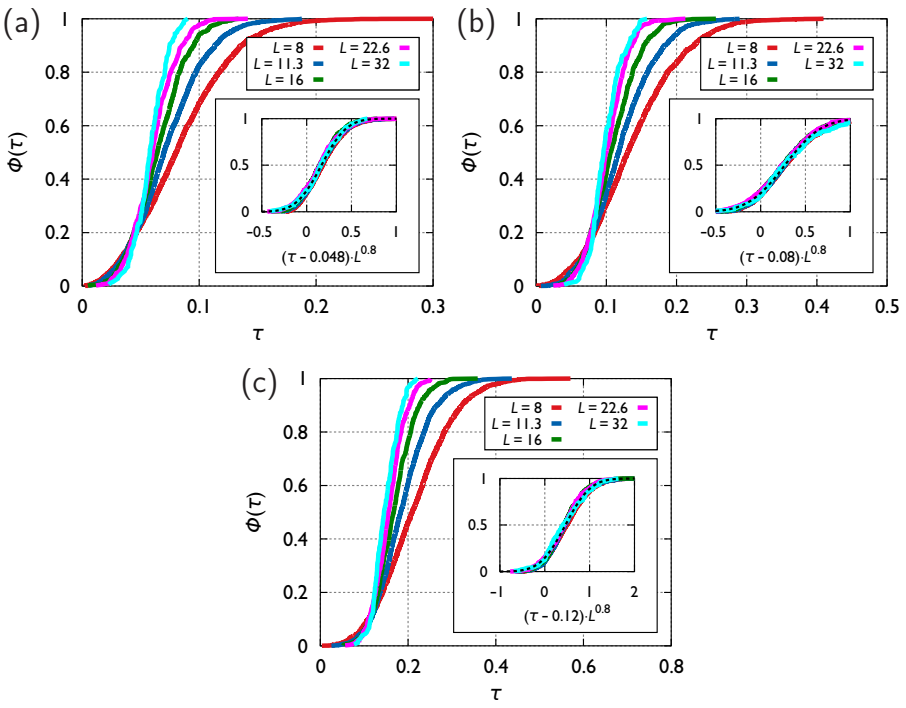

Figure 2.11: Cumulative stress distributions Φ_γ at different strain levels γ, DDD model. Scaling collapse can be obtained by multiplying the external stress with a power of the system size [Eq. (2.8)]. The so collapsed curves can be fitted by an appropriate normal distribution (dashed lines). (a): $\gamma = 0.05$, (b): $\gamma = 0.1$, (c): $\gamma = 0.2$ [I].

To rationalize these findings a simple plasticity model based on order statistics was proposed. Firstly, it was assumed that the material can be decomposed into local units, each characterized by a yield threshold accounting for the inhomogeneity of the underlying microstructure (e.g., dislocation patterns). This non-trivial assumption implies that the distribution of the stress at the onset of the first plastic event, must follow a weakest link distribution. In accordance with Derlet and Maass [62], the distribution of the yield thresholds is assumed to be asymptotically scale-free characterized with exponent β. In this model the stress-strain curve is assumed to be perfectly step-like, with each step corresponding to a random strain burst followed by a random stress increment. The former is modelled as a sequence of independent random variables whereas the stress values corresponding to the onset of subsequent events are assumed to originate from the weakest link sequence. After each event the material gets harder, because the subsequent events take place at the second, third, etc. weakest spot. This sequence is determined by the shape parameter β, and thus the exponent β emerges as a central parameter that also influences the power-law exponent of the plastic stress-strain relation, that is, the amount of plasticity in the microplastic regime [I]. The origin of $\beta \approx 1.4$ for DDD systems was not addressed, it may be influenced by the internal structure of dislocation arrangements, like slip systems, patterns, etc. It is noted, however, that a similar analysis of the average stress-strain

curves performed earlier on 3D DDD simulations and micropillar compression experiments yielded $\beta \approx 1.4$ in both cases [A,D], hinting at some generality of the exponent β.

In order to account for fluctuations in the plastic response on a higher scale model stochastic continuum plasticity models (SCPMs) were introduced [54, 63–67]. In these models the internal disorder is represented by a local yield stress that is considered a spatially fluctuating random variable. Wherever the local stress at a given cell exceeds the local threshold plastic strain is accumulated in that cell giving rise to the anisotropic redistribution of the internal stress within the material. The form of the corresponding elastic stress kernel can be obtained using an Eshelby-type solution of the inclusion problem [68]. In these models the most important input is the distribution of the local yield thresholds that represents the statistical details of the microstructure. This means that the simple theoretical model outlined above that is based on the subsequent activation of the weakest links delivered a method how to calibrate the parameters of the SCPM based on lower-scale DDD simulations [I]. The proposed methodology does not only represent a bridge between micro- and mesoscales, but also gives insight into the nature of the stochastic processes characterizing plasticity.

To understand the role and importance of the yield stress distribution its effect on strain localisation was investigated in materials exhibiting shear softening [J]. A most prominent example of this type of behaviour are metallic glasses – a class of materials with potentially outstanding mechanical properties (for recent overviews of the mechanical behavior of metallic glasses, see [69, 70]) but whose application is hindered by a propensity to fail shortly after yield by catastrophic shear band formation. In order to model this phenomenon, an SCPM was implemented with Weibull-distributed yield stresses with different shape parameters β. It is important to note, that larger β implies a smaller scatter of local yield stresses, i.e., a lower degree of microstructural disorder in the material. As seen in Fig. 2.12 larger disorder ($\beta = 1$) leads to an extended plastic regime and an increased yield strength whereas at small disorder ($\beta = 4$) the elastic regime is immediately followed by the failure of the material.

Figure 2.13 illustrates the changes in the strain patterns that occur during the softening regime. At the peak stress before the onset of softening, deformation is macroscopically homogeneous but exhibits mesoscale patterns in the form of numerous diffuse shear bands which follow the planes of maximum shear stress, here aligned with the x and y directions. These patterns are more pronounced with increasing degree of disorder. Note that the peak stress is reached later in the more disordered sample (top left graph in Fig. 2.13), hence the overall strain is bigger. During the softening regime we observe a qualitative change in the patterns as most of the additional strain accruing during the softening regime is localized in a single shear band which also contains the location where microcrack nucleation takes place. The localisation process was quantitatively analysed and a local criterion was also established for the propagation of the formed embryonic microcracks. In general it was shown that increased microstructural

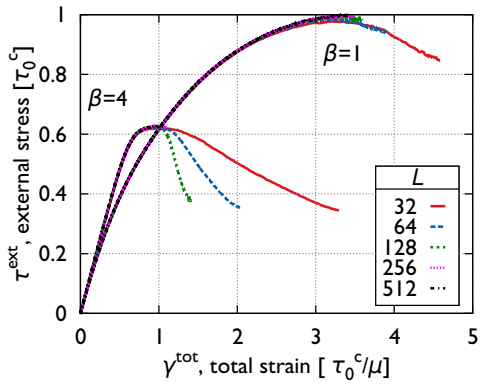

Figure 2.12: Stress–total strain curves for two different yield-stress distributions (Weibull exponents $\beta = 1$ and $\beta = 4$) and different system sizes L. For details see [J].

heterogeneity in a one-phase material delays strain localization and leads to an increase of the plastic regime in the macroscopic stress–strain curves [J].

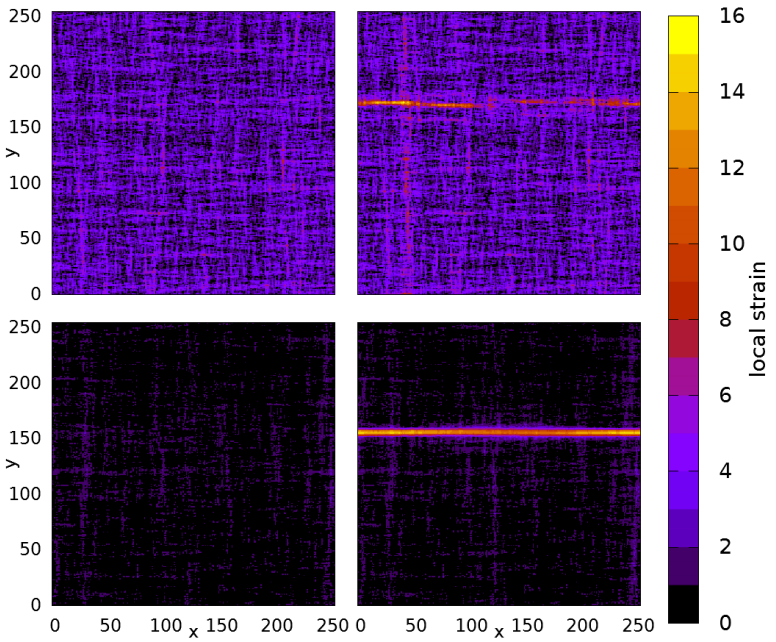

Figure 2.13: Strain patters at the highest external stress just before the onset of softening (left) and at the end of the simulation (right); $\beta = 1$ (top) and $\beta = 4$ (bottom). For details see [J].

2.2.5 Numerical methods [P, Q]

It was already seen in this chapter how important role is played by DDD simulations in materials science research. They are not only important because of their capacity in modelling various deformation phenomena but also because they may be used to validate higher scale plasticity

models that are indispensable for technological applications. Being of central importance, the numerical efficiency of the simulations is also a crucial issue. Two significant improvements will be discussed in this section, one related to the integration scheme the other to the boundary conditions.

Due to the $1/r$-type interactions one concludes that the differential equation system that describes the dynamics of dislocations or dislocation segments [Eq. (2.1) for 2D DDD] is stiff. In such cases explicit methods are inefficient, because the achievable time-step is limited by the shortest timescale in the system, which is determined by the closest dislocation dipole. This typically leads to a very slow propagation of the simulations even when the system is stationary. Nonetheless, most of the simulators are based on explicit methods [35, 71–73]. This issue can be solved by implicit schemes [72]. Sills *et al.* showed that with the help of the simple implicit trapezoidal method and the Newton-Raphson non-linear solver, in certain scenarios a speedup is achievable compared to the default Heun-method of ParaDiS (a 3D DDD simulation implementation) if a sparse matrix was used. This was achieved by taking into account only short range elastic interactions in the Jacobian, defined with a fixed limit on the distance [72]. Gardner *et al.* applied diagonally implicit Runge-Kutta methods and concluded that with high number of dislocation segments the gain in the stepsize compared to explicit methods was not large enough to compensate for the increase in the time needed to calculate one step [74]. Both of these studies were done using ParaDiS or DDLab (which is the serial version of ParaDiS written in MATLAB).

Motivated by these studies we introduced a novel implicit method for our 2D DDD simulations with adaptive stepsize control [P]. A weighted trapezoidal scheme was employed with specific weight factors in order to decrease oscillations around equilibrium and resulting numerical noise. A cut-off parameter r_c was also introduced in the Jacobain matrix with the following properties:

- At $r_c = \infty$ (that is, without using the cut-off functions) the numerical noise can be decreased down to floating point precision and the simulation timestep at equilibrium can practically diverge. These optimal properties are somewhat flawed by an increased computational cost of a single timestep because the Jacobian matrix is dense due to the long-range nature of interactions. In fact, the complexity of computing a single timestep is larger than that of the explicit methods [being $\mathcal{O}(N^3)$ instead of $\mathcal{O}(N^2)$], so for large systems the implicit method with $r_c = \infty$ only close to equilibrium may be more efficient than traditional explicit methods, because here the gain in the timestep can be large enough to compensate for the slower calculation of a single timestep.

- At finite cut-off r_c an in between method is obtained: On the one hand, it makes the Jacobian sparse thus decreasing the complexity of a timestep to $\mathcal{O}(N^2)$, thus, it becomes

efficient for large system sizes, too. On the other hand, it still allows the stepsize to be significantly larger than that of explicit schemes. It, in fact, acts similarly to the annihilation distance of explicit methods: dipoles with distance smaller than r_c are treated implicitly (and thus not limiting the timestep) whereas those with distance larger than r_c are computed explicitly and do limit the timestep even at equilibrium. The advantage is, that the small dipoles here do not have to be annihilated, and their dynamics are still solved with high precision. It was found that the runtime of the new method was approximately 4 orders of magnitude lower than that of the explicit method with a realistic annihilation distance.

The results indicated that when activity was high in the system a smaller value of r_c was the most efficient and as activity ceased an increasing value of r_c showed better performance. Future work will aim at developing an algorithm that dynamically modifies the value of r_c based on the dynamic properties of the system. Such a method could further improve the efficiency of this scheme. In addition, significant increase in computational speed can be expected from porting the source code to GPU [P].

In another work the handling of boundary conditions were investigated [Q]. In all of the problems considered so far in this chapter PBCs were employed. Realistic boundary conditions, however, either prescribe stress or displacement (or their combination). For large systems the type of the boundary is not expected to play a significant role but as soon as size effects are to be investigated and the system size is reduced to the micron scale, PBCs are no longer applicable. To implement realistic boundary conditions a certain elastostatic problem needs to be solved at every timestep of the simulation. This is typically done using the finite element method (FEM). This versatile and flexible tool allows one to study various geometries and boundary conditions with high numerical stability. Despite the advantages of the FEM, in some cases different methods may suit the investigated problem better and may, e.g., exhibit faster runtime compared to FEM. It was shown, for instance, by Wei *et al.* that a particular spectral method has superior time complexity compared to FEM when modelling 3D DDD in a cylindrical micropillar geometry [75]. This method is based on the series expansion of the analytical elastic solution and the boundary conditions are prescribed in terms of Fourier coefficients of the desired boundary values.

Our aim was to develop a spectral method to efficiently handle the boundary problem for 2D systems, so we followed the route proposed by Wei *et al.* The introduced method is able to solve Dirichlet, Neumann and mixed boundary value problems as well. Since, the solution is a linear combination of basis functions which satisfy the Navier–Cauchy equations exactly, in principle, it also fulfils the elastic equations exactly in the volume. However, the boundary conditions are only met approximately. The basis we use is finite, therefore, the possible solutions one can reproduce with this method are from a subspace of all solutions of the Navier—Cauchy

equation. Thus, we had to find the approximate solution in this subspace that is the closest to the genuine solution in some sense. The proposed requirement is that the first finite number of Fourier coefficients of the Fourier series of the approximate solution on the boundary should be identical to the Fourier coefficients of the boundary condition.

Firstly, our method was tested on analytically solvable problems such as pure shear. The method reproduced the analytical solution and showed remarkable fast exponential convergence with the increment of the basis size which is superior to the power-law convergence of FEM. Secondly, the method was applied to cases where the simulation cell contained a dislocation. It was found that if a dislocation is closer to the boundary than a certain distance (which decreases at higher orders of computation) numerical errors appear due to the analytically diverging stress fields. Based on this observation the time complexity that is needed to achieve a certain precision was assessed. As it was discussed in detail in [Q], the solution of the PDE leads to a $\boldsymbol{c} = \boldsymbol{M}^{-1}\boldsymbol{f}$ type multiplication, where vector $\boldsymbol{f}$ can be obtained from the prescribed boundary values, matrix $\boldsymbol{M}$ is characteristic to the type of boundaries and vector $\boldsymbol{c}$ characterizes the solution function. In a typical application the matrix $\boldsymbol{M}$ is unchanged during a simulation even if the boundary values change (but remains of the same type, for instance Dirichlet), hence, it is enough to evaluate and invert the matrix once, while the vector $\boldsymbol{f}$ should be calculated at every time step. Naturally, the subtasks that should be done at every time step will be the ones that determine the computational efficiency of the method. After investigating the computational time of these subtasks we concluded that the computational complexity of our method is $\mathcal{O}\left(N_{\mathrm{dis}}^{3/2}\right)$, that is, $\mathcal{O}\left(L^3\right)$ where N_{dis} and L are the total number of dislocations considered and the characteristic linear system size, respectively. Thus, contrary to FEM, the computational complexity of our numerical method is more favourable than the calculation of dislocation-dislocation interactions in DDD simulations [being $\mathcal{O}(N_{\mathrm{dis}}^2)$ or, equivalently, $\mathcal{O}(L^4)$]. Consequently, taking the boundary conditions into account will have a lower computational cost compared to other tasks, therefore, this component of the simulation will not limit the dislocation number (or system size) we are able to investigate in reasonable time. This will allow us to examine larger systems and gain better statistics (of, for example, dislocation avalanches) [Q].

2.3 Continuum theory of dislocations

2.3.1 Introduction

Plastic deformation of crystalline materials is largely controlled by the motion of dislocations, that are line-type topological lattice defects. Since the typical dislocation density in deformed metals is in the order of at least $\rho \approx 10^{14}$ m^{-2}, the average spacing between dislocation lines is less than 100 nm. This means that already micron sized samples contain a vast amount

of strongly interacting dislocations. As a consequence, to model the plastic deformation of crystalline materials in terms of dislocations one has to handle the problem with statistical physics methods. However, there are two caveats for the direct application of methods from statistical physics to dislocation systems: (i) dislocation motion is strongly dissipative, and (ii) dislocations are flexible lines, inhibiting their treatment as point-particles.

The development of a statistical continuum theory of dislocations was initially motivated by the occurrence of size-effects [76] in the plastic response of samples with characteristic dimensions on the order of 10 μm or less. Attempts to incorporate internal length scales into phenomenological continuum theories by considering so-called strain-gradients [77–80], did not yield a satisfying solution for general loading cases. Another key issue to be addressed is the ubiquitously observed dislocation pattern formation during plastic deformation. Since the early 1960s several theoretical and numerical attempts have been suggested, initially based on analogies with other physical problems like spinodal decomposition [81], internal energy minimization [82], or chemical reaction-diffusion systems [83, 84]. Since, however, they are not directly linked to the specific properties of individual dislocations they are fundamentally phenomenological approaches. Dislocation patterning was also an important motivation for the development of the discrete dislocation dynamics (DDD) method addressed in the previous section of this thesis [85–88]. But due to the long range dislocation-dislocation interaction the simulations are computationally extremely expensive and the study of dislocation patterning with DDD is still limited to specific problems like irregular clusters or veins [87–89]. Recently, El-Azab and coworkers [90, 91] used a continuum formulation based on vector dislocation densities in large-scale numerical simulations, which seem to feature the evolution of dislocation patterns. However, this pseudo-continuum variant of DDD is a numerical rather than a theoretical model of dislocation patterning.

The two caveats for developing a statistical continuum theory of dislocations named in the first paragraph were approached largely independently from each other. The consequences of the dissipative nature of dislocation motion has been thoroughly explored in strongly simplified quasi two-dimensional systems of straight parallel edge dislocations, where dislocations are treated as signed point particles moving in a plane (see Sec. 2.2.1). By a systematic coarse-graining of the evolution equations of individual dislocations [92–97] a continuum theory was developed, that was successfully compared to DDD simulations [94, 98, 99]. In Sec. 2.3.2 it will be shown how the theory can be formulated as a phase field theory whereas Sec. 2.3.3 will focus on the application of the continuum theory to describe and understand pattern formation of dislocations.

The second caveat, that is the fact that dislocations are moving flexible lines entails the question, what are suitable continuum variables allowing for a closed system of conservation laws for dislocation systems. This has been answered in a primarily kinematic theory of curved dislocations, which was developed by Hochrainer *et al.* [100–104]. The kinematics were initially

derived in a higher dimensional space, containing the line direction as independent variable. A multipole expansion of the theory leads to a formulation in terms of alignment tensors, which, in the case of only planar dislocations on parallel glide planes, is equivalent to a Fourier expansion. The resulting conservation laws may be used to derive 'kinetic' theories from a thermodynamic potential with standard methods from irreversible thermodynamics. This yields forms of driving forces [105], naturally generalizing those found in the quasi-two-dimensional theory. The phase field approach of Sec. 2.3.2, however, provides a straightforward toolbox to generalize the 2D theory to 3D to arrive at a physics-based dynamic continuum theory of dislocations. These attempts will be summarized in Sec. 2.3.4 along with the activities that aim at comparing the predictions of the continuum model with experimental data obtained from micropillar compression.

2.3.2 Variational formalism [B, G, H]

In this and the subsequent subsections the 2D dislocation system introduced in Sec. 2.2.1 is considered. Since the number of dislocations is conserved, the evolution of the system on the level of the densities of dislocations with different sign (ρ_+ and ρ_-) is described by balance equations that ensure conservation of the total number of dislocations of both type:

$$\partial_t \rho_\pm + \partial_x[\rho_\pm v_\pm] = f(\rho_+, \rho_-), \tag{2.9}$$

where v_+ and v_- are the average velocities of the positive and negative dislocations in the slip plane (in our case being parallel with the x axis). By adding and subtracting the two equations one obtains

$$\partial_t \rho + \partial_x[\rho v^{\mathrm{d}} + \kappa v^{\mathrm{m}}] = 0, \tag{2.10}$$

$$\partial_t \kappa + \partial_x[\rho v^{\mathrm{m}} + \kappa v^{\mathrm{d}}] = 0, \tag{2.11}$$

and the plastic strain rate according to Orowan's law reads as

$$\dot{\gamma} = b(\rho v^{\mathrm{m}} + \kappa v^{\mathrm{d}}), \tag{2.12}$$

where $\rho = \rho_+ + \rho_-$ is the statistically stored dislocation (SSD) density, $\kappa = \rho_+ - \rho_-$ is the geometrically necessary dislocation (GND) density, and $v^{\mathrm{m}} = (v_+ - v_-)/2$ and $v^{\mathrm{d}} = (v_+ + v_-)/2$ are the 'mean' and 'difference' or 'drift' velocities, respectively.

Equations (2.10,2.11) together with (2.12) represent the kinematics of straight parallel edge dislocations. When constructing dynamic equations the question is how velocities v^{m} and v^{d} depend on the microstructure represented by the densities ρ and κ. Previously Groma *et al.* performed the systematic coarse graining of the equation of motion of individual dislocations

to derive dynamic evolution equations for ρ and κ [94, 95, 98]. In this theory the velocities v^{m} and v^{d} can be expressed as

$$v^{\mathrm{m}} = Mb\chi(\tau^*), \tag{2.13}$$

$$v^{\mathrm{d}} = Mb\left(\frac{\kappa}{\rho}[\tau^* - \chi(\tau^*)] + \tau^{\mathrm{d}}\right), \tag{2.14}$$

where a non-trivial mobility function χ was introduced as

$$\chi(\tau^*) = \begin{cases} 0, & \text{if } |\tau^*| \leqq \tau^{\mathrm{y}}, \\ \tau^* - s\tau^{\mathrm{y}}, & \text{if } |\tau^*| > \tau^{\mathrm{y}}. \end{cases} \tag{2.15}$$

Here stress terms were introduced that can be calculated from ρ and κ and their spatial derivatives [H]. The term τ^* is the sum of the 'mean-field' stress τ^{mf} and the "back-stress" τ^{b}:

$$\tau^* = \tau^{\mathrm{mf}} + \tau^{\mathrm{b}}. \tag{2.16}$$

The mean-field stress is the resolved shear stress in the glide plane due to the long-range stresses of the GNDs and the surface tractions and displacements. The back-stress τ^{b} and the 'diffusion stress' τ^{d} read as

$$\tau^{\mathrm{b}} = -Gb\frac{D}{\rho}\partial_x\kappa, \tag{2.17}$$

$$\tau^{\mathrm{d}} = -GbA\,\partial_x\rho, \tag{2.18}$$

where $G = \frac{\mu}{2\pi(1-\nu)}$ is an elastic constant (μ and ν are the shear modulus and Poisson's ratio, respectively), D and A are dimensionless constants, and $\tau^{\mathrm{y}} = \alpha\mu b\sqrt{\rho}$ is the local yield stress with α being the dimensionless Taylor coefficient in accordance with the Taylor hardening law.

Equations (2.13,2.14) together with Eqs. (2.10,2.11) form a closed set of evolution equations that were found to provide analogous results as lower-scale DDD simulations [98]. These evolution equations were obtained by a systematic coarse graining of the discrete microstructure. The same equations, however, can be also derived using general thermodynamics principles. In the following this procedure and its main conceptual steps will be reviewed, since this methodology can be more easily generalized to the 3D case. Note, that the term thermodynamic refers to the general conceptual framework being adopted from irreversible thermodynamics, but does not by any means refer to the role of temperature.

We start by noticing that due to the dissipative nature of the motion of dislocations (force action on a dislocation is proportional to the dislocation velocity) the total elastic energy of the dislocation system cannot increase during the evolution of the system. Accordingly, there exists

a scalar quantity (state variable) for the discrete dislocation system that cannot increase as the system evolves.

For this governing functional the term 'plastic potential' and notation P were introduced in [B] and the main idea was found to be applicable to determine the stress field of dislocations under different conditions, such as in an anharmonic medium or in the presence of solute atoms [B]. For the evolution of the 2D discrete dislocation system the potential reads as:

$$P[\rho,\kappa] = P_{\mathrm{mf}} + P_{\mathrm{corr}}[\rho,\kappa] = P_{\mathrm{mf}} + \int Gb^2 \left[A\rho \ln\left(\frac{\rho}{\rho_0}\right) + \frac{D}{2}\frac{\kappa^2}{\rho} \right] \mathrm{d}x\mathrm{d}y. \tag{2.19}$$

Here P_{mf} is the mean-field elastic energy of the system whereas P_{corr} is a correction due to short-range spatial correlations present in the dislocation positions.

Following a standard phase-field formalism to derive the evolution equations, first one needs to compute the chemical potentials as

$$\mu_\rho = \frac{\delta P}{\delta \rho}, \tag{2.20}$$

$$\mu_\kappa = \frac{\delta P}{\delta \kappa}, \tag{2.21}$$

then the stress terms of Eqs. (2.16, 2.18) follow as

$$\tau^* = -\frac{1}{b}\partial_x \mu_\kappa, \tag{2.22}$$

$$\tau^{\mathrm{d}} = -\frac{1}{b}\partial_x \mu_\rho. \tag{2.23}$$

It was shown that the mobility law of Eqs. (2.13, 2.14) and the corresponding evolution equations do satisfy the condition $\dot{P} \leqq 0$ regardless of the actual form of the plastic potential P [G].

This observation opens new perspectives in modelling dislocation systems, since in this formalism the plastic potential P solely determines the dynamics. The form of Eq. (2.19) can be, in fact, considered as a first order correction to P_{mf} in ρ and κ that satisfies the simplest symmetry requirements. For further extension of the theory to more complex situations one does not need to repeat the microscopic derivation (which in many cases turned out to be mathematically impossible), one can extend the plastic potential P based on physical arguments. Extension of the theory to 3D was performed along these lines (see Sec. 2.3.4). A similar method was followed to account for the distribution of GND dislocations next to an impenetrable boundary [H]. This study was motivated by the fact, that structural materials do contain such boundaries to increase hardness, these include grain boundaries, phase boundaries, etc.

Let us consider a channel with surfaces perpendicular to the dislocation glide direction embedded into an infinite medium with the same elastic constants. This setup mimics a grain with boundaries impenetrable by dislocations. After randomly placing dislocations with the same

Burgers vectors into the channel [Fig. 2.14(a)] and allowing the system to relax, a DDD simulation shows that the system does not remain homogeneous and boundary layers develop at the surfaces [Fig. 2.14(b)]. It is mentioned that due to the anisotropy of the dislocation-dislocation interaction, walls are naturally formed with an average distance proportional to the dislocation spacing. The dislocation density obtained by averaging 5000 different realizations is plotted in Fig. 2.14(c).

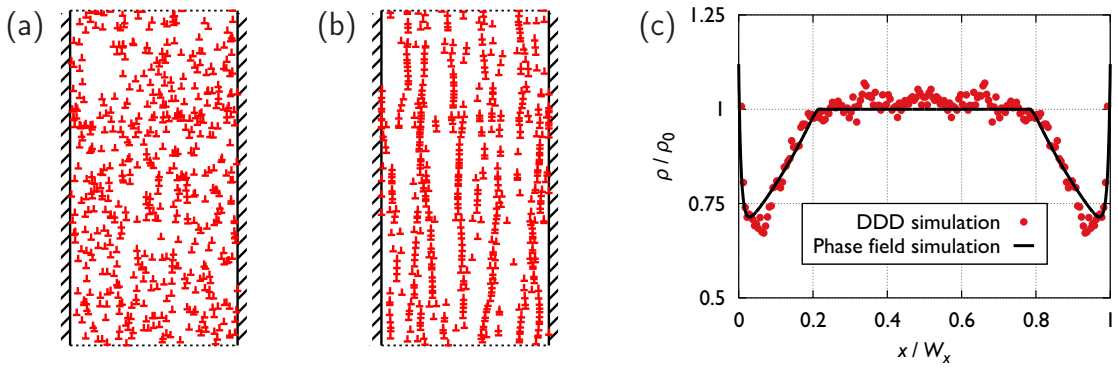

Figure 2.14: (a): Random initial configuration of dislocations with the same sign in a channel. The boundaries in the x direction are impenetrable, and periodic boundary condition is used in the y direction. The total number of dislocations is 512. (b): Relaxed dislocation configuration. (c): Dislocation density profiles (relative to the initial density ρ_0), averaged in the direction perpendicular to the slip direction, developing between two impenetrable walls obtained by DDD simulation (circles) and the numerical solution of the phase field model proposed (full line) [G].

The continuum theory outlined above cannot account for the features of the boundary layer, as it was developed for the $|\kappa| \ll \rho$, that is, small GND density case. In the case of same sign dislocations this condition clearly does not hold. One needs to extend the plastic potential of Eq. (2.19). In this spirit, a term proportional with the square of the gradient of the dislocation density was added to P as well as a surface energy term that was necessary to solve unambiguously the resulting fourth-order differential equation. Both of these terms contained a single dimensionless parameter only, since their actual form was dictated by dimensional and symmetry considerations. The density profile of the relaxed case yielded by the phase field simulations matched quantitatively the DDD results [Fig. 2.14(c)] which proves that the addition of higher order terms is necessary to account for boundary effects in the continuum model [G].

2.3.3 Pattern formation [H, M, O]

Shortly after the first images of dislocations were seen in TEM it was realized that the dislocation distribution in a deformed crystalline material is practically never homogeneous. Depending on the slip geometry, the mode of loading and the temperature, rather different pattern morphologies (e.g., cell [106], labyrinth [107], vein [108] or wall [109] structures) emerge.

There are, however, two important features common to all these patterns: It is almost always observed that the characteristic wavelength Λ of the patterns is proportional to the dislocation spacing, $\Lambda \propto 1/\sqrt{\rho}$ where ρ is the total dislocation density, and inversely proportional to the stress at which the patterns have formed. These relationships are commonly referred to as 'law of similitude' (for a general overview see [110]).

As mentioned in the Introduction of this section, several phenomenological models were proposed to address pattern formation. Since all of them contain length parameters as inputs (that are characteristic to the evolving pattern) they obviously fail to satisfy the law of similitude. On the other hand, the continuum theory summarized in Sec. 2.3.2 does not contain any unphysical length parameters and, as such, it meets the criterion of similitude. The crucial question then follows: whether the continuum theory predicts the formation of patterns and if so, whether it coincides with the patterns forming in lower-scale DDD models. This subsection is concerned with this issue.

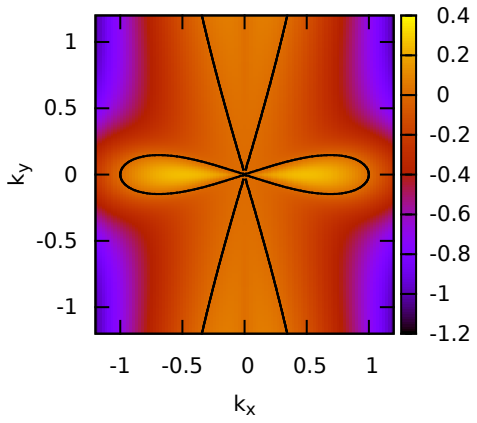

Figure 2.15: The function $\lambda(\boldsymbol{k})$ at $A = 1$, $D = 1$ and $\beta = -1$. The function is positive within the region marked by the contour line $\lambda_+(\boldsymbol{k}) = 0$ [H].

Firstly, the linear stability analysis of the continuum evolution Eqs. (2.10,2.11) were performed. One can easily see that the trivial homogeneous solution $\rho = \rho_0$, $\kappa = 0$ and $\tau_{\mathrm{mf}} = \tau_0$ satisfies the evolution equations, where ρ_0 and τ_0 are constants representing the initial dislocation density and the external shear stress, respectively. Nontrivial behaviour can happen only in

the flowing regime, i.e., if $|\tau_0| > \alpha\mu b\sqrt{\rho_0}$, so, only this case is considered. By adding small perturbations to the dislocation densities and the Airy stress function χ in the form

$$\begin{aligned} \rho(\boldsymbol{r},t) &= \rho + \delta\rho(\boldsymbol{r},t) \\ \kappa(\boldsymbol{r},t) &= \delta\kappa(\boldsymbol{r},t) \\ \chi(\boldsymbol{r},t) &= \tau_0 xy + \delta\chi(\boldsymbol{r},t) \end{aligned} \tag{2.24}$$

and after substituting these into the evolution equations and keeping only the leading terms in the perturbations one arrives at [H]

$$\begin{pmatrix} \delta\rho \\ \delta\kappa \\ \delta\chi \end{pmatrix} = \begin{pmatrix} \delta\rho_0 \\ \delta\kappa_0 \\ \delta\chi_0 \end{pmatrix} \exp\left(\frac{\lambda}{t_0}t + i\sqrt{\rho_0}\boldsymbol{k}\boldsymbol{r}\right), \tag{2.25}$$

where the sign of λ determines whether the perturbation characterized by the wave vector $\boldsymbol{k}$ grows with time. The mathematical analysis yields a $\lambda(\boldsymbol{k})$ function plotted in Fig. 2.15. Remarkably, an unstable region with $\lambda > 0$ appears with a certain maximum along the x axis. This means that lengthscale selection takes place, i.e., the fluctuation that grows fastest exhibits a well-defined wavelength. In Fig. 2.15 a particular set of parameters A, D and β (the first two of which are dimensionless parameters of the gradient stress terms, and the latter is related to the strain rate) were used, but the result is general, for the corresponding discussion see [H].

As said above the linear stability analysis can only provide information on the instability of the trivial solution, but it cannot predict how the initially unstable mode will evolve at later stages. For that the solution of the dynamic evolution equations is necessary. To this end, two different solutions of the equations were implemented where transport of dislocations that controls dislocation density evolution is described in two very different manners. Namely, (i) a hydrodynamic formulation is considered where transport equations are continuous in space and time, assuming that the dislocation velocity depends linearly on the local driving stress, and (ii) a stochastic cellular automaton implementation is developed that assumes spatially and temporally discrete transport of discrete 'packets' of dislocation density that move according to an extremal dynamics [M]. The latter is in fact a more detailed version of the SCPM described in Sec. 2.2.4 that also accounts for the development of local dislocation densities.

Figure 2.16 plots the evolution of the pattern when a Gaussian white noise as initial perturbation is used. First, embryonic patterns start growing locally and then, in a first 'synchronization' stage, organize in the y direction to form parallel walls. In a second 'growth' stage the amplitude of these wall-like dislocation density modulations increases while the once-established pattern remains in place. If, on the other hand, simulations start from a localized dislocation density 'blob' then an interesting scenario occurs: The blob causes positive and negative dislocations

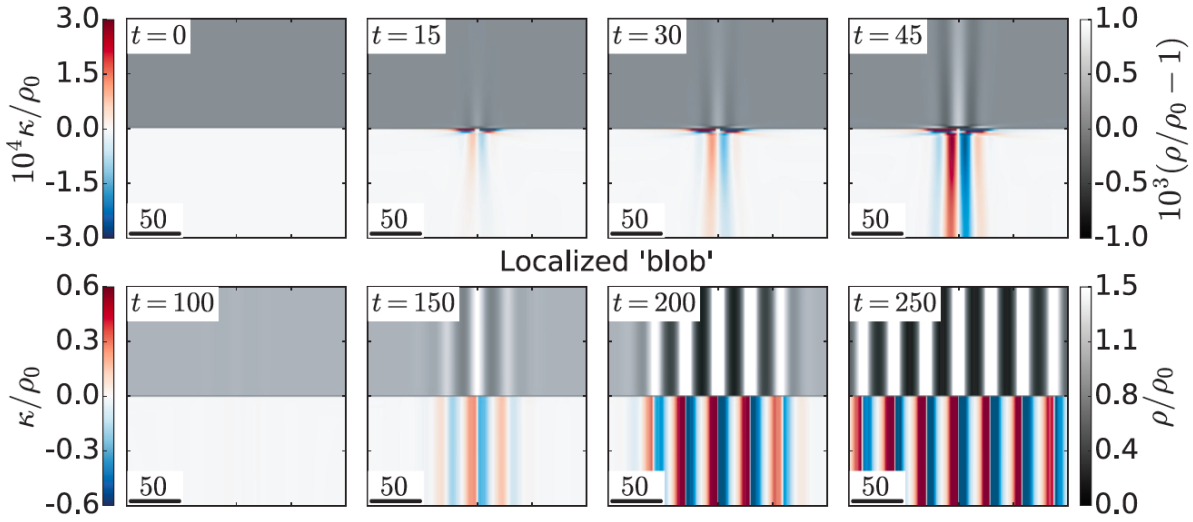

Figure 2.16: Spatiotemporal evolution of dislocation density patterns [total density $\rho(\boldsymbol{r},t)$ and GND density $\kappa(\boldsymbol{r},t)$] in two dimensions for small Gaussian white noise superimposed on a homogeneous density distribution as initial condition; for parameters see [M].

to pile up from both sides. The long-range stresses of the double pile-up then lead to growth of a double wall similar to a kink band in the y direction. Finally, the double wall serves as the nucleus for a nonlinear wave which spreads the pattern in the y direction [M]. Despite the differences, we find that the emergent patterns in both scenarios and both models are mutually consistent and in agreement with the prediction of the linear stability analysis of the continuum model mentioned earlier.

However, in lower-scale 2D DDD simulations such periodic patterns have not been seen so far. Since the continuum model described above was obtained by coarse graining the discrete equations, this issue needed to be addressed. In Sec. 2.2.4 the distribution of the yield thresholds were found to follow a weakest link distribution and, accordingly, the local local yield stresses were Weibull-distributed with a shape parameter $\beta \approx 1.4$. In the continuum and SCPM models above, however, the yield stresses were either deterministic (continuum case) or were drawn from a sharp distribution with a relatively small standard deviation. In order to understand the role of the stochastic yield stress in the pattern formation the yield thresholds in the SCPM were configured with the Weibull distribution obtained directly from the DDD simulations. The emergent pattern evolution is shown in Fig. 2.17. As seen, the formation of dipolar dislocation walls is apparent in both discrete and continuum versions, but these walls are not periodic in the x direction [O]. The analogy between discrete and continuum cases was also proven in terms of the spatial correlation functions. Our results, thus, shed new light on the role of the back stress as well as the stochastic local yield threshold in dislocation patterning of bulk single crystals and provide a successful multiscale description of the dynamics in single-slip edge dislocation systems [O].

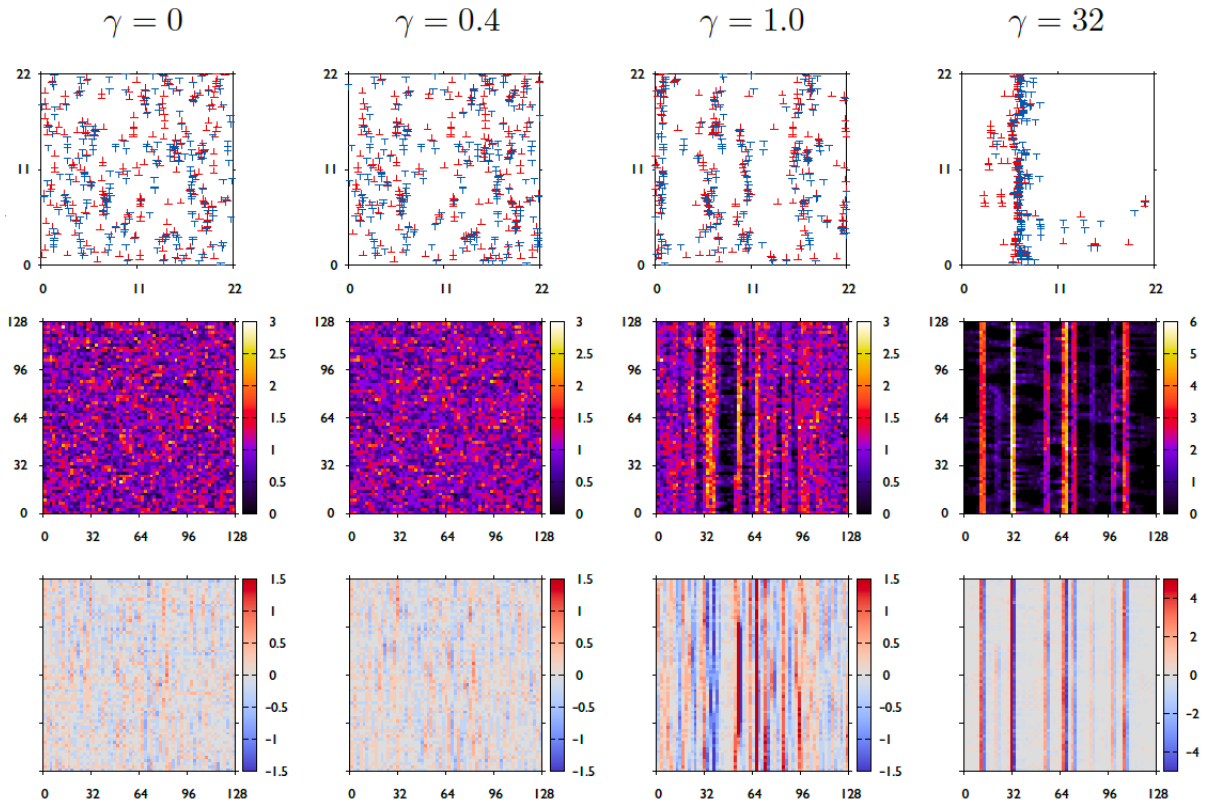

Figure 2.17: Dislocation pattern evolution in discrete and stochastic continuum simulations. Top row: Dislocation configurations obtained with DDD at different plastic strain values γ. Middle and bottom rows: Density of total and GND densities (ρ and κ, respectively) obtained by SCPM simulations at different plastic strain values γ [O].

2.3.4 Modelling in 3D [T, U]

The continuum theory detailed above was developed for parallel straight edge dislocations, a system that is essentially 2D. Real dislocation structures, however, consist of curved dislocations on various slip planes giving rise to a much more complex dynamics. It was, therefore, a long-standing issue if a similar procedure as for 2D (rigorous coarse graining or a phase field approach) can be established for curved dislocation systems. As a first step towards a physics-based 3D theory we carried out the generalization of the phase field formalism for curved dislocations for a single-active-slip system. To this end, the kinematic framework developed by Hochrainer and co-workers was adopted [100–104]. In order to be able to treat dislocations of different orientation in the same volume element, the problem was extended into $2+1$ dimensions, where the dislocation line direction is introduced as an independent variable at each point. In the glide plane, the line direction was represented by the angle φ that the local dislocation line direction forms with the x axis, given by, e.g., the Burgers vector. So, the problem was

'expanded' to the $(x, y, \varphi) = (\boldsymbol{r}, \varphi)$ space. To further reduce the complexity a first order Fourier expansion was applied for the total density, dislocation velocity and curvature density as

$$\rho'(\boldsymbol{r},\varphi) \approx \rho(\boldsymbol{r}) + 2\cos\varphi\kappa_1(\boldsymbol{r}) + 2\sin\varphi\kappa_2(\boldsymbol{r}), \tag{2.26}$$

$$v'(\boldsymbol{r},\varphi) \approx v^{\mathrm{m}}(\boldsymbol{r}) + \cos\varphi v_1^{\mathrm{d}}(\boldsymbol{r}) + \sin\varphi v_2^{\mathrm{d}}(\boldsymbol{r}), \tag{2.27}$$

$$q'(\boldsymbol{r},\varphi) \approx q(\boldsymbol{r}) + \cos\varphi Q_2(\boldsymbol{r}) - \sin\varphi Q_1(\boldsymbol{r}). \tag{2.28}$$

respectively [U]. With this approximation the kinematic theory took an analogous form to 2D Eqs. (2.10, 2.11), but now with two GND density components κ_1 and κ_2 (edge and screw components, respectively), two corresponding drift velocity components v_1^{d} and v_2^{d} and quantities related to curvature q, Q_1 and Q_2. This analogy made it possible to generalize the phase-field formalism of the 2D case with specific mobility functions that guarantee the decrease of the plastic potential during evolution, i.e., $\dot{P} \leq 0$. As such, the dynamics in the theory is dictated solely by the scalar functional P, the exact form of which can be determined by generalising the 2D theory and using symmetry and other physical arguments [U].

Apart from curvature, another important aspect of the full 3D theory is to account for several slip systems. Formally, it appears relatively straightforward to generalize the theory for multiple slip. In this case, however, local dislocation-dislocation interactions, like formation of junctions and dislocation annihilation, cannot be neglected. Moreover, cross slip and at higher temperature climb may play an important role, too. These phenomena need to be incorporated into the proposed theory as source and sink terms. Promising ways how to incorporate some of these phenomena in continuum dislocation theories were recently proposed by El-Azab *et al.* [90, 91, 111] and Schulz *et al.* [112, 113]. These extensions proved successful in describing various technologically important situations, such as torsion of microwires [114].

The mentioned reaction terms contain fitting parameters that are usually fitted with the help of 3D DDD simulations that are computationally limited to rather small volumes and achievable strains. It is, therefore, necessary to test the continuum dislocation dynamics (CDD) model predictions against experimental evidence. Such a unique opportunity is provided by micropillar compression experiments, where using complementary high-resolution electron backscatter diffraction (HR-EBSD) the internal dislocation microstructure can be directly characterized in terms of some of the components of the Nye dislocation density tensor, as seen in Fig. 2.18 (for details see Sec. 2.4.3). We, therefore, investigated the dislocation microstructure evolution in FCC metallic microsamples. Single crystalline copper micropillars with a $\langle 1\,1\,0 \rangle$ crystal orientation (multiple-slip to favour dislocation reactions during deformation) and varying sizes between 1 to 10 μm were analysed under compression loading. The analysis was paralleled by 3D CDD simulations that consider dislocation dynamics, interactions, and reactions of the individual slip systems and providing direct access to these quantities (see Fig. 2.18).

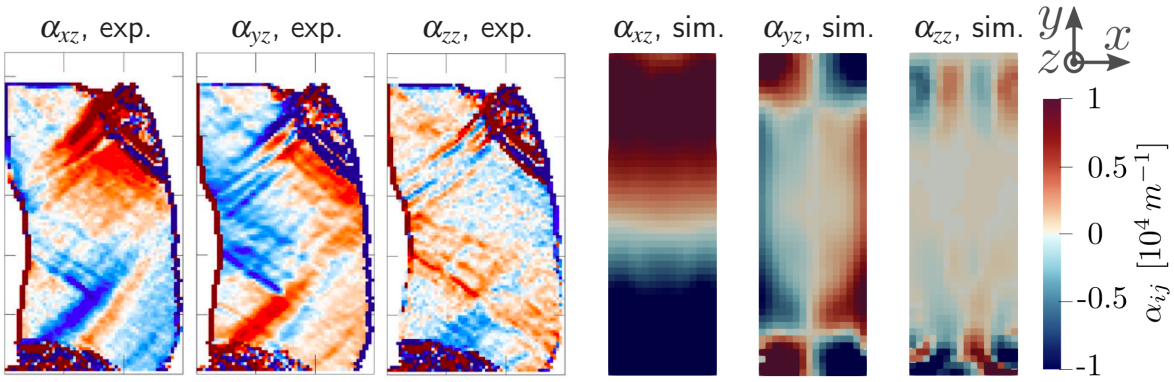

Figure 2.18: First 3 panels: The experimentally accessible components of the tensor $\boldsymbol{\alpha}$ of the 10 μm pillar deformed *in situ* at 9.3 % strain. Second 3 panels: The corresponding components obtained by CDD simulations. Note that in the cross-section of the pillars are in all cases $a = 10$ μm, however the aspect ratios are different. In addition, values in the experimental figures are 10 times larger than that shown by the scale [T].

It was shown, that the plastic deformation of the material is mainly caused by dislocation activities on the four slip systems with the highest Schmid factor. Here, the loss of dislocation density over the surface leads to observable deformation patterns and surface steps. An interesting finding is the increasing amount of GND density in the system during loading. It has been observed for all micropillars considered and is located dominantly on the slip systems that are not mainly responsible for the production of plastic slip. The stabilization of the GND density on these inactive slip systems can be explained by the lower Schmid factor and the associated lower driving force on the dislocations on these systems. However, the presented results indicate that the obstruction for dislocation motion caused by dislocation network formation may play a significant role for this finding.

In the considered size regime, the dislocation network formation is emphasized with increasing micropillar size for small loading states. This indicates a transition from a dislocation starvation regime to a regime dominated by dislocation accumulation forming a cellular structure. This is accompanied by longer travel distance of dislocations to the surface as well as the lower dislocation velocities that can be observed for larger micropillars enforcing the probability of network formation and yielding a contribution to plastic hardening [T].

2.4 Experimental investigations

2.4.1 Introduction

As it was mentioned in the Introduction of the thesis, most of the research presented here was motivated be the pioneering micropillar compression experiments of Dimiduk and co-workers

[19–21]. This influential series of papers layed down the foundations of a new sub-field of materials science that can be termed *micro-* and *nanomechanics*. Our research group at the Department of Materials Physics decided to construct a microdeformation stage that can be placed inside an SEM chamber in order to perform such *in situ* deformation experiments. The reasons for this decision are as follows:

- A new dual-beam SEM device was installed in 2010 at the host institution that made microsample fabrication possible and had a relatively large vacuum chamber that could host the microdeformation stage.
- The required know-how was available at the Department, since micro- and nanoindentation experiments had for long been carried out.
- At the time (around 2015) the commercially available devices did not meet our expectations: they utilized stress control, had a quite low data acquisition rate and were not flexible in the sense that they were capable of performing only one type of experiments.
- Last but not least, developing a new device is financially much more advantageous than buying a new one.

The device constructed is capable of performing compression tests at room temperature in high vacuum mode inside the SEM chamber to allow *in situ* monitoring of the deformation process and slip activity on the samples' surface by secondary and backscattered electrons. The deformation stage sketched in Fig. 2.19 is equipped with an *xy* stage that allows the user to position the micropillar precisely under the indentor tip and a piezoelectric fine z stage that performs the compression. The fine z stage in fact moves a spring that is connected to the flat punch tip and its elongation is measured using a capacitive displacement sensor in order to obtain the acting force. Since the range of the fine z stage is small (30 μm) a conventional coarse z stage was also installed that is only used to navigate the tip to the vicinity of the sample. The device is constructed without any load or strain feedback loop integrated and during measurements the fine z stage (called platen) is moved with a constant velocity. The precision of the measured indentation depth and load is $\sim$1 nm and $\sim$1 μN, respectively. The sampling rate is 200 Hz, while the spring constant can be set to either 1 mN/μm or 10 mN/μm. For a detailed description of the device, the reader is referred to [K].

The first part of this section will be concerned with deformation phenomena of micropillars based on stress-strain curves and the SEM images recorded during and after deformation. In particular, the statistical fluctuations characteristic of this scale will be analysed followed by investigating twinning in Mg micropillars. In Sec. 2.4.3 we utilize a novel experimental methodology of HR-EBSD that is able to characterize the dislocation structure from electron diffraction measurements. This method will be used to evaluate dislocation structures found in

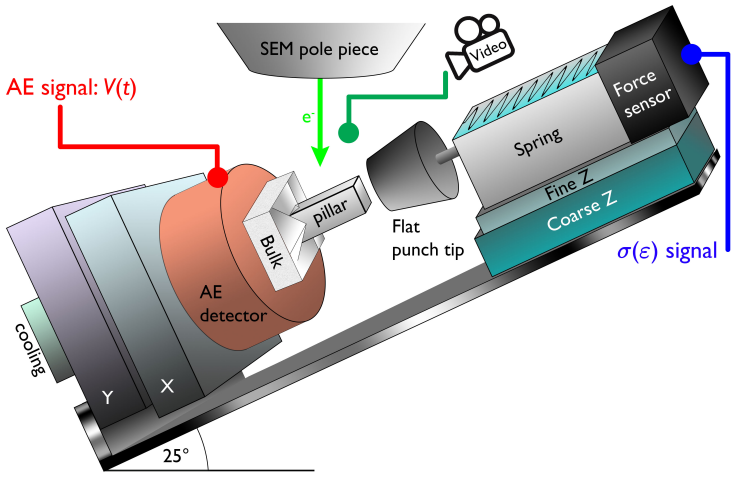

Figure 2.19: Sketch of the microdeformation stage with an unproportionally large micropillar for clarity.

bulk and microscopic single crystalline Cu samples as well as in W around a crack tip. Finally, Sec. 2.4.4 concludes the thesis with summarizing recent results obtained by coupling micropillar compression experiments with the detection of acoustic emission (AE).

2.4.2 Deformation properties of micropillars [D, V]

As it was mentioned already in Sec. 2.2.2, due to the large strain fluctuations emerging at small scales the stress–strain curves of micron- and submicron-scale specimens are of random character in several aspects. The step-like curves consist of plateaux corresponding to strain bursts, and stress increments connecting these plateaux. Consequently, the yield stress of the micropillars can only be defined in a probabilistic way over an ensemble of specimens with the same parameters (size, dislocation density, etc.) as it was also concluded earlier using 2D and 3D DDD simulations [A]. To test the numerical findings experimentally, compression tests were carried out on a large number of pure Cu single-crystalline micropillars with a diameter of $d = 3\,\mu$m. These pillars exhibited the same crystallographic orientation and a close-to-identical geometry so they in principle only differed in the inherent initial realization of the dislocation structure [see Fig. 2.20(a)].

Since the *in situ* deformation stage described in Sec. 2.4.1 had not yet been ready, the uniaxial compression tests were carried out ex situ with a UMIS II. Csiro nanoindenter using a flat-punch diamond tip. The pillars were large enough to enable the indenter to be properly positioned using an optical microscope. The compression tests were performed under load control with a rate of 0.01 mN/s. For exemplary stress-strain curves see Fig. 2.20(b), and for additional details of the experiments, see [D].

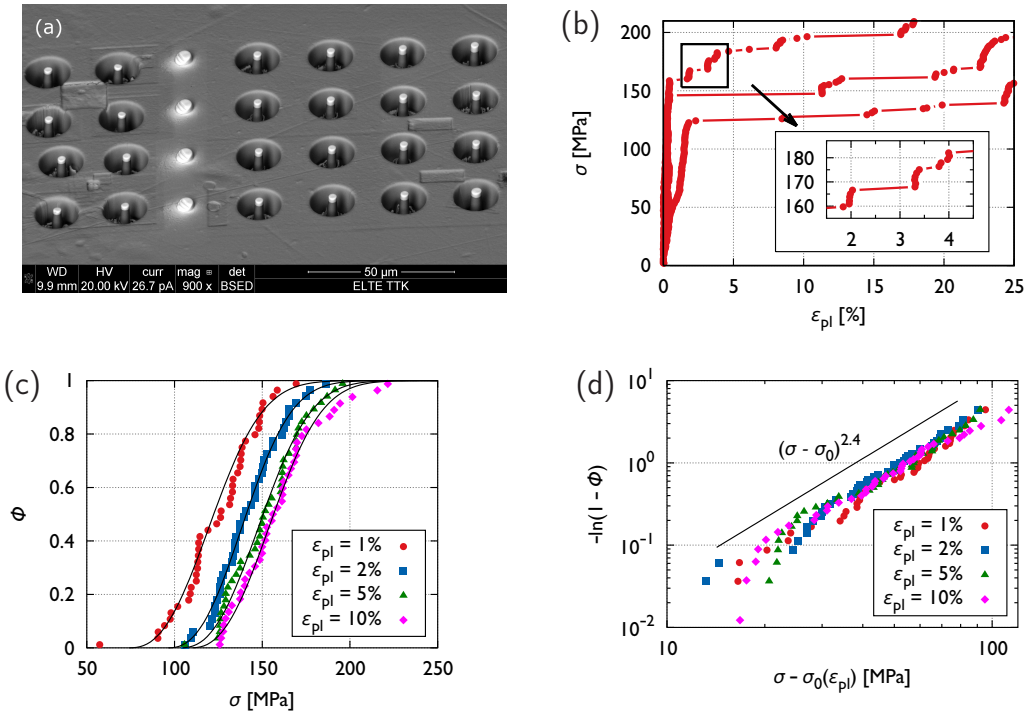

Figure 2.20: (a): SEM backscattered electron images of 24 micropillars before compression. This type of imaging leads to different contrast for different elements, making the amorphous Pt cap clearly visible. (b): Exemplary nominal stress (σ)–plastic strain ($\varepsilon_{\mathrm{pl}}$) curves measured for three different cylindrical micropillars. (c): Cumulative distribution function of the measured applied stress values. The different curves correspond to various plastic strain levels $\varepsilon_{\mathrm{pl}}$ where the stress levels were measured. The solid lines are fitted Weibull distributions. (d): The same distribution on a Weibull plot [D].

According to the statistical analysis of the ensemble of stress-strain curves a threshold stress level σ_{th} could be defined. This point exhibits features that are characteristic of yielding. First, there is a microplastic regime below σ_{th} where there is some plastic strain accumulating, but plastic strain starts to increase rapidly only above this threshold stress σ_{th}. This microplastic regime is characterized by a power-law as $\varepsilon_{\mathrm{pl}} \propto \sigma^{\beta}$, with $\beta \approx 1.1-1.2$. Second, the variance of the plastic strain also increases faster above σ_{th}, suggesting that the system enters a statistically different regime above σ_{th}.

The cumulative distribution functions $\Phi_{\varepsilon,\mathrm{pl}}$ of the stress values measured at different plastic strains $\varepsilon_{\mathrm{pl}}$ are seen in Fig. 2.20(c). The data can be fitted well by a general Weibull distribution:

$$\Phi_{\varepsilon_{\mathrm{pl}}}(\sigma) = \begin{cases} 1-\exp\left(-\dfrac{[\sigma-\sigma_0(\varepsilon_{\mathrm{pl}})]^k}{\delta\sigma(\varepsilon_{\mathrm{pl}})^k}\right), & \text{if } \sigma > \sigma_0(\varepsilon_{\mathrm{pl}}), \\ 0, & \text{otherwise.} \end{cases} \tag{2.29}$$

Here k is the Weibull exponent, and σ_0 and $\delta\sigma$ set the minimum stress and the scale (σ_0 is the lower bound of the support of the distribution function). Parameters σ_0 and $\delta\sigma$ depend on

ε_{pl}, but $k = 3.5$ was taken identical for all the curves. The fit is not only satisfactory on the linear scales but, as seen in Fig. 2.20(d), the Weibull plot of the data also yields a straight line, showing that the asymptotic properties of the distributions are identical.

So, we could conclude that the stress values corresponding to a given plastic strain followed weakest-link statistics of Weibull type. This suggested that plasticity of micron- or submicron-scale pillars was influenced by a weakest-element mechanism and that a dislocation system can be envisaged approximately as a set of independent subregions of the system, and the global yield stress corresponds to that of the weakest element. This conjecture served as the main motivation for the theoretical investigations presented in Sec. 2.2.4. It is noted, that identical conclusions were drawn based on 2D and 3D DDD simulations [D].

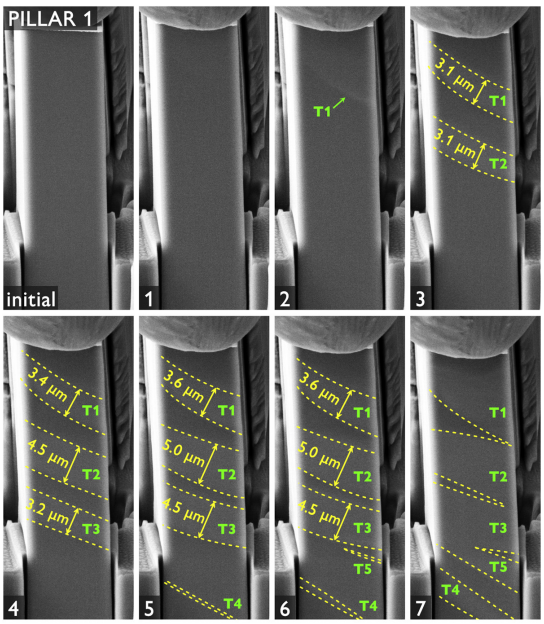

Figure 2.21: The twin evolution and growth dynamics in one of the tested micropillars during compression [V]. For the corresponding video see `https://youtu.be/Q5YwLzyvnao`

In a subsequent, more recent study, the formation and propagation of twins was studied in microsamples having HCP lattice structure in collaboration with colleagues at Charles University, Prague. In particular, single-crystalline rectangular Mg micropillars (dimensions of $10 \times 10 \times 30\,\mu\text{m}^3$) having the orientation that favored twinning were fabricated. The pillars were tested in compression using the high-precision nano-testing device introduced above with concurrent scanning electron microscopy imaging. All the experiments were performed at our Micromechanical Laboratory at the Eötvös Loránd University. The course of a typical experiment is shown in Fig. 2.21. As seen, the twinned regions exhibited different contrast making them easy to recognize in the SEM figures. Deformation proceeded intermittently as twinned regions appeared abruptly accompanied by a stress drop. These nucleated twinned regions then

started to grow, but after reaching a certain critical width their growth stopped and the nucleation of new twins took place. This process was repeated until the twins formed across the entire micropillar height, from its top to its base. Finally, the thickening and coalescence of all the twins took place until the whole volume of the micropillar was twinned. The experimental data were supplemented by finite element method (FEM) calculations. It was shown experimentally and also supported by FEM calculations that the critical thickness was around 3 μm for the studied micropillars. These observations can be effectively explained in terms of the FEM data, especially by means of the shear stress intensity and distribution. Using a line-by-line analysis of the SEM images together with a detailed examination of the compression curves (stress drops) allowed us also to effectively monitor twinning dynamics and to estimate the twin lateral growth rate in Mg micropillars that was found to be in the order of $10^{-5} - 10^{-4}$ m/s. These findings related to twinning at the micrometer scale will be relevant in the development of modern micro−/nano-electromechanical devices (MEMS/ NEMS), since at small scales, as already stated many times before, the deformation behavior becomes less predictable, and this proved to be true for twinning as well.

2.4.3 Assessing internal dislocation structure with HR-EBSD [L, N, R]

All the stochastic properties of plastic flow this thesis is concerned about are related to the fluctuations of the internal dislocation microstructure. Therefore, to measure and analyse the distribution of dislocations in the material (i.e., dislocation patterns) and its statistical properties is indispensable to understand the emergent behaviour. In this chapter the novel method of the high-resolution electron backscatter diffraction (HR-EBSD) is utilized.

The main steps of the method are shown in Fig. 2.22. This technique is based on the so-called Kikuchi patterns that are formed by the diffraction of electrons that get backscattered from the crystal lattice. The patterns are recorded on a square grid. From the pattern the structure and orientation of the crystal can be determined, this procedure corresponds to the standard EBSD method. Here the individual patterns are compared to a reference pattern using a sophisticated cross-correlation analysis to obtain the shift, rotation and distortion of the Kikuchi pattern. From these information one can determine the components of the distortion and the stress tensors within the volume illuminated by the electrons [115, 116]. Based on these information HR-EBSD can characterize the distribution of GNDs in terms of three independent components of the Nye dislocation density tensor. The measurements can be performed on a grid of as small as sub- 100 nm step size, however information is only gathered from the first few tens of nanometers below the surface [117]. Consequently, the careful preparation of the sample surface is of utmost importance for HR-EBSD.

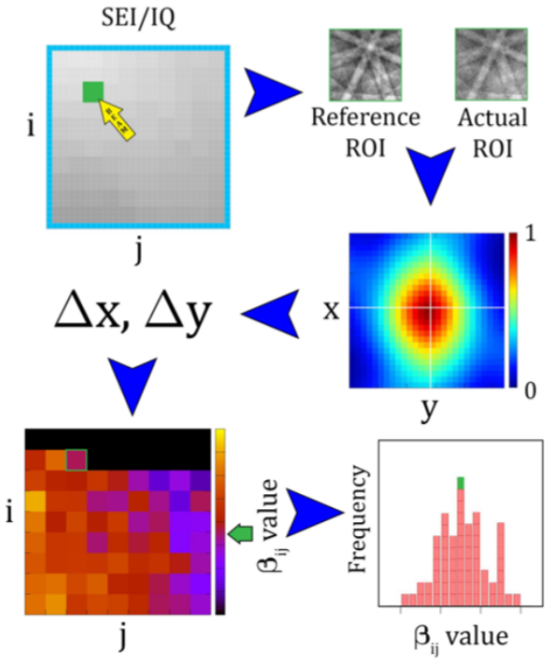

Figure 2.22: Sketch of the HR-EBSD method. The blue arrows show the flow of the process. First, diffraction patterns are recorded on a square grid, then a cross-correlation analysis yields the values β_{ij} of the distortion tensor. One can then obtain, e.g., statistical information about the sample [118].

HR-EBSD had traditionally been used to determine the GND density in the specimen. Wilkinson and co-workers, however, realized that the distribution of the stresses in a polycrystalline sample exhibits a power-law tail [119] similarly to that of the Bragg peaks obtained by XRD on a single crystal [120]. The latter is related to the fact that the distribution of internal stresses σ in a dislocated crystal decays as $1/|\sigma|^3$ with a pre-factor proportional with the total dislocation density [121]. Motivated by these results, in our first investigation with HR-EBSD statistical properties of the dislocation structure developing in an FCC single crystal were investigated [L]. In particular, Cu single crystals of rotated Goss orientation $(011)[01\bar{1}]$ were cut by electrical discharge machining into cuboid shapes and deformed by channel die compression up to the strain levels of 6% and 10%. The compression was performed parallel to the [110] plane normal, while the sample elongated along the $[1\bar{1}0]$ direction, and it was held fixed by the channel walls along the [100] direction. Before deformation, HR-EBSD and x-ray diffraction (XRD) analyses, the samples were electropolished. This type of deformation leads to multiple slip and a cellular pattern already at 6% strain as seen in Fig. 2.23(a). The average cell size was about 2-3 μm.

The question we intended to answer was whether the stress distribution in a single crystal measured by HR-EBSD decays with an inverse cubic tail and if so whether its pre-factor is proportional with the density of dislocations. To determine the latter, complementary XRD measurements were conducted. Further details of the experiments can be found in [L]. The

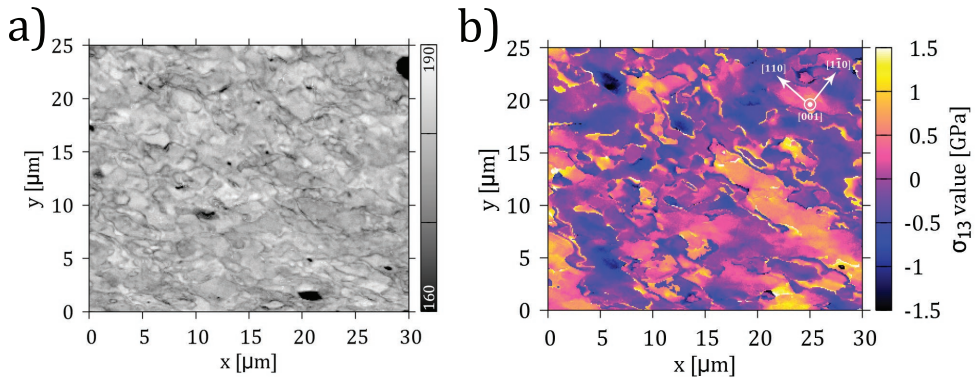

Figure 2.23: (a): Band contrast map obtained on the sample deformed up to 6% strain. (b): The σ_{13} stress component map obtained by HR-EBSD on the same sample. The stress levels indicated are relative values to the stress level at the centre of the scanned area [L].

results yielded positive answers to both of the questions. This means that the total dislocation density could be quantified from a single HR-EBSD map, and the obtained values showed good correlation with those from XRD. It was also found that the ratio of the GND and stored dislocation densities are not constant with increasing strain suggesting that there are two 'separate' length scales in the system. These findings opened new perspectives in the applicability of HR-EBSD in the statistical description of heterogeneous dislocation structures [L].

The method of HR-EBSD can also be used to characterize the spatial distribution of the dislocations within the sample from the components of the Nye dislocation density tensor. In our next paper we aimed at investigating the dislocation distribution in deformed single crystalline copper micropillars [N]. To this end, identical micropillars ($6 \times 6 \times 18$ μm^3 in size) were fabricated by FIB and compressed at room temperature. The deformation process was stopped at different strain levels ($\approx$1%, 4% and 10%) to study the evolution of the GND network. HR-EBSD is only capable of performing measurements on the surface of the sample. To allow for the reconstruction of the whole 3D structure serial slicing was applied, that is, after every HR-EBSD measurement the top $\sim$100 nm layer of the sample was removed by FIB and every time the diffraction measurement was repeated. This so-called 3D HR-EBSD measurement made it possible to create and compare 3D maps of the deformed volumes (see Fig. 2.24). An intermediate behaviour was found at the studied sample size between bulk and nanoscale plasticity: A well-developed dislocation cell structure was built up upon deformation but with significantly lower GND density than in bulk. This explained the simultaneous observation of strain hardening and size effect at this scale. To validate the HR-EBSD measurements complementary scanning transmission electron microscopy (STEM) and TEM images were captured on the 10% pillar to visualize the actual dislocation structure that verified the presence of the cell walls obtained by HR-EBSD [N].

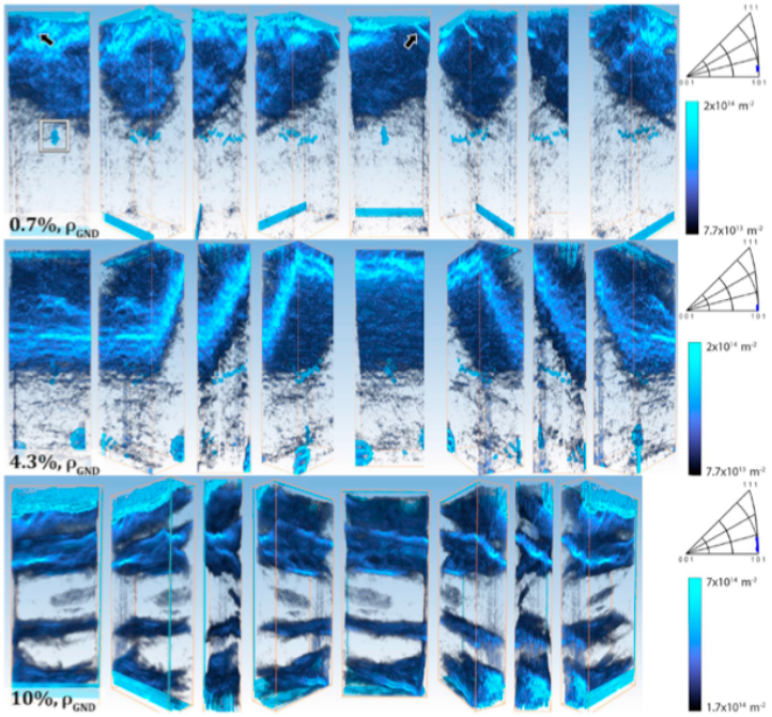

Figure 2.24: 3D models of GND density values for the three micropillars (top row: 0.7%, middle row: 4.3%, bottom row: 10%) rotated around for inspection. First view in each row was made as we look directly on the outer surface of the pillar (first slice). The flat punch tip – Pt cap interface is located at the top of each model. Black arrows in the 0.7% deformed pillar mark the FIB milling artefact. White square indicates the reference pattern replacement artefact. Absolute values of angles of the active slip systems can be easily identified. Inverse pole figures (IPFs) on the right side show the orientation distribution viewed from the compression direction, plotted for one slice from the middle of each pillar [N].

Finally, HR-EBSD was utilized to characterize the shape of the plastic zone in terms of GNDs in a W single crystal in 3 dimensions [R]. Cantilevers of similar size with a notch were fabricated by FIB and were deformed inside a scanning electron microscope at different temperatures (21 °C, 100 °C and 200 °C) just above the micro-scale brittle-to-ductile transition. This was followed by an in-depth HR-EBSD analysis of various planes. The obtained Nye tensor components are shown in Fig. 2.25. The value of $\alpha_{\mathrm{sq}} = \sqrt{\alpha_{13}^2 + \alpha_{23}^2 + \alpha_{33}^2}$ was used to estimate the total GND content. As seen, at all three temperatures the plastic zone was found to be larger close to the free surface than inside the specimen, similar to macro-scale tension tests [122]. However, at higher temperature, the 3D shape of the plastic zone changes from being localized in front of the crack tip to a butterfly-like distribution, shielding more efficiently the crack tip and inhibiting crack propagation. The analysis of the distribution of the Nye tensor components was used to differentiate between the types of GNDs nucleated in the sample. Based on the α_{i3} components, the Burgers vector directions can be identified. A sketch in the bottom row of Fig. 2.25 reflects only the collective sign of the projected Burgers vector around the crack

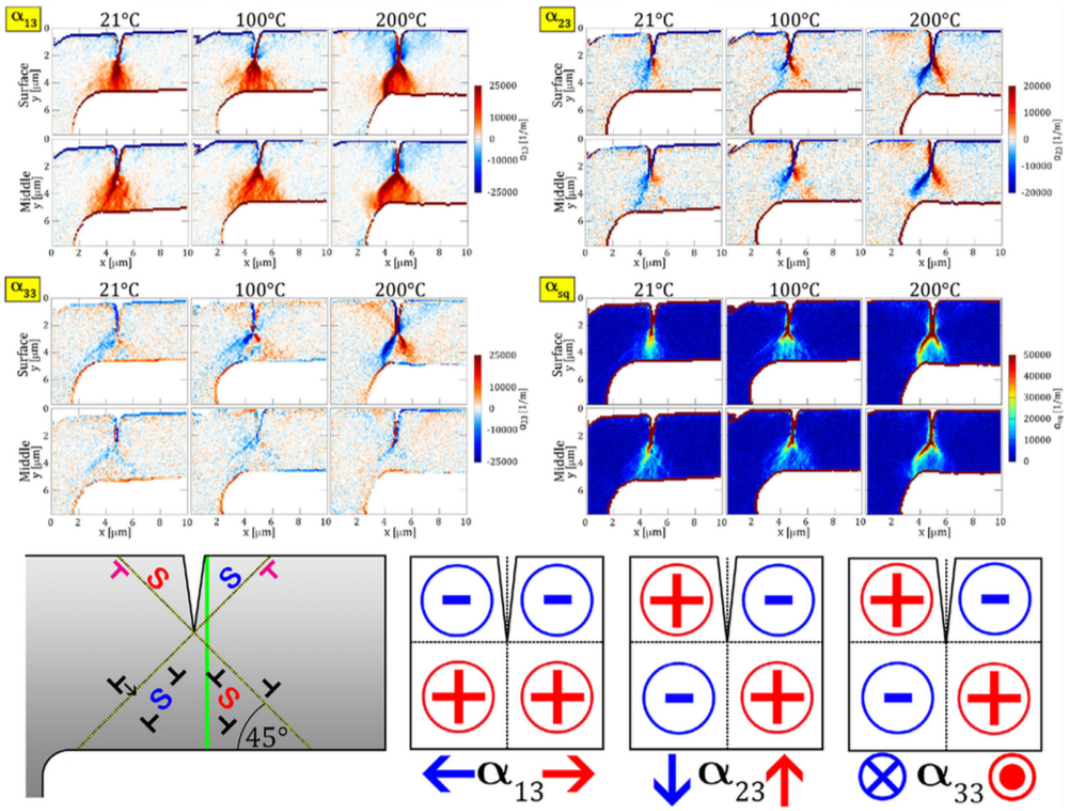

Figure 2.25: Distribution of α_{13}, α_{23}, α_{33} and α_{sq} components at three different temperatures close to the surface and in the middle of the cantilever. Bottom row represents a sketch of the GND configuration based on the α_{i3} component analysis and Burgers vector directionality. Arrows indicate the typical Burgers vector direction based on the component analysis. Dislocations coloured in magenta correspond to increased edge type GNDs at higher temperatures due to increased pile-ups in the system [R].

tip. Earlier studies had already investigated BCC systems, where dislocations emitted from a crack tip were described and crack tip deformation had been presented [123, 124] and modelled [125]. In these works the excess dislocations around the crack tip were assumed to be emitted from the crack on various slip planes. After studying the Burgers vector configuration based on the Nye-tensor components, however, we concluded that the GND configuration is not as simple as it was expected earlier. The observations of Fig. 2.25, i.e., that Burgers vectors have a direction perpendicular to the line connecting the dislocations and the crack-tip indicate that the detected GNDs are not mainly emitted from the crack tip. Rather, it was suggested that they are formed by secondary dislocation sources that are being created by increased dislocation interactions due to large local stresses, pinning, and junction formation. These results, to our knowledge, represent the first analysis based on HR-EBSD measurement that aims at studying the directionality of $\boldsymbol{b}$ and show the strong capacities in these measurements in describing and understanding dislocation structures and their evolution [R].

2.4.4 Acoustic emission [K, X]

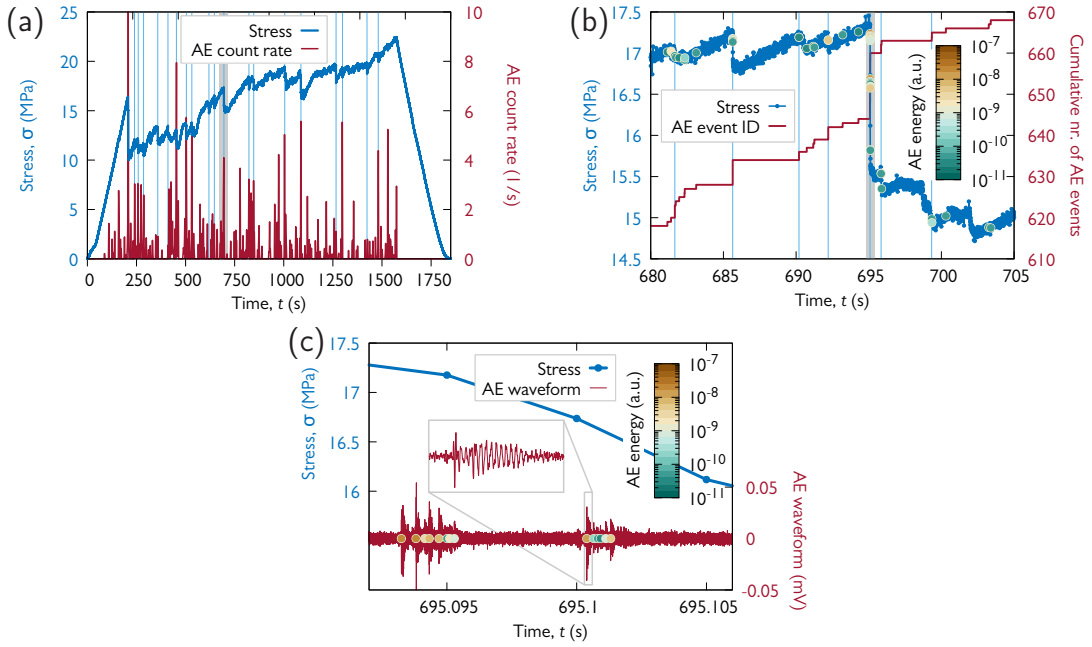

Figure 2.26: Compression experiment of Zn micropillars oriented for basal slip. (a): An exemplary measured stress vs. time curve as well as the rate of the detected individual AE bursts. The light blue vertical lines mark the stress drops larger than 1 MPa. (b): Zoomed stress-time curve of the region shaded by grey in panel (a). The coloured data points along the stress curve represent the individual AE signals and their energy and the red curve shows the cumulative number of these signals. (c): Zoomed stress-time curve of the region shaded by grey in panel (b) and the detected AE waveform of the same interval. The inset shows the magnified view of a single event and coloured data points correspond to individual signals detected by thresholding the AE signal [X].

In spite of the focused research of the community detailed above, a general framework to describe stochastic behaviour is still elusive, partly because experimental results are not robust enough (they are rather sensitive to sample geometry, strain rate, machine stiffness, etc.). Thus, development of new experimental methodologies for microdeformation may help clarifying the open issues regarding stochastic plastic response and the corresponding critical behaviour. The results related to HR-EBSD technique described in the previous section also pointed in this direction. Our research group made another step towards extending our experimental capabilities by investigating acoustic signals during microdeformation. The microdeformation stage described in Sec. 2.4.1 was designed and developed not only to be able to record stress-strain characteristics of microsamples but also to record the released acoustic emission (AE) signal at the same time *in situ* [K]. A piesoelectric AE sensor is placed under the sample, as seen in Fig. 2.19. To my knowledge, such a simultaneous measurement had not been performed before and made it possible to study strain bursts in more detail since the time resolution of AE is orders of magnitude better than that of a force sensor. Indeed, compression experiments

performed on single crystalline Zn micropillars yielded a strong correlation between the stress drops – resulting from the elongation of the indentor spring after the sudden collective dislocation rearrangement in the sample – and AE bursts (see Fig. 2.26). Through these results it was not only confirmed that the AE signals originate directly from dislocation avalanches, but also the temporal analysis of the AE signal proved that dislocation avalanches obey the ubiquitous fundamental scaling laws of earthquakes [X]. The results (currently being under review) not only shed light on the universal behaviour of collective dislocation phenomena but are also of high technological importance, since they allows one to relate to properties of AE signals to those of the microscopic deformation event. This information is crucial for the assessment of AE experiments performed on bulk samples.

3 Thesis statements

I summarize below the most important results of the scientic work presented in Chapter 2. The relevant publications are referenced at each thesis point and detailed in my publication list in Chapter 5.

1. *Plastic yielding at the micrometer scale.* I applied DDD simulations and microcompression experiments to investigate the stochastic nature of yielding of micron-scale objects. I conceived the idea of defining the yield stress at this scale over an ensemble of statistically equivalent realizations via the average stress-strain curve. The particular related findings are as follows:

   a) 2D and 3D DDD simulations were employed to show that a yield stress can be defined in an average sense that separates two statistically different regimes: a microplastic part with a limited amount of activity and a flowing part with a significant plastic strain rate due to dislocation avalanches.

   b) The same analysis was extended to an ensemble of single crystalline Cu micropillars with identical parameters (initial average dislocation density, crystal orientation and geometry). The same features as with DDD simulations were recovered hinting at the general nature of the average yield point.

   c) An in-depth analysis of the accumulation of plastic strain in 2D DDD simulations showed that during avalanches irreversible structural changes take place. Plastic deformation also happens between these events, but these are quasi-reversible.

   Related publications: [A, D, F]

2. *Universality class of plastic deformation.* With the help of 2D DDD simulations I studied the avalanche behaviour of dislocation systems. I identified a universality class that is related to the critical behaviour of dislocations which is characterized by the absence of length and timescales that would limit the spatial extent of avalanches. This behaviour is inconsistent with the depinning scenario that was envisaged earlier to provide a general description for plasticity. The particular findings that lead to this conclusion are as follows:

a) The relaxation of initially random dislocation structures as well as those subject to some external perturbation were found to exhibit slow, scale-free relaxation characterized by self-similarity in the velocity distribution of dislocations.

b) The avalanche size distributions during quasi-static loading follow a scale-free distribution with a cut-off. The latter has been shown to be proportional with the system size at every stress level, that is, in the thermodynamic limit the avalanche size distribution is always scale-free.

c) The reason for this glassy behaviour is the long-range interaction between a large number of dislocations. As soon as the dynamics of a single dislocation line is considered, mean-field depinning is recovered, as shown by molecular dynamics simulations of a dislocation line traveling in a random alloy.

Related publications: [C, E, S].

3. *Statistics of internal disorder in dislocation systems.* The stochastic properties of crystal plasticity are due to the randomness in the dislocation microstructure. I, therefore, pursued to determine the distribution of local yield thresholds using 2D DDD simulations and, based on this result, developed a mesoscopic stochastic plasticity model. The particular related findings are as follows:

   a) The local yield threshold distribution was found to be characterized by a power-law distribution that lead to Weibull-type order statistics for stress values at the onset of subsequent avalanches. The mesoscopic model based on this observation and the lower-scale DDD models were compared in terms of stress-strain curves and their fluctuations that demonstrated the success of scale linking.

   b) A similar mesoscopic stochastic plasticity model was applied to study the deformation of shear softening materials (such as amorphous materials) and the role of the yield threshold distribution. It was shown that increased microstructural heterogeneity delays strain localization (that is, shear band formation and subsequent rupture) and leads to an increase of the plastic regime in the macroscopic stress–strain curves.

   Related publications: [I, J].

4. *Development of novel efficient numerical tools for dislocation dynamics.* Discrete dislocation dynamics simulations play an essential role in the particular field both from the modelling and theoretical perspectives. Two new methodological developments were performed that aim at increasing the numerical efficiency of these numerical tools. Firstly, a complex implicit scheme was proposed for the numerical solution of the equations of motion that lead to a significant (several magnitudes in some cases) speed up in the simulations. Secondly, a new spectral method was developed for satisfying various elastic

boundary conditions in 2D simulations. This method was shown to exhibit better computational efficiency than the FEM.

Related publications: [P, Q].

5. *Pattern formation of dislocations.* It is an ubiquitous feature of crystalline materials that upon plastic deformation dislocations accumulate and arrange into various patterns. Using theoretical approaches and numerical simulations I investigated this phenomenon and obtained the following results:

   a) I was involved in deriving a continuum density-based plasticity theory and its reformulation into a phase field model that gives a mesoscale representation of a 2D system of straight dislocations. The model was generalized to account for the distribution of geometrically necessary dislocations close to an impenetrable boundary.

   b) By the linear stability analysis of the governing partial differential equations it was shown, that the homogeneous solution is unstable and that the theory predicts the formation of dipolar walls with a certain wavelength.

   c) A stochastic extension of the continuum model was performed that yields identical patterning characteristics as lower-scale discrete dislocation dynamics simulations.

   d) The continuum model was generalized to curved dislocations in single slip based on the phase field formalism. For the first time, physics-based dynamical evolution equations were proposed for this scenario.

   Related publications: [B, G, H, M, O, U].

6. *Characterizing the dislocation network with HR-EBSD measurements.* High-resolution electron backscatter diffraction (HR-EBSD) is a novel non-destructive method giving access to the internal stresses and the GND distribution on the surface of a crystalline sample. This method was utilized at our laboratory and with its help the following results were obtained:

   a) The distribution of internal stresses in a deformed bulk Cu single crystal was determined and compared with numerical dislocation dynamics simulations. The fact that the tail of the distribution was found to decay as an inverse cubic function in both cases allowed us to use HR-EBSD to measure not only the geometrically necessary but also the statistically stored density of dislocations.

   b) The distribution of geometrically necessary dislocations was investigated in microsamples. In case of copper, an embryonic cellular structure was found that can be considered a transition state between bulk and nanoscale behaviour. The analysis of the components of the Nye dislocation density tensor lead to the conclusion

that most of the dislocations are found in inactive slip systems and were formed by reactions during deformation.

c) Similar behaviour was observed in tungsten cantilevers in front of a crack, namely, the dislocation structure that develops and shields the stress field around the crack tip was found to be built of dislocations that were not emitted from the crack tip, rather they were formed by dislocation reactions.

Related publications: [L, N, R, T].

7. *Utilizing acoustic emission in micromechanical experiments.*

Acoustic emission (AE) experiments were used extensively for bulk samples to investigate the stochastic features of plasticity. We developed an experimental set-up that, for the first time, allowed us to record AE signals of a microsample together with its stress-strain characteristics *in situ* in a scanning electron microscope. With this measurement the dislocation avalanche behaviour in Zn micropillars was investigated. It was found that these events analogous to earthquakes as the ubiquitous scaling-laws (that is, Gutenberg-Richter law, Omori law, productivity law) were found to hold in micropillars, too.

Related publications: [K, X].

4 Plans for future research

In this chapter I summarize the plans for my research in the next approx. 5 years. These topics are, in fact, the direct continuation of the work presented in the scientific part of this thesis. The proposed research activities will be mostly funded by the National Research, Development, and Innovation Office of Hungary through the 4-year grant OTKA-FK-138975 that started in September 2021.

The planned research continues to aim at providing a deeper understanding of the plastic behaviour of materials at the micron scale. The planned experimental and theoretical/numerical topics are grouped in four distinct, though related topics, as follows.

1. *Experimental investigations of the stochastic features of plasticity*

   (1.1) AE measurements for various materials and deformation mechanisms. As it was described in Sec. 2.4.4, the novel methodology of detecting AE signals during micro-compression developed at our laboratory has opened new perspectives in the experimental investigation of collective dislocation dynamics. In the near future we will investigate how the AE signals and their statistics depend on the material and deformation mechanism. Firstly, *twinning* (a typically strong source of AE signals) will be studied during the compression of *single crystalline Mg*. Depending on the orientation one can tune the proportion of twinning and dislocation glide on basal slip (two distinct deformation mechanisms) in the total deformation [V]. In collaboration with Kristián Máthis (Charles University, Czech Republic) we will investigate the differences in type (waveform and spectrum) and statistics (distribution of size and duration) of the AE signals corresponding to the two distinct processes. Secondly, we will conduct similar micro-compression experiments on other crystalline materials that exhibit pronounced twinning due to small stacking fault energy. In particular, we will investigate *pure Ag single and polycrystals* since it is known that in FCC the nature of criticality changes profoundly compared to HCP crystals [60, 126] and a CoCrFeNi high entropy alloy (HEA) that possesses improved mechanical properties, such as high hardness combined with ductility [127]. Thirdly, samples showing plastic instabilities of the *Portevin–Le Chatelier (PLC) effect* [128] will be examined. In such cases strain bursts can be observed even for bulk samples and it is known that AE signals can be detected for micropillars [see Fig. 4.1(a)] [K]. Here we will focus on how sample size influences this instability and the AE signals and whether one can classify the type of PLC instability based on the AE measurements.

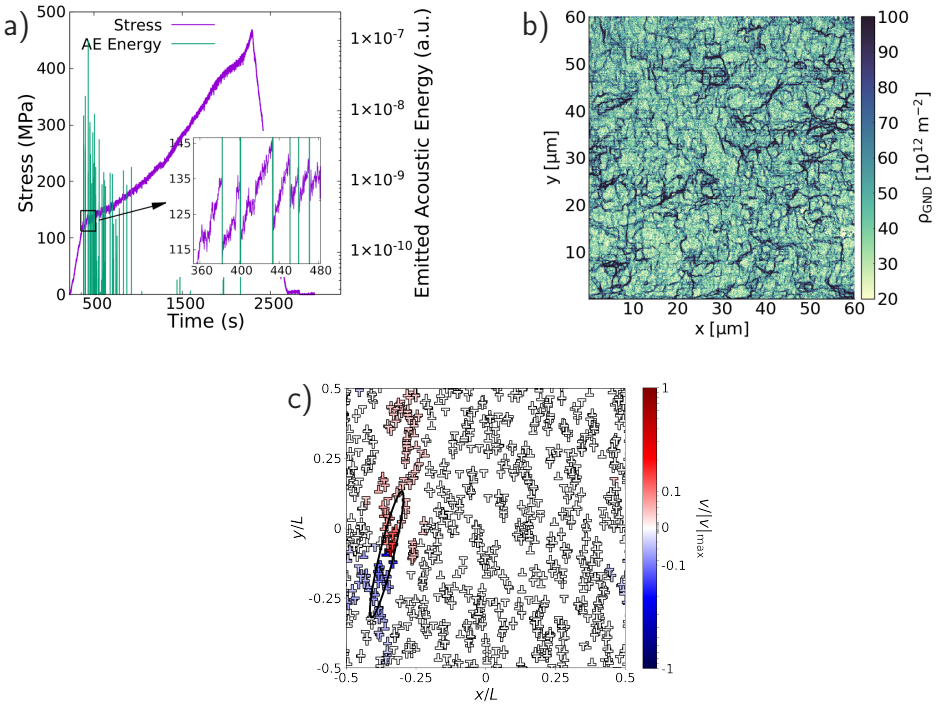

Figure 4.1: Preliminary experimental and numerical results. (a): Stress-time curve of a compressed Al-3Mg micropillar exhibiting the PLC effect. According to the inset the numerous AE events detected are in perfect correlation with the stress drops. (b): Distribution of GND densities on a bulk Cu single crystal deformed to 11% strain obtained using HR-EBSD. (c): An extended deformation mode determined from the dislocation velocities v at the onset of a plastic event in 2D DDD simulations. Note, that its spatial extension practically reaches the system size.

(1.2) Effect of irradiation. To further explore how the microstructural features of the crystal affect the stochastic response we will examine the role of point defects. Numerical simulations suggest that such a quenched disorder suppresses glassy behaviour [59, 61] characteristic of pure dislocation systems [E, 129]. A multi-energy proton irradiation scheme will be applied to Zn single crystals that was used successfully for metallic glasses [130]. Micropillar testing will be then carried out on irradiated micropillars coupled with AE measurements. In accordance with numerical predictions, suppression of the large strain bursts and a pronounced microplastic response is expected.

(1.3) AE for bulk materials. Bulk materials with HCP structure emit a large number of burst-like AE signals with scale-free energy distribution [17, 18, 126]. Temporal clustering similarly to that expressed by Omori-law for earthquakes has been investigated, but due to the huge number of signals only weak clustering was found [131, 132]. In order to assess whether our findings on temporal correlation on micropillars also apply for bulk materials we will conduct compression experiments on sub-mm size Zn single crystal samples directly placed on an AE sensor to reduce the reflections of the acoustic waves in the sample. This will reduce the length of the burst-like signals and allow for an analysis

with significantly better time resolution. These results are expected to answer whether the boundary conditions play any role in the observed scale-free phenomena.

2. *Micromechanical behaviour of materials*

   (2.1) Dislocation microstructure of deformed micropillars. As mentioned before, microstructure of crytalline materials plays a fundamental role in the properties of the observed stochastic behaviour [60, 126, 133]. Within this objective we will investigate in detail the microstructure of single crystalline micropillars that were compressed in points (1.1) and (1.2). The in-depth *post mortem* HR-EBSD and TEM investigations will clarify the type of dislocations and their geometrical properties that develop upon compression. According to our hypothesis, in HCP the microstructure mainly consists of straight edge dislocations or dislocation dipoles on the basal plane and the number of forest dislocations, and thus the role of reactions, is negligible. This would explain why single slip DDD simulations yield similar scaling properties [E, 129] than Zn micropillars [X]. The point defects created by irradiation and dislocation reactions in FCC samples are expected to drastically change this picture.

   (2.2) The role of dislocation reactions - bending experiments. In FCC samples oriented for multiple slip the size of strain bursts, as well as the number of AE bursts are significantly reduced (see, e.g., [132, N]). This well-known fact is believed to be due to dislocation reactions and the corresponding reduction in the distance travelled by dislocations [134]. Indeed, recent compression experiments on Cu single crystalline micropillars revealed that even at the μm scale a large number of geometrically necessary dislocations (GNDs) develop on inactive slip systems due to dislocation reactions that lead to the development of a cellular dislocation microstructure and strain hardening [T]. During the next years we will continue our collaboration with Katrin Schulz (Karlsruhe Institute of Technology, Germany) and Szilvia Kalácska (EMPA Thun, Switzerland) and investigate the microstructural evolution during bending experiments of single crystals (such as Cu, Zn, HEAs) with diameters $5-10$ μm. During bending a large GND content accumulates in the central region of the sample which makes such experiments especially suitable for studying reactions.

3. *Utilizing machine learning for micromechanics*

   In recent years machine learning (ML) has become a promising tool to unveil the most important microstructural features that determine plastic response from a large amount of data [135–140]. Recently, the method has been successfully applied for instrumented indentation experiments for the prediction of mechanical properties [141]. At our laboratory we will utilize ML algorithms to assess the local stress distribution from HR-EBSD measurements. To this end, we will perform a large number ($\sim$10,000) of nanoindentation

experiments on the surface of a pre-deformed Cu sample. Preliminary results showed, that a fractal-like dislocation pattern develops even close to the surface [see Fig. 4.1(b)]. The indentation hardness and other features of the indentation curve (such as the first pop-in stress) are known to be of stochastic character [142], presumably due to the fluctuations in the microstructure. We will utilize a supervised learning algorithm – Random Forest regression – trained over a set of HR-EBSD data (local GND density and stresses as well as the components of the Nye dislocation density tensor) and the corresponding nanoindentation curves. The results will yield which features of the local microstructure influence local hardness and are expected to allow us to predict the distribution of local strength directly from HR-EBSD measurements. Since the research group of the PI does not have experience with ML, that part of this objective will be carried out in collaboration with Katrin Schulz (Karlsruhe Institute of Technology, Germany), an expert of this field [136, 143].

4. *Numerical modelling of the local stochastic processes of the yielding transition*

   (4.1) Identifying collective modes in crystalline plastic deformation. Using conceptually simple 2D DDD simulations it was found that dislocation systems exhibit glassy features in the form of large avalanches that may span the entire system even at small applied stresses [E] signalling an extended critical behaviour that was confirmed in more complex 3D DDD simulations as well [129]. The 2D system was also sufficient to describe the AE signals and their temporal correlations [X]. In order to identify collective modes that are triggered during avalanches we will apply linear stability analysis of the equations of motion of 2D DDD systems. Preliminary results revealed long-range dynamical correlations between dislocations that is expected to explain the scale-free behaviour observed before [Fig. 4.1(c) shows an exemplary deformation mode spanning the whole simulation area]. We will quantify the spatial extension of these modes and investigate their response to an external stress especially close to the onset of a plastic event. We will also study how quenched disorder (such as vacancies or solute atoms) and a finite threshold in the mobility law (corresponding to, e.g., Peierls stress) localizes the eigenmodes and, according to our hypothesis, lead to smaller strain bursts. The effect of irradiation studied under objective (1.2) will make it possible to directly compare our predictions with experimental data.

   (4.2) Local yield stress distributions and weakest link theory. Plastic instabilities appearing in the form of strain bursts are due to the disorder in the microstructure that can be formulated using the concept of local yield thresholds (see the Background section). This idea has been also applied to amorphous materials where a methodology has been developed to measure this distribution using molecular dynamics simulations [144]. We will establish a similar technique for 2D DDD simulations, that is, local regions of the whole

simulation area will be tested with varying region sizes. This study is expected not only to answer what the local yield stress distribution is, but also to identify the scale that corresponds to a representative volume element. It is expected that with an increasing strength of quenched disorder the local yield threshold represents a smaller and smaller region that makes application of weakest link arguments [D, I] straightforward.

(4.3) Developing stochastic mesoscopic models for plasticity. As a next step stochastic elastoplastic models will be constructed where the local yield threshold is the main input [145]. Here we will aim at developing models that yield identical results to experiments performed under objective (1.1). (i) For single crystals correlations in the yield threshold between adjacent cells will be introduced to account for long-range dynamic correlations. (ii) For PLC materials aging will be introduced to every cell similarly to the model used for describing plastic instabilities during the compression of snow [146]. We will focus on understanding the relation between local strain bursts and the AE signals measured in the experiments.

5 List of publications

5.1 Publications referenced in my PhD thesis

[1] I. Groma and **P. D. Ispánovity**, *Role of anharmonicity in dislocation patterning*, Phys. Rev. B **76**, 054120 (2007).

[2] **P. D. Ispánovity** and I. Groma, *The probability distribution of internal stresses in externally loaded 2D dislocation systems*, J. Stat. Mech., P12009 (2008).

[3] **P. D. Ispánovity**, I. Groma and G. Györgyi, *Evolution of the correlation functions in two-dimensional dislocation systems*, Phys. Rev. B **78**, 024119 (2008).

[4] F. F. Csikor, M. Zaiser, **P. D. Ispánovity** and I. Groma, *The role of density fluctuations in the relaxation of random dislocation systems*, J. Stat. Mech., P03036 (2009).

5.2 Publications this thesis is based on

[A] **P. D. Ispánovity**, I. Groma, G. Györgyi, F. F. Csikor and D. Weygand, *Submicron plasticity: yield stress, dislocation avalanches, and velocity distribution*, Phys. Rev. Lett. **105**, 085503 (2010).
Own contribution: I conceived the original idea for the research, developed and carried out the simulations, performed the data analysis, developed the theoretical background and wrote the original version of the manuscript.

[B] I. Groma, G. Györgyi and **P. D. Ispánovity**, *Variational approach in dislocation theory*, Philos. Mag. **90**, 3679 (2010).
Own contribution: I developed and carried out the simulations of the paper, performed the data analysis, took part in the discussions on the theory and contributed to the final version of the manuscript.

[C] **P. D. Ispánovity**, I. Groma, G. Györgyi, P. Szabó and W. Hoffelner, *Criticality of relaxation in dislocation systems*, Phys. Rev. Lett. **107**, 085506 (2011).
Own contribution: I conceived the original idea for the research, developed and carried out the simulations, performed the data analysis, developed the theoretical background and wrote the original version of the manuscript.

[D] **P. D. Ispánovity**, Á. Hegyi, I. Groma, G. Györgyi, K. Ratter and D. Weygand, *Average yielding and weakest link statistics in micron-scale plasticity*, Acta Mater. **61**, 6234 (2013).
Own contribution: I conceived the original idea for the research, took part in the design of the experiments, developed and carried out the simulations, performed the data analysis, developed the theoretical background and wrote the original version of the manuscript.

[E] **P. D. Ispánovity**, L. Laurson, M. Zaiser, I. Groma, S. Zapperi and M. J. Alava, *Avalanches in 2D Dislocation Systems: Plastic Yielding is not Depinning*, Phys. Rev. Lett. **112**, 235501 (2014).
Own contribution: I conceived the original idea for the research, developed and partially carried out the simulations, performed the data analysis, developed the theoretical background and took part in writing the original version of the manuscript.

[F] P. Szabó, **P. D. Ispánovity** and I. Groma, *Plastic strain is a mixture of avalanches and quasireversible deformations: Study of various sizes*, Phys. Rev. B **91**, 054106 (2015).
Own contribution: I took part in conceiving the original idea for the research, developed the simulations, took part in the data analysis, took part in developing the theoretical background and contributed to the final version of the manuscript.

[G] I. Groma, Z. Vandrus and **P. D. Ispánovity**, *Scale-free phase field theory of dislocations*, Phys. Rev. Lett. **114**, 015503 (2015).
Own contribution: I took part in conceiving the original idea for the research, took part in developing the simulations, took part in the data analysis, took part in developing the theoretical background and contributed to the final version of the manuscript.

[H] I. Groma, M. Zaiser and **P. D. Ispanovity**, *Dislocation patterning in a two-dimensional continuum theory of dislocations*, Phys. Rev. B **93**, 214110 (2016).
Own contribution: I developed and carried out the simulations, took part in the data analysis, took part in developing the theoretical background and contributed to the final version of the manuscript.

[I] **P. D. Ispánovity**, D. Tüzes, P. Szabó, M. Zaiser and I. Groma, *Role of weakest links and system-size scaling in multiscale modeling of stochastic plasticity*, Phys. Rev. B **95**, 054108 (2017).
Own contribution: I conceived the original idea for the research, took part in developing the simulations, performed the data analysis, developed the theoretical background and wrote the original version of the manuscript.

[J] D. Tüzes, **P. D. Ispánovity** and M. Zaiser, *Disorder is good for you: The influence of local disorder on strain localization and ductility of strain softening materials*, Int. J. Fract. **205**, 139 (2017).
Own contribution: I took part in developing the simulations, took part in the data analysis, took part in developing the theoretical background and contributed to the final version of the manuscript.

[K] Á. I. Hegyi, **P. D. Ispánovity**, M. Knapek, D. Tüzes, K. Máthis, F. Chmelík, Z. Dankházi, G. Varga and I. Groma, *Micron-Scale Deformation: A Coupled In Situ Study of Strain Bursts and Acoustic Emission*, Microsc. Microanal. **23** (6), 1076 (2017).
Own contribution: I conceived the original idea for the research, took part in the design of the experiments and contributed to the final version of the manuscript.

[L] Sz. Kalácska, I. Groma, A. Borbély and **P. D. Ispánovity**, *Comparison of the dislocation density obtained by HR-EBSD and X-ray profile analysis*, Appl. Phys. Lett. **110**, 091912 (2017).
Own contribution: I developed and carried out the simulations of the paper, performed the data analysis, took part in the discussions on the theory and contributed to the final version of the manuscript.

[M] R. Wu, D. Tüzes, **P. D. Ispánovity**, I. Groma, T. Hochrainer and M. Zaiser, *Instability of dislocation fluxes in a single slip: Deterministic and stochastic models of dislocation patterning*, Phys. Rev. B **98**, 054110 (2018).
Own contribution: I took part in developing the SCPM simulations, took part in the data analysis, took part in the discussions on the theory and contributed to the final version of the manuscript.

[N] Sz. Kalácska, Z. Dankházi, Gy. Zilahi, X. Maeder, J. Michler, **P. D. Ispánovity** and I. Groma, *Investigation of geometrically necessary dislocation structures in compressed Cu micropillars by 3-dimensional HR-EBSD*, Mater. Sci. Eng. A **770**, 138499 (2020).
Own contribution: I took part in the design of the experiments, contributed to the data analysis and contributed to the final version of the manuscript.

[O] **P. D. Ispánovity**, S. Papanikolaou and I. Groma, *The Emergence and Role of Dipolar Dislocation Patterns in Discrete and Continuum Formulations*, Phys. Rev. B **101**, 024105 (2020).
Own contribution: I conceived the original idea for the research, developed and carried out the simulations, performed the data analysis, contributed to the development of the theoretical background and took part in writing the original version of the manuscript.

[P] G. Péterffy and **P. D. Ispánovity**, *An efficient implicit time integration method for discrete dislocation dynamics*, Model. Simul. Mater. Sc. **28**, 035013 (2020).
Own contribution: I conceived the original idea for the research, took part in developing the simulations and took part in writing the original version of the manuscript.

[Q] D. Berta, I. Groma, and **P. D. Ispánovity**, *Efficient numerical method to handle boundary conditions in 2D elastic media*, Model. Simul. Mater. Sc. **28**, 035014 (2020).
Own contribution: I conceived the original idea for the research, took part in developing the simulations, developed the theoretical background and took part in writing the original version of the manuscript.

[R] Sz. Kalácska, J. Ast, **P. D. Ispánovity**, J. Michler and X. Maeder, *3D HR-EBSD characterization of the plastic zone around crack tips in tungsten single crystals at the micron scale*, Acta Mater. **200**, 211 (2020).
Own contribution: I took part in the Burgers vector analysis using HR-EBSD and contributed to the final version of the manuscript.

[S] G. Péterffy, **P. D. Ispánovity**, M. E. Foster, X. Zhou and R. B. Sills, *Length scales and scale-free dynamics of dislocations in dense solid solutions*, Mater. Theory **4**, 1 (2020).
Own contribution: I conceived the original idea for the research, took part in the data analysis, developed the theoretical background and took part in writing the original version of the manuscript.

[T] K. Zoller, Sz. Kalácska, **P. D. Ispánovity** and K. Schulz, *Microstructure evolution of compressed micropillars investigated by in situ HR-EBSD analysis and dislocation density simulations*, Comptes Rendus. Physique **22**, Online first 1–27 (2021).
Own contribution: I took part in conceiving the original idea for the research, took part in the data analysis, took part in developing the theoretical background and took part in writing the original version of the manuscript.

[U] I. Groma, **P. D. Ispánovity** and T. Hochrainer, *On the dynamics of curved dislocation ensembles* Phys. Rev. B **103**, 174101 (2021).
Own contribution: I took part in discussions on the developed theory and contributed to the final version of the manuscript.

[V] K. Máthis, M. Knapek, F. Šiška, P. Harcuba, D. Ugi, **P. D. Ispánovity**, I. Groma and K. S. Shin, *On the dynamics of twinning in magnesium micropillars*, Mater. Des. **203**, 109563 (2021).
Own contribution: I took part in the design of the experiments and contributed to the final version of the manuscript.

[X] **P. D. Ispánovity**, D. Ugi, G. Péterffy, M. Knapek, Sz. Kalácska, D. Tüzes, Z. Dankházi, K. Máthis, F. Chmelík and I. Groma, *Dislocation Avalanches: Earthquakes on the Micron Scale* arXiv preprint: 2107.13334 (2021).
Own contribution: I conceived the original idea for the research, took part in the design of the experiments, took part in developing the simulations, performed the data analysis, developed the theoretical background and wrote the original version of the manuscript.

5.3 Further publications after obtaining my PhD degree

5.3.1 Publications in international peer-reviewed journals

[1] **P. D. Ispánovity**, B. Bakó, D. Weygand, W. Hoffelner and M. Samaras, *Impact of gamma′ particle coarsening on the critical resolved shear stress of nickel-base superalloys with low aluminium and/or titanium content*, J. Nucl. Mater. **416**, 55 (2011).

[2] I. Groma, G. Györgyi and **P. D. Ispánovity**, *Comment on "Dislocations Jam at Any Density"*, Phys. Rev. Lett. **108**, 269601 (2012).

[3] I. Groma, D. Tüzes and **P. D. Ispánovity**, *Asymmetric X-ray line broadening caused by dislocation polarization induced by external load*, Scripta Mater. **68**, 755 (2013).

[4] Zs. Kovács, M. Ezzeldien, K. Máthis, **P. D. Ispánovity**, F. Chmelík and J. Lendvai, *Statistical analysis of acoustic emission events in torsional deformation of a Vitreloy bulk metallic glass*, Acta Mater. **70**, 113 (2014).

5.3.2 Conference proceedings

[1] M. Milner-Bolotin, V. Milner, A. M. Tasnádi, H. T. Weck, I. Groma and **P. D. Ispánovity**, *Contemporary Experiments and New Devices in Physics Classrooms*, J. Phys.: Conf. Ser. **1929**, 012067 (2021).

5.3.3 Publications in Hungarian journals

[1] Á. Hegyi, K. Ratter, **P. D. Ispánovity** and I. Groma, *Mikroméretű minták deformációinak vizsgálata*, Fizikai Szemle **62**, 77 (2012).

[2] M. Hömöstrei, T. L. Pham, Á. Beregi, A. Laukó, Á. Béda, P. Nagy, **P. D. Ispánovity** and P. Jenei, *Ifjú Fizikusok Nemzetközi Versenye magyar szemmel*, Fizikai Szemle **64**, 430 (2014).

[3] L. Kovács, D. Nagy, M. Szakály, M. Hömöstrei, **P. D. Ispánovity**, J. Asbóth, D. Tüzes and P. Jenei, *Ifjú Fizikusok Nemzetközi Versenye 2018 – magyar szemmel – 1. rész*, Fizikai Szemle **69**, 201 (2019).

[4] M. Gyulai, Á. Kadlecsik, M. Vavrik, M. Hömöstrei, **P. D. Ispánovity**, M. Vincze and P. Jenei, *Ifjú Fizikusok Nemzetközi Versenye 2018 – magyar szemmel – 2. rész*, Fizikai Szemle **69**, 314 (2019).

5.4 Equivalent publication number

Equivalent publication number according to the evaluation criteria of the Physics Section of the Habilitation Committee of the Eötvös Loránd University (point 1. of Appendix I.): **48**.

5.5 Citation metrics

Number of independent citations according to the Hungarian Academy of Sciences, Section of Physical Sciences (IX) criteria: **290** (see Tab. 5.1).

I request that the citation metrics of my scientific publications be computed using the citation data of the MTMT database. I declare that my MTMT identification number is: **10027552**.

Ispánovity Péter Dusán 's summary of scientific and educational work
HAS Section of Physical Sciences (XI.) (2021.09.22)

Number of comlete scientific publications[1]	1-5 authors	6-10 authors	11-20 authors	21-100 authors	> 100 authors („author")[2]	> 100 authors („contributor")[3]
Original journal article	23	7	0	0	0	0
Summary article	0	0	0	0	0	0
Reviewed conference paper (At least 3 pages)	0	0	0	0	0	0
Books, Book chapters	0	0	0	0	0	0
Number of all complete scientific publications	23	7	0	0	0	0

Independent citations[4] of complete scientific publications in complete scientific works (without self citations and co-authors' citations for common publications):

Teljes tudományos közlemények[1] száma	1-5 authors	6-10 authors	11-20 authors	21-100 authors	> 100 authors („author")[2]	> 100 authors („contributor")[3]
Number of independent citations	189	101	0	0	0	0
Weight factor (W)	1	0.75	0.5	0.25	1	0
Effective citations	189	75.75	0	0	0	0

Independent citations of the applicant's complete scientific work:[4]

Characteristics	All citations	Effective citations
Independent citations of all complete scientific work	290	264.75
Independent citations of publications since getting degree (2009)	273	247.75

H-index calculated from independent and dependent citations[4]	11
H-index calculated from independent citations[4]	9

Number of the applicant's other publications:

	Number of publications
Higher educational books and book chapters	0
Unreviewed conference papers	0
Edited books	0
Popular science	2
Report	0
Other	1

Table 5.1: Statistics of publications and citations as extracted from the MTMT database.

6 Brief summary of a scientific talk

In my scientific talk I will give a concise overview of my research activities after carried out obtaining my PhD degree. I will start with a quick introduction on the background and the most important findings that motivated my work. The rest of the talk will be split into three parts according to the sections of Chapter 2.

Firstly, my results related to the investigations of the avalanche behaviour in dislocation systems will be presented. After describing the simulation methods I will show how can one define a yield stress in the statistical sense for micron and submicron scale specimens. This yield stress separates two dynamically different regimes based on which it was suggested that a dynamical phase transition takes place at yielding. I will show that the in-depth analysis of the distribution of dislocation avalanche sizes that the picture of a phase transition cannot hold, because the system is characterized by scale-free dynamics and behaves as one being always in a critical state.

Secondly, the continuum theory of dislocations and its variational formulation will be presented. This theory is able to describe properly dislocation fluxes and the corresponding plastic deformation in 2D dislocation systems. It will be shown how the theory predicts pattern formation and these predictions will be compared with lower scale discrete simulations. Finally, the generalization of the theory to 3D will be outlined.

In the last part of my presentation our recent experimental findings will be discussed. I will briefly introduce the method of high-resolution electron backscatter diffraction (HR-EBSD) and present the results we obtained using this novel technique. The emphasis will be placed on the microsamples and the determination of the internal dislocation structure. I will conclude with introducing the coupling of acoustic emission and microcompression experiments and show how experiments using this new methodology reveal temporal clustering of dislocation avalanches that are analogous to earthquakes.

7 Teaching activities

7.1 Lectures and tutorials held at the Eötvös Loránd University

The following list is an excerpt from the neptun e-learning system.

Semester	Subject code	Subject name	Course type
2007/08/1	fg1n2K04	*Physics (mechanics and thermodynamics)*	tutorial
2007/08/2	fggn8201g	*Physics (electromagnetism and optics)*	tutorial
2007/08/2	fg1n2K05	*Physics (electromagnetism and optics)*	tutorial
2007/08/2	ff1n2s01:2	*Mechanics*	tutorial
2007/08/2	ff1n2s03	*Electromagnetism*	tutorial
2008/09/1	ff1n2o02	*Criterion class in Physics*	tutorial
2008/09/1	ff1n2o02	*Criterion class in Physics*	tutorial
2008/09/1	fg1n2K04	*Physics (mechanics and thermodynamics)*	tutorial
2008/09/1	ff1n2s01:2	*Mechanics*	tutorial
2008/09/1	ff1n2s01:2	*Mechanics*	tutorial
2008/09/1	fg1n2K04	*Physics (mechanics and thermodynamics)*	tutorial
2008/09/2	ff1n2s03	*Electromagnetism*	tutorial
2008/09/2	ff1n2s03	*Electromagnetism*	tutorial
2011/12/2	ff1c4s12	*Classical physics (laboratory)*	laboratory course
2011/12/2	ff1n1s02	*Mechanics of continuous phases*	exp. demonstration
2011/12/2	ff1c1s02e	*Mechanics of continuous phases - advanced*	exp. demonstration
2012/13/1	ff1c2s01e	*Mechanics*	tutorial
2012/13/1	ff1c2s01e	*Mechanics*	tutorial
2012/13/1	fffn111	*Mechanics*	exp. demonstration
2012/13/2	ff1c4s12	*Classical physics (laboratory)*	laboratory course
2012/13/2	ff1n1s02	*Mechanics of continuous phases*	exp. demonstration
2012/13/2	ff1c1s02e	*Mechanics of continuous phases - advanced*	exp. demonstration

Semester	Subject code	Subject name	Course type
2013/14/1	ff1n2s01	*Mechanics*	tutorial
2013/14/1	ff1c1s01e	*Mechanics*	exp. demonstration
2013/14/1	f3fn1af1	*Applied physics I.*	lecture
2013/14/2	ff1c1s03e	*Electromagnetism (advanced)*	exp. demonstration
2013/14/2	FIZ/1/026E	*Current topics of materials science*	seminar
2014/15/1	ff1c1s01e	*Mechanics*	exp. demonstration
2014/15/1	ff1c2s01e	*Mechanics*	tutorial
2014/15/1	ff1c2s01e	*Mechanics*	tutorial
2014/15/1	f3fn1af1	*Applied physics I.*	lecture
2014/15/2	ff1c1s02	*Mechanics of continuous phases*	exp. demonstration
2014/15/2	ff1c1s02e	*Mechanics of continuous phases - advanced*	exp. demonstration
2014/15/2	ff1c1s04	*Thermodynamics*	exp. demonstration
2014/15/2	ff5t2s03	*Electromagnetism*	tutorial
2015/16/1	ff1c1s01e	*Mechanics*	exp. demonstration
2015/16/1	ff1c2s01e	*Mechanics*	tutorial
2015/16/1	ff1c2s01e	*Mechanics*	tutorial
2015/16/1	f3fn1af1	*Applied physics I.*	lecture
2015/16/2	ff1c1s04	*Thermodynamics*	lecture
2015/16/2	ff1c1s02	*Mechanics of continuous phases*	exp. demonstration
2015/16/2	ff1c2s03e	*Electromagnetism (advanced)*	tutorial
2015/16/2	ff1c2s03e	*Electromagnetism (advanced)*	tutorial
2016/17/1	ff1c1s01e	*Mechanics*	exp. demonstration
2016/17/1	ff1c2s01e	*Mechanics*	tutorial
2016/17/1	ff1c2s01e	*Mechanics*	tutorial
2016/17/1	f3fn1af1	*Applied physics I.*	lecture
2016/17/2	ff1c1s04	*Thermodynamics*	lecture
2016/17/2	ff5t1s57	*New devices and technologies*	lecture
2016/17/2	ff5t2s03b	*Electromagnetism*	tutorial
2017/18/1	mechf17ea	*Mechanics*	lecture
2017/18/1	mechaf17ga	*Mechanics*	tutorial
2017/18/2	termof17ea	*Thermodynamics*	lecture
2017/18/2	ff5t1s57	*New devices and technologies*	lecture
2018/19/1	mechf17ea	*Mechanics*	lecture

Semester	Subject code	Subject name	Course type
2018/19/2	termof17ea	*Thermodynamics*	lecture
2018/19/2	ff5t1s57	*New devices and technologies*	lecture
2019/20/1	mechf19ea	*Mechanics*	lecture
2019/20/1	mechaf19ga	*Mechanics*	tutorial
2019/20/2	hotanef19va	*Thermodynamics and Continuum Mechanics - Adv.*	lecture
2019/20/2	ff5t1s57	*New devices and technologies*	lecture
2020/21/1	mechf19ea	*Mechanics*	lecture
2020/21/1	mechaf19ga	*Mechanics*	tutorial
2020/21/2	hotanef19va	*Thermodynamics and Continuum Mechanics - Adv.*	lecture
2020/21/2	ujeszkf19eo	*New devices and technologies*	lecture
2021/22/1	mechf19ea	*Mechanics*	lecture

7.2 Supervision of PhD students

In the following, students who did or are currently doing their PhD research under my supervision are listed. All the activities took place at the Eötvös Loránd University, Budapest, Hungary.

- 2012–2018: Dániel Tüzes, title of the thesis: *Stochastic Properties of Dislocation Motion and Rearrangement* (co-supervised with Prof. István Groma)
- 2013–2016: Ádám Hegyi, topic: *Statistical properties of deformation avalanches* (he obtained his pre-degree certificate but did not submit a thesis)
- 2017–: Dávid Ugi, topic: *Experimental investigation of dislocation avalanches*
- 2018–: Gábor Péterffy, topic: *Dynamical correlations in dislcoation systems*
- 2020–: Dénes Berta, topic: *The role of curvature and internal disorder in dislocation systems*
- 2021–: Tabish Aftab, topic: *Stress fluctuations in heterogeneous materials*

7.3 Supervision of undergraduate students

In the following, students who finished their diploma research under my supervision are listed. All the activities took place at the Eötvös Loránd University, Budapest, Hungary.

- 2015: Péter István Zöld, Physics Teacher MA, *Alakemlékező ötvözetek/Shape Memory Alloys*
- 2016: Gábor Péterffy, Physics BSc, *Hatékony implicit numerikus séma kidolgozása és alkalmazása diszkrét diszlokáció dinamikai szimulációkban/Development and Application of an Efficient Implicit Scheme in Discrete Dislocation Dynamics Simulations*
- 2016: Beáta Herke, Physics BSc, *A papírsatu fizikája/Physics of the Paper Vice*
- 2017: Dávid Ugi: Materians Science MSc, *Egykristályok mikromechanikai tulajdonságainak kísérleti vizsgálata/Experimental Investigation of the Micromechanic Properties of Single Crystals*
- 2017: Roland Kovács, Physics Teacher MA, *Mozgások számítógépes elemzése a Tracker program segítségével/Computer Analysis of Motions with Tracker*
- 2018: Gábor Péterffy, Physicist MSc, *A besugárzás képlékeny alakváltozásra gyakorolt hatásának modellezése a mikronos mérettartományban/Modelling of the Impact of Irradiation on the Plastic Deformation at the Micron Scale*
- 2018: Dénes Berta, Physics BSc, *Hatékony numerikus módszer a határfeltételek figyelembevételére rugalmas anyagban/Efficient Numerical Scheme for Handling Boundary Conditions in an Elastic Medium*
- 2019: Janka Molnár, Physics BSc, *Dinamikai korrelációk és deformációs lavinák/Dynamical Correlations and Deformation Avalanches*
- 2020: Dénes Berta, Physicist MSc, *Local Yield Stress in 2D Dislocation Systems*
- 2020: Ecsedi Grácia Antónia, Physics Teacher MA, *Napelemes eszközök használatának előnyei a középiskolában/Advantages of Using Devices with Solar Panels in Secondary Schools*
- 2021: Dániel Godó, Physics BSc, *Deformált Cu egykristályok mikroszerkezeti inhomogenitásának vizsgálata indentációs és EBSD mérések alapján/Investigation of the Microstructural Inhomogeneity of Deformed Cu single crystals using indentation and EBSD measurements*
- 2021: Gergő Bence Mamuzsics, Physics BSc, *Cu egykristályok hajlítása során kialakuló diszlokációs mikroszerkezet kísérleti vizsgálata/Experimental Investigation of the Dislocation Microstructure Developing in During Bending of Cu Single Crystals*

7.4 Participation of my students at OTDK conferences

- 2015: Gergely Dálya And Kornél Kapás, *A deformáció hatása a réz egykristály felületén kialakuló fraktál dimenziójára/The Effect of Deformation on the Dimension of the Fractal Developing on the Surface of Cu Single Crystals*
- 2017: Gábor Péterffy, *Hatékony implicit numerikus séma kidolgozása és alkalmazása diszkrét diszlokáció dinamikai szimulációkban/Development and Application of an Efficient Implicit Scheme in Discrete Dislocation Dynamics Simulations*, 3rd place
- 2017: Dávid Ugi, *Zn egykristály mikromechanikai tulajdonságainak vizsgálata/Micromechanical Properties of Zn Single Crystals*, 2nd place
- 2019: Dénes Berta, *Hatékony numerikus módszer a határfeltételek figyelembevételére rugalmas anyagban/Efficient Numerical Scheme for Handling Boundary Conditions in an Elastic Medium*, 3rd place, special award

7.5 Tutoring

Since 2013 are I am involved in selecting and tutoring the students participating at the International Young Physicists' Tournament (IYPT). Five times I also travelled with the team to the international event where I took part as a Team Leader.

8 Outline of a lecture course

8.1 Description of the selected lecture course

The lecture course I selected for my habilitation talk is *Mechanics* (subject code: mechf19ea, 2×90 minutes per week). I have been the lecturer of this course for 5 years now, and the number of attending students was between 50 and 100 every year. The course is primarily meant for first year Physics BSc and Physics Teacher MA students, and this is their first physics-related course at the university, which also adds to its importance. I note that there exists a parallel advanced course for mechanics that is meant for Physics BSc students with extraordinary skills. Consequently, in this course the emphasis is not put on complicated analytical derivations rather we focus on the proper foundations of the physical quantities and concepts (such as energy, moment of inertia, etc.).

As well-known, mechanics is concerned with describing the motion of objects and to understand its causes. During this lecture classical mechanics is covered, that is, the route paved by Newton is followed and we consider force as a central quantity in the theoretical description. During the course of the semester, firstly, kinematics are presented together with a brief introduction of the necessary mathematical formulations, such as derivatives and vector calculus. This is followed by stating the Newton's laws, that is, the fundamental dynamic equations of a point-like object. Conservative forces are then introduced together with the concept of work, kinetic and potential energies. Afterwards, the behaviour of a system of particles will be discussed followed by an in-depth analysis of harmonic oscillators. The semester then continues with demonstrating how the Newtonian equations change in an accelerating reference frame. The final lectures deal with the theory of gravitation, perhaps the most influential result obtained using Newtonian mechanics and then the semester concludes with the mechanics of solid bodies.

As mentioned above, the aim of this course is not only to present mechanics as a physical theory in a scientifically concise manner but also, being their first physics-related lecture, to increase the motivation and involvement of the students and to develop a solid understanding of the main physical concepts that their latter courses can build upon. To this end, lectures are complemented by demonstrative experiments that are performed on the stage during the lectures. The lecturer must also take in to account, that the background knowledge of participating

students exhibits a large variance, so, explanations and mathematical derivations should be presented in a way that assumes as little prior knowledge as possible. To assist the students in their studies, the lecture follows the notations and logic of the textbook referenced below.

Textbook: A. Hudson and R. Nelson: University Physics (chapters I-XVI), Harcourt College Publishers (1987).

8.2 Lecture course topics

In a semester on average 25 lectures take place. The topics covered are as follows.

1. *Kinematics of point-like objects I.*
   Scope of physics and its methodologies; experiment with a Mikola-tube; SI metric system; measurement errors; limits of physical theories; space-time in Newtonian mechanics; linear motion: displacement function, coordinate system, displacement 'vector', travelled distance

2. *Kinematics of point-like objects II.*
   Average velocity 'vector'; basics of differentiation; definition of instantaneous velocity

3. *Kinematics of point-like objects III.*
   Linear motion: average acceleration, instantaneous acceleration, the role of the sign of acceleration; linear motion with constant acceleration; free fall

4. *Kinematics of point-like objects IV.*
   Description of planar and 3D motions with different coordinate systems; meaning of dimension; displacement vector; path; velocity; geometric interpretation of the velocity; acceleration; general description of the linear uniform motion; projectile motion

5. *Circular motion*
   Polar coordinates; quantities describing uniform circular motion (radius, angular rotation, angular velocity, period, frequency), centripetal acceleration, non-uniform circular motion; tangential acceleration; general non-linear motions

6. *Dynamics of point-like objects I.*
   Historical overview of the development of the concepts dynamics; concept of interaction; Newton's First Law; inertial reference frame; definition of mass/inertia; concept of force

7. *Dynamics of point-like objects II.*
   Newton's Second Law; Newton's Third Law; concept of superposition; steps of the solution of a dynamics problem; force laws: force of gravity, force of a spring, constraint forces

8. *Dynamics of point-like objects III.*
   Equations of motion in the presence of constraint forces; motion on a slope; centripetal force; conical pendulum; static and dynamic friction; motion of a ball in a viscous fluid

9. *Dynamics of point-like objects IV.*
   Solution of the equations of motion in the presence of viscous drag; differential equation; the role of free parameters; determination of the velocity and displacement using integral calculus

10. *Work and energy*
    Work during linear motion; work of a varying force; work for a curved path; kinetic energy; theorem of work for a linear motion with uniform acceleration; theorem of work for a general motion; power

11. *Conservative forces*
    Conservative and non-conservative forces; potential energy; conservation of mechanical energy; energy diagram; determination of the force from the potential energy; concept of gradient

12. *Rocket motion*
    Momentum; conservation of momentum for two particles; impulse; rocket propulsion

13. *Mechanics of systems of particles*
    Elastic and inelastic collisions; planar elastic collisions; centre of mass; theorem for the centre of mass; conservation of momentum for a system of particles; description of collisions in a reference frame attached to the centre of mass; momentum and kinetic energy of a system of particles

14. *Harmonic oscillator I.*
    Harmonic oscillator; equation of motion as a differential equation; amplitude; angular frequency; phase; free parameters; initial conditions; relation of circular and harmonic motion; energetics of harmonic motion; harmonic motion in gravitational field; motion of a pendulum

15. *Harmonic oscillator II.*
    Damping due to friction; damped oscillator; equation of motion and its solution; the underdamped and the overdamped case; oscillator damped with dynamic friction; equation of motion and its solution

16. *Harmonic oscillator III.*
    Driven oscillator; resonance; resonance curve; phase shift; superposition of oscillators with the same frequency; superposition of oscillators with different frequencies

17. *Non-inertial reference frames I.*
    Description of motion in a non-inertial reference frame; reference frames with parallel axes; fictitious forces; rotating reference frames; angular velocity vector

18. *Non-inertial reference frames II.*
    Centrifugal force; Coriolis force and its effect on moving objects near the Earth; Foucault pendulum; Eötvös balance; phenomena on the rotating Earth

19. *Gravitation I.*
    Kepler's laws of planetary motion; mathematical properties of an ellipse; central force fields; angular momentum and its conservation

20. *Gravitation II.*
    Areal velocity; Newton's law of universal gravitation; The Cavendish experiment; work of the gravitational field

21. *Gravitation III.*
    Potential energy; conservation of mechanical energy during planetary motion; energetics of planetary motion; escape velocities

22. *Mechanics of rigid bodies I.*
    Torque; line of action; torque as a vector; centre of gravity; types of equilibrium

23. *Mechanics of rigid bodies II.*
    Conditions of equilibrium of a rigid body; kinematics of rotational motion; uniform and non-uniform rotational motion; rolling motion; kinetic energy for a rotational motion around a fixed axis; moment of inertia; Parallel axis theorem

24. *Mechanics of rigid bodies III.*
    Angular momentum of a system of particles; theorem for the angular momentum; angular momentum of a rigid body rotating around a fixed axis; fundamental dynamical equation of rotational motion; conservation of angular momentum; angular momentum of a symmetric rotating body

25. *Mechanics of rigid bodies IV.*
    Work and work theorem for rotating motion; physical pendulum; general motion of a rigid body; planar motion of a rigid body; gyroscope; torque-free and torque-induced precession

8.3 Outline of three lectures

I present here the outline of lectures 18, 20 and 25. Each lecture is 2×45 minutes long. During the lectures demonstrative experiments are shown to increase the motivation of the students and to support the physical argumentation. In the descriptions below the experiments to be carried out are explicitly mentioned.

Lecture 18: Non-inertial reference frames II.

During the preceding lecture it was calculated how the acceleration of an object can be determined from the coordinates measured in a rotating reference frame. We assumed that the angular velocity ω is constant and we concluded that

$$m\boldsymbol{a} = \boldsymbol{F}_{\mathrm{e}} - m\boldsymbol{\omega} \times (\boldsymbol{\omega} \times \boldsymbol{r}) + 2m\boldsymbol{v} \times \boldsymbol{\omega}. \tag{8.1}$$

Here $\boldsymbol{F}_{\mathrm{e}}$, m and $\boldsymbol{\omega}$ stand for the net force, the mass of the object and the angular velocity vector of the rotating frame, respectively. The position vector $\boldsymbol{r}$ is the one measured in the rotating frame and $\boldsymbol{v}$ and $\boldsymbol{a}$ are its first and second derivatives, respectively (so they correspond to the velocity and acceleration as measured in the rotating frame).

This lecture is concerned about analysing the virtual force components appearing in Eq. (8.1) and to discuss phenomena related to them.

Centrifugal force The first virtual force component in Eq. (8.1) is called centrifugal force. Firstly, I show using a vector identity, that

$$\boldsymbol{F}_{\mathrm{cf}} = -m\boldsymbol{\omega} \times (\boldsymbol{\omega} \times \boldsymbol{r}) = m\omega^2 \boldsymbol{\rho}, \tag{8.2}$$

where $\boldsymbol{\rho}$ is a vector perpendicular to the axis of rotation and points from the axis to the object considered.

To demonstrate the effect of this force we perform a few experiments:

1. A track is being rotated with a constant angular velocity with a small trolley on it. a) We first let the trolley roll freely and observe that it does not remain in equilibrium, rather accelerates in radial direction away from the axis of rotation. b) When a spring scale is

attached to the trolley one observes that it remains in equilibrium, although non-zero net force is measured with the scale. We also check the effect of the angular velocity in both cases.

2. Coloured water is poured in a glass that is then rotated around its symmetry axis. The shape of the water surface changes with the angular velocity and takes a paraboloid-like shape.

3. A model of Earth consisting of thin bent plates that form a sphere is investigated. With increasing angular velocity the shape of the sphere changes and gets elongated in the radial direction and contracts along the axis of rotation. This experiment is to demonstrate why the Earth has a geoid shape.

4. A chain is rotated using an electric motor up to a rather high angular velocity. Then the chain is detached from the motor and let to move freely. One observes that due to the large centrifugal forces the chain behaves like a rigid wheel and rolls freely to a quite long distance.

5. A piece of paper having a circular shape is rotated quickly around its symmetry axis. Due to the centrifugal forces it becomes so rigid, that it can be used as a saw to cut a small peace of wood.

After discussing the experiments and the role of the centrifugal force a short calculation is presented to approximate the difference in the gravitational acceleration that one measures at the poles of the Earth and at the Equator.

Coriolis force First we ask the question whether the Earth is rotating or the world around us. One could decide based on the centrifugal force, but its effect is rather small, and one needs to perform measurements at distant locations. Then we show an experiment that demonstrates that when a frame around a pendulum is rotated, the pendulum keeps oscillating in the same plane. Based on this observation we introduce the famous experiment of Foucault. Due to the large space needed by the Foucault pendulum, the experiment is set up at one of the staircases of the university and the students follow the experiment live on a screen from the lecture hall.

To explain the observed behaviour the second virtual force component in Eq. (8.1) is considered:

$$\boldsymbol{F}_{\mathrm{Co}} = 2m\boldsymbol{v} \times \boldsymbol{\omega} = 2m(\boldsymbol{v} \times \boldsymbol{\omega}_{\mathrm{f}} + \boldsymbol{v} \times \boldsymbol{\omega}_{\acute{\mathrm{e}}}), \tag{8.3}$$

where the angular velocity was split up to two components as $\boldsymbol{\omega} = \boldsymbol{\omega}_{\mathrm{f}} + \boldsymbol{\omega}_{\acute{\mathrm{e}}}$, that is, to a component pointing in direction north and one pointing upwards (or downwards on the Southern Hemisphere).

The effect of the Coriolis force on moving objects near the Earth We analyse the terms of Eq. (8.3) in more detail to understand its effect on objects moving in different directions. For instance, the Eötvös effect is deduced, that is, the weight of object moving East gets smaller whereas those moving West gets larger.

Foucault pendulum and the Eötvös balance To understand the behaviour of the Foucault pendulum an experiment with the model of a Foucault pendulum is performed. This consists of a pendulum swinging on a rotated frame and the bob contains ink that gradually flows out on a paper, so, the path of the pendulum is visualized. A star like pattern is obtained and discussed in terms of the Coriolis force.

Afterwards the operation of Eötvös balance is shown and it is explained how this device can be used to demonstrate the rotation of the Earth within seconds.

Phenomena on the rotating Earth The lecture is concluded by mentioning few phenomena related to the rotation of Earth, such as the rotation of cyclones, and, finally, a gyroscope that can be used as a compass (gyrocompass) is shown and explained.

Lecture 20: Gravitation II.

During the preceding lecture the students got familiar with Laws of Kepler, central force fields and the conservation of angular momentum.

This lecture continues the discussion of gravitation and comprises one of the most influential experiments of physics, the Cavandish experiment, that is demonstrated to the students in the lecture hall. I believe that seeing this sophisticated experiment is very impressive for first year physics students, and this is the reason why I selected this lecture as one candidate for my habilitation lecture.

Areal velocity We start by deriving Kepler's second law from the conservation of angular momentum in a central force field. After showing that the areal velocity (the area swept over unit time by the vector connecting the origin and the moving object) is half of the magnitude of the angular momentum, we conclude that the gravitational force is central and that objects in a gravitational field perform planar motion.

Newton's law of universal gravitation Assuming that an object moves on a circular path around the Sun we derive the Newton's law of universal gravitation using Kepler's Laws. We conclude that

$$\boldsymbol{F}_g = -G\frac{m_1 m_2}{r^2}\frac{\boldsymbol{r}}{r}, \tag{8.4}$$

where m_1 and m_2 denote the masses of the interacting objects, $\boldsymbol{r}$ is a vector between the two objects pointing to the one $\boldsymbol{F}_g$ acts on and G is the gravitational constant. We discuss that

Newton was unable to measure the value of the latter, because from astronomical observations only the product $G \cdot M$ could be calculated, where M is the mass of the Sun.

The Cavendish experiment The measurement of the value of G had become possible much later with the Cavandish experiment, performed in 1798. It was also important because it demonstrated, for the first time, that gravitation can be not only observed on astronomical scales but also between regular objects in a laboratory.

During the lecture the experiment is performed with a torsion balance similar to the original. The rotation of the balance is monitored in two ways: a) A laser beam is pointed directly at the mirror attached to the arm of the balance and the motion of the light spot can be observed visually by the students on the wall of the lecture hall. b) An electronic device measures the position using red LEDs and a computer automatically collects the data.

The first measurement has the advantage that the value of G can be determined by the students themselves using a simple calculation that assumes constant acceleration of the masses. The second method, on the other hand, shows the complete history of the rotation where, for instance, damping due to air drag can be observed.

Work of the gravitational field In the last part of the lecture the work done by the gravitational field is calculated and we conclude that it is independent of the path itself, that is, the gravitational field is conservative. This finding will be exploited during the subsequent lecture that is concerned about planetary motion.

Lecture 25: Mechanics of rigid bodies IV.

This lecture concludes the semester and is the last in a row to discuss the mechanics of rigid bodies. The preceding lectures were concerned about kinematics and dynamics of rigid bodies rotating around a fixed axis. Quantities such as torque, moment of inertia, rotational energy and angular momentum were introduced as well as the fundamental dynamical equation of rotational motion.

Work and work theorem for rotating motion We start by determining the work done by a force acting on a rigid body that is allowed to rotate around a fixed axis. From the definition of work we conclude that the work is

$$W_{\mathrm{f}} = \int_{\vartheta_1}^{\vartheta_2} M \mathrm{d}\vartheta, \tag{8.5}$$

where ϑ is the angle of rotation and M is the component of the torque parallel with the axis.

With the definition of work the work theorem is stated for rotational motion. In order to bring these quantities closer to the students, a simple problem is solved using the work theorem followed by summarizing analogies between the quantities and equations describing dynamics of a point like object and that of a rigid body rotating around a fixed axis (e.g., the force is analogous to the torque).

Physical pendulum The motion of a physical pendulum is then discussed. Using the fundamental dynamic equation for rotational motion we conclude that

$$\Theta\ddot{\vartheta} = -Gs\sin\vartheta, \tag{8.6}$$

where Θ is the moment of inertia, ϑ is the angle between vertical and the line connecting the axis of rotation and the centre of mass, G is the weight of the pendulum and s is the distance of the axis and the centre of mass. Using an analogy with the equation of motion of a harmonic oscillator we conclude that for small angles the pendulum performs harmonic oscillations with angular velocity $\omega_0 = \sqrt{\frac{Gs}{\Theta}}$. To demonstrate this result we perform an experiment with a rigid body where s can be tuned and show how the period depends on s. We also perform a short calculation to obtain the angular frequency of a uniform rod swinging around one of its ends.

General motion of a rigid body The dynamics of a rigid body is dictated by two vector equations:

$$\boldsymbol{F}_\mathrm{e} = m\boldsymbol{a}_\mathrm{TKP}, \tag{8.7}$$

that is, the net force $\boldsymbol{F}_\mathrm{e}$ determines the acceleration of the center of mass $\boldsymbol{a}_\mathrm{TKP}$ and

$$\boldsymbol{M}_\mathrm{e} = \dot{\boldsymbol{L}}, \tag{8.8}$$

that is, the net torque on the center of mass ($\boldsymbol{M}_\mathrm{e}$) is equal to the time derivative of the angular momentum $\boldsymbol{L}$. To express the latter with the orientation of the body requires the introduction of the moment of inertia tensor which is out of the scope of this course. It is part of the parallel advanced mechanics course.

Planar motion of a rigid body Here we continue with the special case of planar motion, when each point of the body move in parallel planes. In this case only the z component of the second equation above is considered where the z axis is chosen to be perpendicular to the plane. In addition, the moment of inertia is scalar and $L_z = \Theta\omega$.

To demonstrate how the resulting equations are solved in practice we consider the rolling motion of a cylinder and a wheel. Before solving the dynamical equation an experiment is performed where a cylinder and a wheel having equal mass and radius are let to roll down

a slope. The calculation then proves the observations that the cylinder rolls faster due to its smaller moment of inertia.

Gyroscope and torque-free and torque-induced precession At the very end of the semester phenomena related to gyroscopes are briefly discussed. Since the analytical treatment is again out of the scope of this course we rather present many experiments with various gyroscopes, explain the difference between the two types of precession and derive a formula for the torque-induced precession: $\omega_P = \frac{M}{\Theta\omega}$, where M is the external torque, Θ is the moment of inertia and ω is the angular velocity of the gyroscope. The validity of this formula is verified experimentally. The semester is concluded with presenting a few exotic gyroscopes without an intention to explain the observed complex behaviour.

Acknowledgements

Throughout the writing of this thesis, which eventually took significantly longer than I planned, I have received a great deal of help that I would like to thank hereby.

First of all, I would like express my gratitude to all my colleagues and students, who I had the chance to work with during my research presented in this thesis. For me, most of the motivation and inspiration for scientific work comes from interactions, such as lively discussions at conferences, smart or funny comments from my students, the joy when we together start to understand something, skype meetings with colleagues being far away, group meetings with progress reports and pizzas, and so on. I believe that if I had had to work alone, not much from the results presented above would actually exist.

I am also very grateful to those many people who were persistently pushing me to write this thesis. Since I myself have always considered this task somewhat inferior to other activities, I think they played a crucial role in this document's coming into existence. Special thanks to those who helped me with the latex template.

Finally, I sincerely thank István Groma for the invaluable help and support I received from him throughout my career. In addition, as a head of the Department of Materials Physics he created a friendly and peaceful atmosphere, that I find indispensable for scientific work, and also had a pivotal contribution in the establishment and maintenance of the experimental facilities that the experimental part of this thesis is based on.

Bibliography

[1] E. Orován, Z. Phys. **84**, 634 (1934).

[2] G. I. Taylor, Proc. R. Soc. London, Ser. A **145**, 362 (1934).

[3] M. Polányi, Z. Phys. **84**, 660 (1934).

[4] G. I. Taylor, J. Inst. Metals **62**, 307 (1938).

[5] R. Hill and J. R. Rice, J. Mech. Phys. Solids **20**, 401 (1972).

[6] R. J. Asaro and A. Needleman, Acta Metall. **33**, 923 (1985).

[7] L. P. Kubin and Y. Estrin, Acta Metall. **33**, 397 (1985).

[8] E. C. Aifantis, Int. J. Plast. **3**, 211 (1987).

[9] W. A. Curtin and R. E. Miller, Modell. Simul. Mater. Sci. Eng. **11**, R33 (2003).

[10] A. Arsenlis, D. M. Parks, R. Becker and V. V. Bulatov, J. Mech. Phys. Solids **52**, 1213 (2004).

[11] V. Vitek, M. Mrovec and J. L. Bassani, Mat. Sci. Eng. A **365**, 31 (2004).

[12] N. Zaafarani, D. Raabe, R. N. Singh, F. Roters and S. Zaefferer, Acta Mater. **54**, 1863 (2006).

[13] S. Keshavarz and S. Ghosh, Acta Mater. **61**, 6549 (2013).

[14] N. A. Fleck, G. M. Müller, M. F. Ashby and J. W. Hutchinson, Acta Mater. **42**, 475 (1994).

[15] K. W. McElhaney, J. J. Vlassak and W. D. Nix, J. Mat. Res. **13**, 1300 (1998).

[16] J. Weiss, F. Lahaie and J.-R. Grasso, J. Geophys. Res. **105**, 433 (2000).

[17] M.-C. Miguel, A. Vespignani, S. Zapperi, J. Weiss and J.-R. Grasso, Nature **410**, 667 (2001).

[18] J. Weiss and D. Marsan, Science **299**, 89 (2003).

[19] M. D. Uchic, D. M. Dimiduk, J. N. Florando and W. D. Nix, Science **305**, 986 (2004).

[20] D. M. Dimiduk, M. D. Uchic and T. A. Parthasarathy, Acta Mater. **53**, 4065 (2005).

[21] D. M. Dimiduk, C. Woodward, R. LeSar and M. D. Uchic, Science **312**, 1188 (2006).

[22] F. F. Csikor, C. Motz, D. Weygand, M. Zaiser and S. Zapperi, Science **318**, 251 (2007).

[23] D. S. Fisher, K. Dahmen, S. Ramanathan and Y. Ben-Zion, Phys. Rev. Lett. **78**, 4885 (1997).

[24] S. Zapperi, P. Cizeau, G. Durin and H. E. Stanley, Phys. Rev. B **58**, 6353 (1998).

[25] N. Martys, M. Cieplak and M. O. Robbins, Phys. Rev. Lett. **66**, 1058 (1991).

[26] P. Daguier, B. Nghiem, E. Bouchaud and F. Creuzet, Phys. Rev. Lett. **78**, 1062 (1997).

[27] M. D. Uchic, P. A. Shade and D. M. Dimiduk, Ann. Rev. Mater. Res. **39**, 361 (2009).

[28] C. R. Weinberger and W. Cai, P. Natl. Acad. Sci. **105**, 14304 (2008).

[29] A. Cao and E. Ma, Acta Mater. **56**, 4816 (2008).

[30] S. Xu, Y. Guo and A. Ngan, Int. J. Plast. **43**, 116 (2013).

[31] L. A. Zepeda-Ruiz, A. Stukowski, T. Oppelstrup and V. V. Bulatov, Nature **550**, 492 (2017).

[32] V. Bulatov and W. Cai, *Computer Simulations of Dislocations*, Oxford Series on Materials Modelling (Oxford University Press, Oxford, New York, 2013).

[33] J. P. Hirth and J. Lothe, *Theory of Dislocations*, 2nd ed. (John Willey & Sons, New York, 1982).

[34] B. Bakó, I. Groma, G. Györgyi and G. Zimányi, Comp. Mater. Sci. **38**, 22 (2006).

[35] E. van der Giessen and A. Needleman, Model. Simul. Mater. Sc. **3**, 689 (1995).

[36] A. A. Benzerga, Y. Bréchet, A. Needleman and E. van der Giessen, Model. Simul. Mater. Sc. **12**, 159 (2004).

[37] S. S. Chakravarthy and W. Curtin, J. Mech. Phys. Solids **58**, 625 (2010).

[38] J. Rosti, J. Koivisto, L. Laurson and M. J. Alava, Phys. Rev. Lett. **105**, 100601 (2010).

[39] M.-C. Miguel, A. Vespignani, M. Zaiser and S. Zapperi, Phys. Rev. Lett. **89**, 165501 (2002).

[40] M. Zaiser, B. Marmo and P. Moretti, in *Proceedings of the International Conference on Statistical Mechanics of Plasticity and Related Instabilities* (2005) poS (SMPRI2005) 053.

[41] M. Zaiser, Adv. Phys. **55**, 185 (2006).

[42] B. Bakó, I. Groma, G. Györgyi and G. T. Zimányi, Phys. Rev. Lett. **98**, 075701 (2007).

[43] P. D. Ispánovity, I. Groma, W. Hoffelner and M. Samaras, Model. Simul. Mater. Sc. **19**, 045008 (2011).

[44] F. F. Csikor and I. Groma, Phys. Rev. B **70**, 064106 (2004).

[45] P. D. Ispánovity and I. Groma, J. Stat. Mech. , P12009 (2008).

[46] P. M. Derlet and R. Maaß, Model. Simul. Mater. Sc. **21**, 035007 (2013).

[47] M. Zaiser, J. Schwerdtfeger, A. S. Schneider, C. P. Frick, B. G. Clark, P. A. Gruber and E. Arzt, Philos. Mag. **88**, 3861 (2008).

[48] A. Rinaldi, P. Peralta, C. Friesen and K. Sieradzki, Acta Mater. **56**, 511 (2008).

[49] R. Maaß, S. Van Petegem, D. Ma, J. Zimmermann, D. Grolimund, F. Roters, H. Van Swygenhoven and D. Raabe, Acta Mater. **57**, 5996 (2009).

[50] F. F. Csikor, M. Zaiser, P. D. Ispánovity and I. Groma, J. Stat. Mech. **2009**, P03036 (2009).

[51] D. S. Fisher, Physics Rep. **301**, 113 (1998).

[52] S. Zapperi and M. Zaiser, Mat. Sci. Eng. A **309**, 348 (2001).

[53] B. Bakó, D. Weygand, M. Samaras, W. Hoffelner and M. Zaiser, Phys. Rev. B **78**, 144104 (2008).

[54] M. Zaiser and P. Moretti, J. Stat. Mech. **2005**, P08004 (2005).

[55] K. A. Dahmen, Y. Ben-Zion and J. T. Uhl, Phys. Rev. Lett. **102**, 175501 (2009).

[56] N. Friedman, A. T. Jennings, G. Tsekenis, J.-Y. Kim, M. Tao, J. T. Uhl, J. R. Greer and K. A. Dahmen, Phys. Rev. Lett. **109**, 095507 (2012).

[57] G. Tsekenis, J. T. Uhl, N. Goldenfeld and K. A. Dahmen, EPL (Europhysics Letters) **101**, 36003 (2013).

[58] X. Zhang, B. Pan and F. Shang, EPL (Europhysics Letters) **100**, 16005 (2012).

[59] M. Ovaska, L. Laurson and M. J. Alava, Sci. Rep. **5**, 1 (2015).

[60] P. Zhang, O. U. Salman, J.-Y. Zhang, G. Liu, J. Weiss, L. Truskinovsky and J. Sun, Acta Mater. **128**, 351 (2017).

[61] H. Salmenjoki, A. Lehtinen, L. Laurson and M. J. Alava, Phys. Rev. Mater. **4**, 083602 (2020).

[62] P. M. Derlet and R. Maass, Philos. Mag. **95**, 1829 (2015).

[63] S. Papanikolaou, D. M. Dimiduk, W. Choi, J. P. Sethna, M. D. Uchic, C. F. Woodward and S. Zapperi, Nature **490**, 517 (2012).

[64] J.-C. Baret, D. Vandembroucq and S. Roux, Phys. Rev. Lett. **89**, 195506 (2002).

[65] M. Talamali, V. Petäjä, D. Vandembroucq and S. Roux, Phys. Rev. E **84**, 016115 (2011).

[66] C. Liu, E. E. Ferrero, F. Puosi, J.-L. Barrat and K. Martens, Phys. Rev. Lett. **116**, 065501 (2016).

[67] Z. Budrikis, D. F. Castellanos, S. Sandfeld, M. Zaiser and S. Zapperi, Nat. Commun. **8**, 1 (2017).

[68] J. D. Eshelby, P. Roy. Soc. Lond. A **241**, 376 (1957).

[69] M. Ashby and A. L. Greer, Scripta Mater. **54**, 321 (2006).

[70] C. A. Schuh, T. C. Hufnagel and U. Ramamurty, Acta Mater. **55**, 4067 (2007).

[71] S. Papanikolaou, H. Song and E. van der Giessen, J. Mech. Phys. Solids **102**, 17 (2017).

[72] R. B. Sills and W. Cai, Model. Simul. Mater. Sc. **22**, 025003 (2014).

[73] B. Devincre, R. Madec, G. Monnet, S. Queyreau, R. Gatti and L. Kubin, in *Mechanics of Nano-Objects*, edited by O. Thomas, A. Ponchet and S. Forest (Presses des Mines, Paris, 2011) pp. 81–100.

[74] D. J. Gardner, C. S. Woodward, D. R. Reynolds, G. Hommes, S. Aubry and A. Arsenlis, Model. Simul. Mater. Sc. **23**, 025006 (2015).

[75] C. R. Weinberger and W. Cai, J. Mech. Phys. Solids **55**, 2027 (2007).

[76] N. Fleck and J. Hutchinson, in *Advances in Applied Mechanics*, Vol. 33, edited by J. W. Hutchinson and T. Y. Wu (Elsevier, 1997) pp. 295–361.

[77] H. T. Zhu, H. Zbib and E. Aifantis, Acta Mech. **121**, 165 (1997).

[78] E. Aifantis, J. Eng. Mater. Technol. **2**, 189 (1999).

[79] N. Fleck and J. Hutchinson, J. Mech. Phys. Solids **49**, 2245 (2001).

[80] M. Gurtin, J. Mech. Phys. Solids **50**, 313 (2002).

[81] D. Holt, J. Appl. Phys **41**, 3197 (1970).

[82] N. Hansen and D. Kuhlmann-Wilsdorf, Mater. Sci. Eng. **81**, 141 (1986).

[83] D. Walgraef and E. Aifantis, J. Appl. Phys. **58**, 688 (1985).

[84] J. Pontes, D. Walgraef and E. Aifantis, Int. J. Plast. **22**, 1486 (2006).

[85] L. Kubin and G. Canova, Scripta Metall. **27**, 957 (1992).

[86] N. Ghoniem and L. Sun, Phys. Rev. B **60**, 128 (1999).

[87] B. Devincre, L. Kubin, C. Lemarchand and R. Madec, Mat. Sci. Eng. A **309**, 211 (2001).

[88] R. Madec, B. Devincre and L. Kubin, Scripta Mater. **47**, 689 (2002).

[89] A. Hussein, S. Rao, M. Uchic, D. Dimiduk and J. El-Awady, Acta Mater. **85**, 180 (2015).

[90] S. Xia and A. El-Azab, Modell. Simul. Mater. Sci. Eng. **23**, 055009 (2015).

[91] P. Lin and A. El-Azab, Modell. Simul. Mater. Sci. Eng. **28**, 045003 (2020).

[92] I. Groma, Phys. Rev. B **56**, 5807 (1997).

[93] M. Zaiser, M.-C. Miguel and I. Groma, Phys. Rev. B **64**, 224102 (2001).

[94] I. Groma, F. Csikor and M. Zaiser, Acta Mater. **51**, 1271 (2003).

[95] I. Groma, G. Györgyi and B. Kocsis, Phil. Mag. **87**, 1185 (2007).

[96] S. Mesarovic, R. Baskaran and A. Panchenko, J. Mech. Phys. Solids **58**, 311 (2010).

[97] M. Dogge, R. Peerlings and M. Geers, Mech. Mater. **88**, 30 (2015).

[98] S. Yefimov, I. Groma and E. van der Giessen, J. Mech. Phys. Solids **52**, 279 (2004).

[99] I. Groma, G. Györgyi and B. Kocsis, Phys. Rev. Letters **96**, 165503 (2006).

[100] T. Hochrainer and M. Zaiser, in *International Conference on Statistical Mechanics of Plasticity and Related Instabilities*, Vol. 23 (SISSA Medialab, 2006) p. 002.

[101] T. Hochrainer, M. Zaiser and P. Gumbsch, Phil. Mag. **87**, 1261 (2007).

[102] S. Sandfeld, T. Hochrainer, P. Gumbsch and M. Zaiser, Phil. Mag. **90**, 3697 (2010).

[103] T. Hochrainer, S. Sandfeld, M. Zaiser and P. Gumbsch, J. Mech. Phys. Solids **63**, 167 (2014).

[104] T. Hochrainer, Phil. Mag. **95**, 1321 (2015).

[105] T. Hochrainer, J. Mech. Phys. Solids **88**, 12 (2016).

[106] Y. Kawasaki and T. Takeuchi, Scripta Metall. **14**, 183 (1980).

[107] G. Zhang, R. Schwaiger, C. Volkert and O. Kraft, Philos. Mag. Lett. **83**, 477 (2003).

[108] K. Siu and A. Ngan, Philos. Mag. **93**, 449 (2013).

[109] H. Mughrabi, Acta metallurgica **31**, 1367 (1983).

[110] M. Sauzay and L. P. Kubin, Prog. Mater. Sci. **56**, 725 (2011).

[111] A. El-Azab, Scripta Mater. **54**, 723 (2006).

[112] K. Schulz and M. Sudmanns, PAMM **17**, 107 (2017).

[113] M. Sudmanns, M. Stricker, D. Weygand, T. Hochrainer and K. Schulz, J. Mech. Phys. Solids **132**, 103695 (2019).

[114] K. Zoller and K. Schulz, Acta Mater. **191**, 198 (2020).

[115] A. J. Wilkinson, G. Meaden and D. J. Dingley, Ultramicroscopy **106**, 307 (2006).

[116] A. J. Wilkinson and D. Randman, Philos. Mag. **90**, 1159 (2010).

[117] D. Chen, J.-C. Kuo and W.-T. Wu, Ultramicroscopy **111**, 1488 (2011).

[118] S. Kalácska, *Experimental investigation of plastic deformation induced dislocation systems*, Ph.D. thesis, Eötvös Loránd University, Doctoral School of Physics (2017), https://doi.org/10.15476/ELTE.2017.145.

[119] A. J. Wilkinson, E. Tarleton, A. Vilalta-Clemente, J. Jiang, T. B. Britton and D. M. Collins, Appl. Phys. Lett. **105**, 181907 (2014).

[120] I. Groma, Phys. Rev. B **57**, 7535 (1998).

[121] I. Groma and B. Bakó, Phys. Rev. B **58**, 2969 (1998).

[122] D. Hart and H. Bruck, Exp. Mech. **60**, 345 (2020).

[123] S. Ohr, Mater. Sci. Eng. **72**, 1 (1985).

[124] J. Ast, M. N. Polyakov, G. Mohanty, J. Michler and X. Maeder, Mat. Sci. Eng. A **710**, 400 (2018).

[125] E. Tarleton and S. G. Roberts, Philos. Mag. **89**, 2759 (2009).

[126] J. Weiss, W. B. Rhouma, T. Richeton, S. Dechanel, F. Louchet and L. Truskinovsky, Phys. Rev. Lett. **114**, 105504 (2015).

[127] J. Gubicza, P. T. Hung, M. Kawasaki, J.-K. Han, Y. Zhao, Y. Xue and J. L. Lábár, Mater. Charact. **154**, 304 (2019).

[128] G. Ananthakrishna, S. Noronha, C. Fressengeas and L. Kubin, Phys. Rev. E **60**, 5455 (1999).

[129] A. Lehtinen, G. Costantini, M. J. Alava, S. Zapperi and L. Laurson, Phys. Rev. B **94**, 064101 (2016).

[130] J. Heo, S. Kim, S. Ryu and D. Jang, Sci. Rep. **6**, 1 (2016).

[131] T. Richeton, P. Dobron, F. Chmelik, J. Weiss and F. Louchet, Mat. Sci. Eng. A **424**, 190 (2006).

[132] J. Weiss, T. Richeton, F. Louchet, F. Chmelik, P. Dobron, D. Entemeyer, M. Lebyodkin, T. Lebedkina, C. Fressengeas and R. J. McDonald, Phys. Rev. B **76**, 224110 (2007).

[133] J. Alcalá, J. Očenášek, J. Varillas, J. A. El-Awady, J. M. Wheeler and J. Michler, Sci. Rep. **10**, 1 (2020).

[134] B. Devincre, T. Hoc and L. Kubin, Science **320**, 1745 (2008).

[135] H. Salmenjoki, M. J. Alava and L. Laurson, Nat. Commun. **9**, 1 (2018).

[136] K. Schulz, S. Kreis, H. Trittenbach and K. Boehm, Engineering Fracture Mechanics **218**, 106552 (2019).

[137] Z. Yang, S. Papanikolaou, A. C. Reid, W.-k. Liao, A. N. Choudhary, C. Campbell and A. Agrawal, Sci. Rep. **10**, 1 (2020).

[138] S. Biswas, D. F. Castellanos and M. Zaiser, Sci. Rep. **10**, 1 (2020).

[139] M. H. Rafiei, Y. Gu and J. A. El-Awady, JOM **72**, 4380 (2020).

[140] M. Sarvilahti, A. Skaugen and L. Laurson, APL Mater. **8**, 101109 (2020).

[141] L. Lu, M. Dao, P. Kumar, U. Ramamurty, G. E. Karniadakis and S. Suresh, P. Natl. Acad. Sci. **117**, 7052 (2020).

[142] J. Shimanek, Q. Rizzardi, G. Sparks, P. M. Derlet and R. Maaß, J. Mater. Res. **35**, 196 (2020).

[143] H. Trittenbach, M. Gauch, K. Böhm and K. Schulz, in *2018 IEEE 5th International Conference on Data Science and Advanced Analytics (DSAA)* (IEEE, 2018) pp. 450–459.

[144] S. Patinet, D. Vandembroucq and M. L. Falk, Phys. Rev. Lett. **117**, 045501 (2016).

[145] A. Nicolas, E. E. Ferrero, K. Martens and J.-L. Barrat, Rev. Mod. Phys. **90**, 045006 (2018).

[146] T. W. Barraclough, J. R. Blackford, S. Liebenstein, S. Sandfeld, T. J. Stratford, G. Weinländer and M. Zaiser, Nat. Phys. **13**, 272 (2017).